



**UNIVERSITY OF TRENTO**

Department of Physics

Doctoral Programme in Physics

XXXIII Enrolment Cycle

**Nuclear fragmentation in particle  
therapy and space radiation protection:  
from the standard approach to the  
FOOT experiment**

Supervisors

Prof. Chiara LA TESSA

Dr. Francesco TOMMASINO

Candidate

Sofia COLOMBI



### **Commission of the final examination**

External Referees: Prof. Vincenzo Monaco, Dr. Michael Sivertz

External Members: Prof. Vincenzo Monaco, Dr. Uli Weber

Internal Member: Prof. Pietro Faccioli

### **Final examination**

Date: 23/02/2021



# Abstract

A lack of experimental cross section data for light fragments ( $A < 20$ ) and neutrons for primary beams energy spanning between few MeV to GeV emerges from available literature and has been recently pointed out also by the International Commission on Radiological Protection (ICRP) [1]. Thus, dedicated studies are highly recommended to improve experimental cross-sectional data tables in order to further develop the computational methods at the base of Monte Carlo transport codes currently used in particle therapy and space radiation protection. In fact, secondary particles generated in the nuclear interactions occurring between charged radiation and matter require a detailed investigation.

Nuclear interactions occurring between the primary beam and the patient's body change the primary radiation field reaching the tumoral site and the other body tissues. At present, a detailed knowledge of the fragments production in biological materials significantly different from water is required to improve the quality of delivered treatment planning. The high energy charged particles composing the space radiation environment can seriously harm astronauts' health. Thus, efficient passive shielding countermeasures are needed. However, a more complete characterization of lighter and highly penetrating radiation generated in the interaction of the radiation field with e.g. materials composing the spaceship hull or in-situ compounds for planetary base missions is required to assess and mitigate the radiation-induced health risk.

In this work several analysis related to secondary fragments characterization of data collected by means of a relatively simple experimental setup widely used up to now to perform nuclear fragmentation studies are provided. A novel experiment of applied nuclear physics named FOOT (FragmentiOn Of Target) has been conceived in the last years to improve the characterization of both projectile and target fragments, and to measure nuclear fragmentation cross sections with great accuracy for beams and targets of interest in particle therapy and space radioprotection. In this work an extended investigation of the FOOT experimental setup performances and fragments reconstruction capabilities is discussed.

# Table of Contents

List of Acronyms	VIII
Introduction	1
<b>1 Radiation interaction with matter</b>	<b>5</b>
1.1 Interaction of charged particles with matter . . . . .	5
1.1.1 Energy deposition in matter: the Bethe-Block formula . . . . .	5
1.1.2 Mean range and energy straggling . . . . .	8
1.1.3 Angular straggling . . . . .	10
1.1.4 Nuclear fragmentation . . . . .	11
1.2 Interaction of neutral particles with matter . . . . .	13
1.2.1 Neutrons . . . . .	13
1.2.2 Photons . . . . .	14
1.3 Application of nuclear interaction in research . . . . .	15
1.3.1 Particle therapy . . . . .	16
1.3.2 Space radiation protection . . . . .	19
1.4 Experimental cross sections . . . . .	20
1.4.1 Particle therapy . . . . .	21
1.4.2 Space radiation . . . . .	30
<b>2 Experimental approaches to fragments detection</b>	<b>37</b>
2.1 Standard setup . . . . .	38
2.2 The FOOT experiment . . . . .	42
2.2.1 Experimental strategies . . . . .	43
2.2.2 The design criteria of the FOOT apparatus . . . . .	45
2.2.3 Electronic detector setup . . . . .	47
Pre-target region . . . . .	47
Magnetic spectrometer . . . . .	49
Downstream region . . . . .	52
DAQ and trigger . . . . .	54

2.2.4	Emulsion spectrometer . . . . .	54
<b>3</b>	<b>Standard experimental approach to fragments characterization</b>	<b>59</b>
3.1	Particle identification with a $\Delta E - E$ telescope . . . . .	59
3.2	Time of Flight technique . . . . .	65
3.3	Two relevant studies for particle therapy and space radioprotection	67
3.3.1	Interaction of 400 MeV/u $^{12}\text{C}$ ions with bone-like materials .	68
3.3.2	Secondary neutrons produced by fragmentation of $^{58}\text{Ni}$ ions in materials relevant for space radioprotection . . . . .	70
<b>4</b>	<b>Global analysis of the FOOT experiment</b>	<b>81</b>
4.1	The analysis software . . . . .	81
4.2	Monte Carlo simulations . . . . .	82
4.3	Fragments identification . . . . .	84
4.3.1	Charge identification . . . . .	88
4.3.2	Mass identification . . . . .	89
4.4	Cross sections measurements . . . . .	98
4.5	Analysis of performances . . . . .	105
<b>5</b>	<b>FOOT real data analysis</b>	<b>111</b>
5.1	Data samples . . . . .	111
5.2	Energy calibration . . . . .	114
5.3	Charge reconstruction . . . . .	117
<b>6</b>	<b>Future work: neutrons detection with FOOT</b>	<b>123</b>
	<b>Conclusions</b>	<b>129</b>
	<b>Appendix</b>	<b>132</b>
	Analysis of performances . . . . .	132
	<b>Bibliography</b>	<b>136</b>

# List of Acronyms

**ALM** Augmented Lagrangian Method

**BGO** bismuth germanate

**BMN** Beam Monitor

**BP** Bragg Peak

**CAL** Calorimeter

**CNAO** Centro Nazionale di Adroterapia Oncologica

**DAQ** Data Acquisition

**DNA** deoxyribonucleic acid

**DSB** Double Strand Breaks

**FIRST** Fragmentation of Ions Relevant for Space and Therapy

**FLUKA** FLUktuierende KAskade

**FOOT** FragmentatiOn Of Target

**GCR** Galactic Cosmic Rays

**GSI** Gesellschaft für Schwerionenforschung

**GPU** Graphics Processing Unit

**HIMAC** Heavy-Ion Medical Accelerator

**ID** Identification

**ISS** International Space Station

**ITR** Inner Tracker

**LBL** Lawrence Berkeley Laboratory

**LET** Linear Energy Transfer

**LINAC** LINear Acceleartor

**LNS** Laboratori Nazionali del Sud

**M28** MIMOSA28

**MC** Monte Carlo

**NIRS** National Institute of Radiological Science

**PM** Permanent Magnet

**PMMA** polymethyl methacrylate

**PSI** Paul Scherrer Institute

**RBE** Relative Biological Effectiveness

**SCN** Scintillator detector

**SHOE** Software for Hadrontherapy Optimization Experiment

**SiPM** Silicon Photomultiplier

**SOBP** Spread Out Bragg Peak

**SPE** Solar Particles Events

**SSB** Single Strand Breaks

**STC** Start Counter

**TPS** Treatment Planning System

**VTX** Vertex detector

# Introduction

Nowadays, the application of particle beams in cancer therapy is a well-established strategy and its combination with surgery, chemotherapy and conventional radiotherapy is becoming an increasingly adopted approach for several clinical cases (e.g. skull base tumors). Currently, protons and  $^{12}\text{C}$  ions are used for patients' treatment, due to their characteristic depth-dose deposition profile featuring a pronounced peak (i.e. the *Bragg Peak*) at the end of range. Clinical energies typically span between 60 and 250 MeV for protons and up to 400 MeV/u for  $^{12}\text{C}$  ions, in order to deliver the required dose to targets at different depths. Interactions between the primary beam and the patient's body can occur during treatment, changing the primary radiation composition, energy and direction and thus affecting its depth- and lateral dose profile. Compared to conventional photon therapy, charged particles might have a different biological effectiveness. This is summarized by the Relative Biological Effectiveness parameter (i.e. RBE, defined as the ratio of photon to charged particles dose necessary to achieve the same biological effect). RBE depends on both biological (e.g. cell type, cell cycle, oxygenation) and physical variables (e.g. dose, particle energy, track structure), and therefore an RBE different from 1 is associated in principle to both protons and carbon ions. However, for a number of reasons, a constant RBE=1.1 is nowadays attributed to protons in clinical practice. Despite of that, it is known that heavy secondary target fragments are generated in proton therapy treatments, which will have a higher biological effectiveness with respect to protons [2]. Moreover, the interaction of carbon ions with the patient's body is currently modeled in the treatment planning on the basis of experimental data measured in water, by rescaling with a density factor for all other biological materials. This approximation neglects the influence of the elemental composition, which might become relevant in cases where the material encountered by the beam significantly differs from water (e.g. bone or lung tissues) and result in a non-uniform and incorrect dose profile.

While the main goal of particle therapy is the inactivation of malignant cancer cells with radiation, space radiation protection aims at the opposite, assessing the radiation induced health risks in space missions in order to reduce the exposure to high radiation doses and preserve the astronauts' life. In fact, the radiation

---

environment in space can lead to serious health risks for astronauts, especially in long duration and far from Earth space missions (like human explorations to Mars). Protons from Solar Particle Events (SPEs) and Van Allen belts and fast heavy ions (i.e., helium and a low amount of heavier particles) coming from Galactic Cosmic Rays (GCR) covering an energy range up to few GeV are among the most abundant particle species in radiation environment in deep space. Today, the only possible countermeasure from space radiation is passive shielding. However, nuclear fragmentation processes can occur inside the spaceship hull, causing the production of lighter and highly penetrating radiation that must be considered when a shielding is designed. Despite the many fundamental open issues in particle therapy and space radiation protection fields, the lack of experimental fragmentation cross section data in their energy range of interest is currently observed. Therefore, accurate experimental measurements providing a detailed knowledge of the transport of charged and neutral particles for beam and targets combinations relevant in particle therapy and space radiation applications would be of great importance in order to further optimize particles treatments and passive shielding. Moreover, additional data would help benchmarking Monte Carlo (MC) codes, which are extensively used by the scientific communities in both research fields. In fact, the available transport codes suffer from many uncertainties and they need to be verified with reliable experimental data. The FOOT (FragmentatiON Of Target) experiment has been specifically designed to measure fragment production high-resolution double differential cross sections for both light (e.g. C, O) and heavy (e.g. Fe) projectiles in the medium energy range (up to 700 MeV/u).

The purpose of this work is the experimental characterization of particles originated in nuclear fragmentation processes for several targets and beams of interest for particle therapy and space radiation protection.

In *Chapter 1*, an overview of the most relevant aspects of charged and neutral particles interactions with matter and their application in particle therapy and space radiation protection is provided. A review of the existing fragmentation cross section data in this research fields is reported as well. In *Chapter 2*, the experimental setup exploited to date for the characterization of fragments and the final design of the FOOT experimental apparatus are both presented, as well as aims, methods and adopted strategies for the projectile and target fragments detection. In *Chapter 3*, the physical characterization of the interaction of therapeutic  $^{12}\text{C}$  ions with bone-like materials is presented. Secondary neutrons production studied during the ROSSINI (RadiatiON Shielding by ISRU and/or INnovative materIals for EVA, Vehicle and Habitat) experimental campaign for a  $^{58}\text{Ni}$  beam in different targets of interest for different mission scenarios is described too. In *Chapter 4*, a MC based study of the performances and fragments reconstruction capabilities of FOOT by means of a dedicated software developed is discussed. In *Chapter 5*, the preliminary analysis of data collected in two different experimental campaigns

---

at CNAO and GSI with a partial FOOT electronic setup is provided. In *Chapter 6* future perspectives of the FOOT experiment for the detection of neutrons is presented as well.



# Chapter 1

## Radiation interaction with matter

An overview of the relevant physical processes involved in the interaction of charged particles and neutrons with matter is given in this chapter. For both types of interaction an energy transfer occurs. While charged particles crossing a medium lose energy through interactions due to Coulomb force and nuclear fragmentation, neutrons carry no charge and therefore cannot interact electromagnetically with matter. Thus, they only interact with a nucleus of the absorbing material, resulting in a secondary charged radiation if the neutral particle is not absorbed.

### 1.1 Interaction of charged particles with matter

Two main types of physical interactions can occur when a charged particle beam passes through a target, both resulting in a lateral spread of the beam:

- Electromagnetic interactions, which rule the energy deposition of the primary beam
- Nuclear interactions, which are responsible for the loss of primary ions and production of secondary radiation.

#### 1.1.1 Energy deposition in matter: the Bethe-Block formula

As they pass through matter, charged particles undergo electromagnetic interactions, losing energy through excitation or ionization of the electrons belonging to the target atoms and elastic collisions with the nuclei of target atoms. The result of

such interaction mechanisms is an energy loss per unit length traveled by ions  $\frac{dE}{dx}$ , which is accurately described by the Bethe-Bloch formula [3, 4, 5] as follows:

$$S(E) = -\frac{dE}{dx} = \frac{4\pi e^2 Z_t Z_p^2}{m_e v^2} \left[ \ln \frac{2m_e v^2}{\langle I \rangle} - \ln(1 - \beta^2) - \beta^2 - \frac{C}{Z_t} - \frac{\delta}{2} \right] \quad (1.1)$$

where  $Z_p$  and  $Z_t$  denote the nuclear charge of the projectile and the target, respectively,  $m_e$  and  $e$  are the mass and the charge of the electron, respectively, and  $\langle I \rangle$  is the mean ionization energy of the target atom or molecule. The formula includes relativistic corrections (Fano version, 1963) with a dependence from  $\beta^2$ , and contains two additional terms: the shell correction  $C/Z_t$  and the density effect correction  $\delta/2$ . The former accounts for the effects which arise when the velocity of the incident particle is comparable or smaller than the orbital velocity of the bound electrons and results in a correction of the stopping power up to 6%. The density term corrects for polarization effects in the target, while the mean ionization  $\langle I \rangle$  corrects for the quantum mechanical energy levels available for the transfer of energy to the target electrons. This formula describes the mean rate of energy loss in the region  $0.05 < \beta\gamma < 10^3$  for intermediate- $Z$  materials with an accuracy of a few percent. According to this formula, the energy loss per unit path length increases with the square of the particle charge as shown in Figure 1.1(a).

The stopping power presents a dependence on the particles energy. The trend for a proton as a function of its energy is depicted in figure 1.1(b), where the contribution of both the electronic and the nuclear parts are represented and can be described in terms of the relativistic parameter  $\beta\gamma$ . At  $\beta\gamma \simeq 3$  it reaches a minimum of ionization,  $dE/dx \simeq 2 \text{ MeV g}^{-1} \text{ cm}^2$ , followed at higher energies by a relativistic rise, with a logarithmic dependence on  $\beta\gamma$ . At even higher energies ( $\beta\gamma > 10^3$ ), the radiative effects become relevant and the Bethe-Bloch equation is no longer valid. On the contrary, as the particle energy decreases from  $\sim 10^3$  MeV to  $\sim 10^{-1}$  MeV the stopping power increases, according to the  $\beta^{-2}$  dependence of Eq. 1.1. Hence, a greater amount of energy per unit length is deposited toward the end of the particle path than at the beginning. A further correction to the Bethe-Bloch formula takes into account the dependence of the projectile effective charge on the velocity. At high velocities, the atomic electrons are completely stripped off and the ion effective charge is equal to its atomic charge number  $Z_p$ . At lower velocities, the mean charge state decreases due to the interplay of ionization and recombination process and the  $Z_p$  in Eq. 1.1 has to be replaced by the effective charge  $Z_{eff}$  described by the Barka's empirical formula:

$$Z_{eff} = Z_p \left[ 1 - \exp(-125\beta Z_p^{-2/3}) \right] \quad (1.2)$$

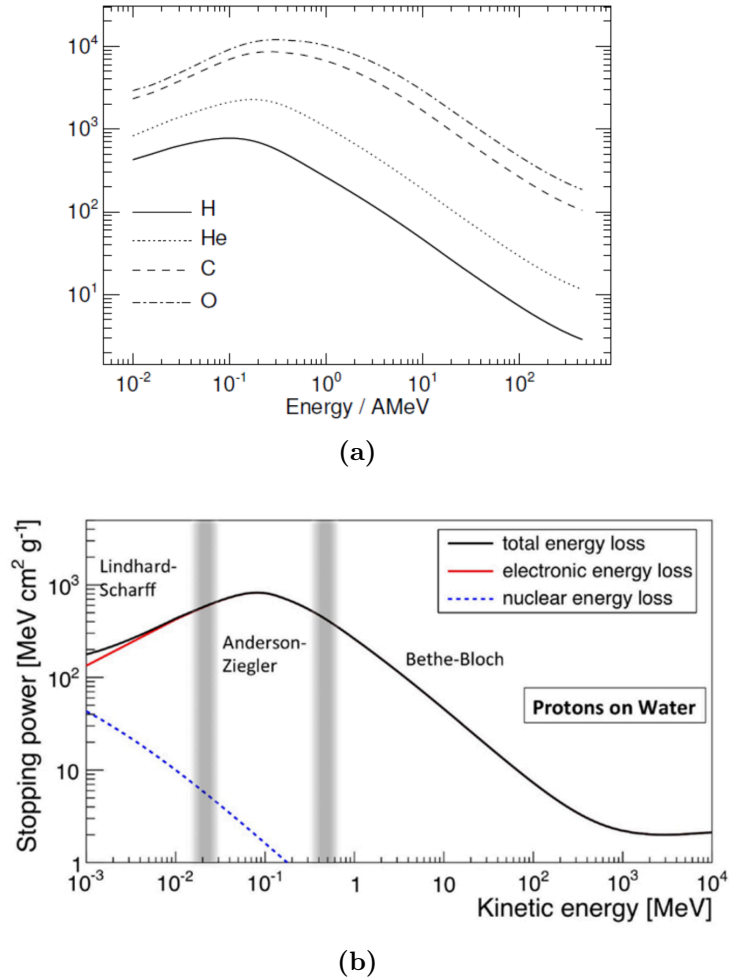


**Figure 1.1:** (a) Electronic stopping power of different ions calculated in water as a function of the energy [6]. (b) Mass stopping power for a proton in water as a function of its energy: the nuclear contribution is relevant only at lower energies [7].

The maximum energy-loss rate is reached at a projectile velocity of

$$v_p \approx Z_p^{-2/3} v_0 \quad (1.3)$$

where  $v_0 = e^2/\hbar$  is the Bohr velocity and the corresponding  $\beta$  value is  $e^2/\hbar c = 1/137$ . For projectile velocities below  $v_p$ , elastic collisions with the target nuclei begin to contribute significantly to the energy loss and dominate the stopping process at the very end of the particle path.

A fundamental quantity strictly related to the energy release of a particle in

matter, and thus to the induced radiation damage, is the *dose* ( $D$ ), which is defined as the ratio between the mean energy  $d\epsilon$  imparted by ionizing radiation in a volume element and the mass  $dm$  of that volume. It can also be expressed as a function of the particle fluence  $F$  [ $cm^{-2}$ ], the specific energy loss of that particle in the target  $dE/dx$  [ $\frac{keV}{\mu m}$ ] and the density of the target  $\rho$  [ $\frac{g}{cm^3}$ ] [8], as follows:

$$D = \frac{d\epsilon}{dm} = 1.6 \cdot 10^{-9} F \frac{dE}{dx} \frac{1}{\rho} \quad (1.4)$$

$D$  is expressed in units of Gray (Gy), where  $1 \text{ Gy} = 1 \text{ J kg}^{-1}$ . In particular, the energy loss process of a charged particle traversing a medium results in a peculiar profile of the depth-dose distribution called *Bragg Curve*, featured by a distinct peak (i.e., the *Bragg Peak*) at the end of the particle range, eventually preceded by a flat plateau. The peak position can be precisely adjusted to the desired depth in tissue by changing the kinetic energy of the incident ions (see Figure 1.2).

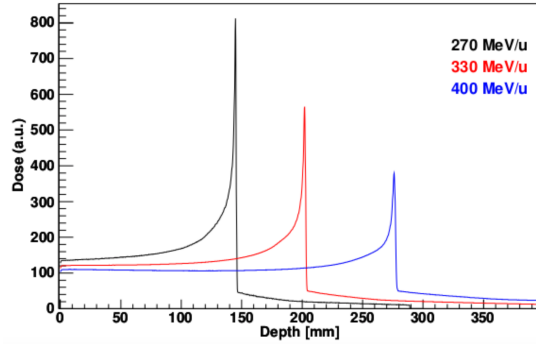


**Figure 1.2:** Depth-dose distributions in water calculated with FLUKA Monte Carlo code [9, 10] for the same number of primary carbon ions at increasing energies [9].

### 1.1.2 Mean range and energy straggling

Given a particle type, beam energy and target material, the mean distance that an ion travels before coming to rest is called *mean range*. It is related to the particle initial kinetic energy  $E_0$  and its energy loss and can be assumed to be equal to the total path length of the particle trajectory in an absorber, defined as follows:

$$R(E_0) = \int_0^{E_0} \left( \frac{dE}{dx} \right)^{-1} dE \quad (1.5)$$

According to Eq.1.5, as the kinetic energy of the primary particle increases the path length becomes longer (see Figure 1.2). The ranges of different ions with

equal initial kinetic energy  $E$  per atomic mass unit and crossing the same absorber scale as  $A/Z^2$ . This means that, given a certain energy per unit mass, heavier ions show a shorter range than lighter ones (Figure 1.3).

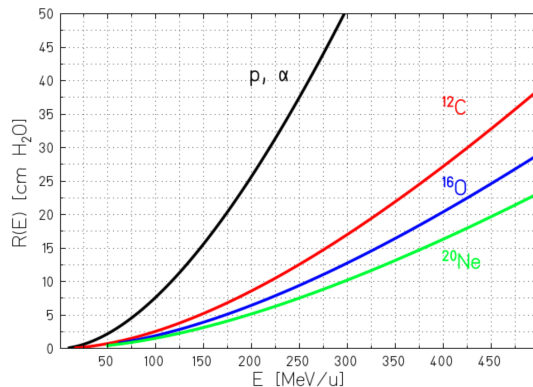


**Figure 1.3:** Mean ranges of several ions in water [8].

For instance, at the same energy per nucleon, the proton range is the same of  ${}^4\text{He}$  ions and approximately three times the range of  ${}^{12}\text{C}$ . According to Eq.1.1, the energy loss of a single ion plotted as a function of the absorber depth would result in a very sharp peak near the stopping point. However, a broadening of the peak can be noticed when an ion beam consisting of many particles cross the medium (see Figure 1.4). This is due to statistical fluctuations of the energy loss in the many collisions of a slowing-down process.

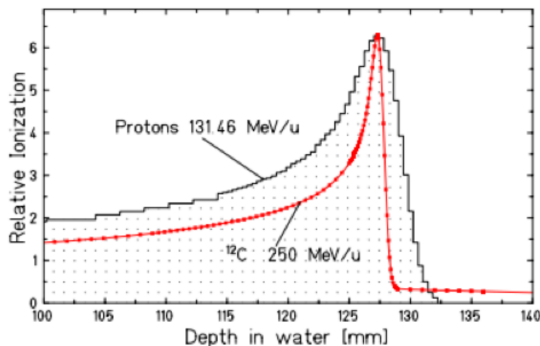


**Figure 1.4:** Measured Bragg peaks of protons and  ${}^{12}\text{C}$  ions having the same mean range in water [8].

These fluctuations cause the so called *energy loss straggling*, well described by the Vavilov distribution for a thin layer of matter [11]. In the limit of many collisions (or a thick absorber), the Vavilov distribution approaches the following

Gaussian form:

$$f(\Delta E) = \frac{1}{\sqrt{2\pi}\sigma} \exp\left(-\frac{(\Delta E - \overline{\Delta E})^2}{2\sigma^2}\right) \quad (1.6)$$

The variance  $\sigma_R^2$  of the range straggling is related to the variance  $\sigma_E^2$  of the energy loss straggling by

$$\sigma_R^2 = \int_0^{E_i} \left(\frac{d\sigma_E}{dx}\right) \left(\frac{dE}{dx}\right)^{-3} dE \quad (1.7)$$

The ratio between the straggling width  $\sigma_R$  and mean range  $R$  is nearly constant and can be described as follows:

$$\frac{\sigma_R}{R} = \frac{1}{\sqrt{M}} f\left(\frac{E}{Mc^2}\right) \quad (1.8)$$

where  $f$  is a slowly varying function depending on the absorber while  $E$  and  $M$  are the particle energy and mass, respectively. Because of the term  $1/\sqrt{M}$ , the relative straggling expressed in Eq.1.8 decreases with increasing mass of the projectile mass, being maximum for protons.

### 1.1.3 Angular straggling

Ions traversing an absorber will undergo small lateral deflections mainly caused by the elastic scattering on the target nuclei and resulting in a spreading of the beam. The statistical distribution function  $F(\theta, d)$  for the scattering angle  $\theta$  at a penetration depth  $x$  is described in the Molière theory [12]. For small angles ( $\theta \simeq 0$ ), the higher order terms in Molière's solution can be neglected and the angular distribution can be approximated by a Gaussian function:

$$F(\theta, x) = \frac{1}{\sqrt{2\pi}\sigma_\theta} \exp\left(-\frac{\theta^2}{2\sigma_\theta^2}\right) \quad (1.9)$$

The standard deviation  $\sigma_\theta$  was calculated by Highland [13]:

$$\sigma_\theta = \frac{13.6MeV}{pv} Z \sqrt{\frac{x}{X_0}} \left[1 + 0.038 \log\left(\frac{x}{X_0}\right)\right] \quad (1.10)$$

where  $X_0$  is the radiation length, whose values can be found in tables,  $x$  is the absorber material thickness, and  $Z$  and  $p$  are charge and momentum of the projectile, respectively. Targets made of heavy elements cause a larger angular spread than targets composed of light elements with the same thickness. Eq.1.10 shows that the angular distribution decreases as the particle momentum rises. Thus,

the lateral spread at the same penetration depth is smaller for heavy ions than, for example, protons at the same velocity (see Figure 1.5).

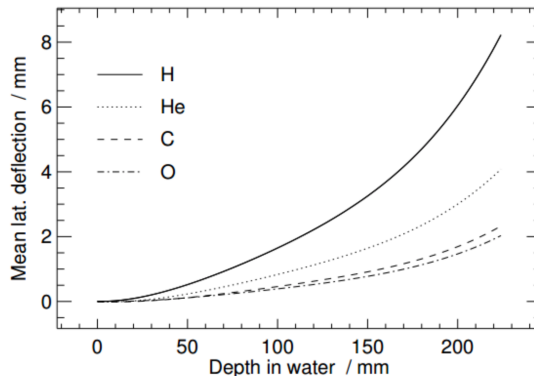


**Figure 1.5:** Lateral deflection in water of some ion beams of clinical interest [6].

#### 1.1.4 Nuclear fragmentation

Along its path, the primary beam undergoes electromagnetic and nuclear interactions with the nuclei of the absorber material. Nuclear reactions classified as *elastic collisions* preserve the involved nuclei charge and the kinetic energy, only contributing in changing the spatial distribution of the beam, and thus are not discussed in this work. Instead, nuclear reactions classified as *inelastic collisions* may cause the break up of target and projectile nuclei, if heavier than a proton, causing the release of secondary particles (i.e., photons, neutrons, protons, heavier ions), thus changing the kinetic energy of each component of the system. The latter are the nuclear reactions of interest in this work. Specifically, projectile fragmentation leads to an attenuation of the primary particles: due to nuclear inelastic processes, a monochromatic incoming beam turns into a mixed beam containing neutral and charged particles. These fragments may have different energy distribution and penetration depth. Thus, they could be responsible for a biological range extension after the Bragg peak or to an increase of biological damage in the plateau region of the Bragg curve, leading to an overestimation of the dose in the healthy tissue region [2].

At energies of several hundreds megaelectronvolts per atomic mass typical in radiotherapy and space radioprotection applications, violent nuclear spallation reactions may result in a partial fragmentation or complete disintegration of both the projectile and target nuclei. In the latter kind of reaction, both the colliding partners are involved in what is called a *central* (or *near central*) collision. However, the most frequent nuclear reactions are peripheral collisions, in which particles lose

one or more nucleons. This process can be described with the two steps model of *abrasion-ablation* [14], illustrated in figure 1.6.

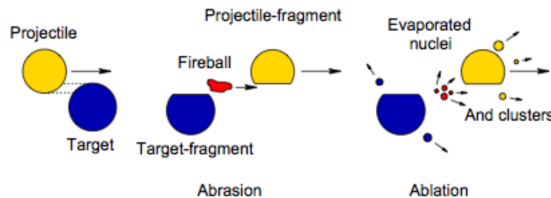


**Figure 1.6:** A simplified model of the nuclear fragmentation due to peripheral collisions of projectile and target nucleus as described by [14].

In the fast stage (*abrasion*), the nucleons within the overlapping zone of the projectile and target nuclei interact with each other and are sheared away, forming the hot reaction zone, named “fireball”. The projectile fragments follow the initial trajectory with approximately the same velocity prior the interaction, while target fragments slowly recoil. Projectile fragments are distributed in a small angle in the forward direction, but the spread of the lighter fragments (protons and helium ions) enhance the lateral broadening of the beam. They could have a lower charge and mass with respect to the primary beam, resulting in a longer range than the beam particles. Therefore, they generate a longitudinal tail in the dose deposition curve delivering an unwanted dose beyond the BP. Target fragments, instead, are produced at a very low velocity and therefore they can travel a very short range, of the order of tens of  $\mu\text{m}$ . They are mostly relevant in proton therapy, where no beam fragmentation occurs. The residual projectile and target fragments as well as the fireball are excited as a result of the *abrasion* process and they later dissipate their energy by undergoing particle evaporation (*ablation*). Only few nucleons in the overlap zone between the projectile and target nuclei effectively interact during the collision, so the number of participant nucleons is small. As a result of the *abrasion-ablation* process, projectile fragments either “scraped off” from the direct overlap of the nuclei either originate from the de-excitation of the projectile residue and target fragments produced as evaporation products from the excited target residue are observed. The former mostly move in the forward direction at velocities approximately equal to that of the projectile, the latter are observed to have an almost isotropic distribution in the laboratory frame.

The *nuclear cross section* is a key parameter for the description of nuclear interactions, since it links the probability that a nuclear reaction will occur with given beam and target properties, and it can be defined as follows:

$$\sigma = \frac{N}{N_i} \frac{A}{\rho x N_A} \quad (1.11)$$

where  $N$  is the number of interactions and  $N_i$  the number of incoming particles, while  $\rho$ ,  $A$  and  $x$  are the target density, mass number and thickness, respectively. The cross section is conventionally measured in barn ( $b$ ), where  $1b = 10^{-28} \text{ m}^2 = 100 \text{ fm}^2$ . We refer to *differential*  $\left(\frac{d\sigma}{d\Omega}; \frac{d\sigma}{dE}\right)$  or *double-differential cross sections*  $\left(\frac{\partial^2\sigma}{\partial\Omega\partial E}\right)$  when the term  $N$  in Eq. 1.11 includes only particles produced in a certain solid angle portion  $d\Omega$  or in a certain energy range  $dE$ . Moreover, the cross section evaluation can be restricted to the production of a specific fragment charge or isotope in order to describe the probability to generate that particle.

## 1.2 Interaction of neutral particles with matter

### 1.2.1 Neutrons

Since neutrons carry no charge, they interact only weakly with matter into which they can penetrate deeply. As a result of the interaction between neutron and nucleus of the absorbing material, the neutron may either disappear and be replaced by one or more secondary radiation, or else the energy or direction of the neutron is changed significantly. There are two types of neutron interaction processes:

- *Elastic and inelastic scattering* with a target nucleus, which leads to a changing in the neutron speed and direction, leaving the nucleus with the same number of protons and neutrons it had before the interaction. During an elastic scattering the total kinetic energy of the neutron and nucleus is unchanged by the interaction. The average energy transferred from a neutron of kinetic energy  $E$  to a nucleus of mass  $A$  is:

$$\frac{2EA}{(A+1)^2} \quad (1.12)$$

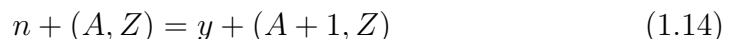
Thus, light or rich in protons materials are the most effective in reducing the energy of neutrons with a fewest number of interactions. In general after  $n$  collisions, the initial energy  $E_0$  of a neutron is expected to be reduced to:

$$E_n = E_0 \left[ \frac{A^2 + 1}{(A+1)^2} \right]^n \quad (1.13)$$

Instead, in an inelastic scattering process part of the initial neutron kinetic energy is used to place the nucleus into the excited state, from which it eventually releases radiation. Thus, the total kinetic energy of the neutron

and the nucleus is not preserved anymore. The average energy loss depends on the energy levels within the nucleus, thus is not easy to write an expression for it. Anyway, the effect is again to reduce neutron velocity and change its direction.

- *Absorption* of the neutron by the target nucleus, resulting in a wide range of radiations that could be emitted. Even though the nucleus may rearrange the internal structure and release one or more gamma rays, the secondary radiation resulting from neutron interactions is almost always charged particles. The absorption process can be described as follows:



Finally, there maybe a fission event, leading to two or more fission fragments (nuclei of intermediate atomic weight) and additional neutrons.

The probability for a specific type of interaction to occur, change dramatically with the neutron energy. Neutrons with energy spanning from hundreds of keV to hundreds of MeV (referred to as *fast neutrons*) can transfer an appreciable amount of energy in a single collision, thus they mainly interact via elastic or inelastic scattering with the target nuclei. The latter occurs only if their energy is sufficiently high to excite the target nuclei. The traversing process of a fast neutron through a thick absorber material can be described by several scattering processes of two free particles, where at each step the neutron slows down according to a process called *moderation* [15]. Instead, neutrons with low energy below some keV can be absorbed by the target nucleus. The absorption process becomes dominant if the neutron is in thermal equilibrium with the absorber atoms.

### 1.2.2 Photons

The energy loss mechanisms of photons are of interest in nuclear fragmentation experiments due to their large production in the process and their usefulness for the time-of-flight measurement (see Sec. 3.2). Photons transfer their partial or total energy to a bound electron of the target atom through three main mechanisms:

- *Photoelectric absorption*. The photon interacts with a bound electron of the absorber nucleus and transfers all its energy, leading to the ejection of a so called *photoelectron* with an energy:

$$E_e = h\nu - E_b \quad (1.15)$$

where  $h$  is the Planck constant,  $\nu$  the frequency of the impinging photon and  $E_b$  the binding energy of the electron in its original shell. In this process the

atom is left in an ionized state due to the loss of the electron, thus it deexcites either by the capture of a free electron or by the rearrangement of the shell electrons with a possible further photons or electrons emission. Photoelectric absorption is the dominant energy loss process for low energetic photons and high-Z absorbers (see Figure 1.8). In fact, the probability of photoelectric absorption varies as

$$\propto \frac{Z^n}{h\nu^3} \quad (1.16)$$

where  $Z$  is the atomic number of the target material,  $n$  can vary between 4 and 5 and  $h\nu$  is the energy of the impinging photon.

- *Compton scattering.* The photon scatters on a bound electron and transfers part of its energy to the latter (see Figure 1.7(a) ). Because all scattering angles are possible, the energy transferred to the electron can vary up to a large fraction of the initial photon energy.
- *Pair production.* If the photon energy exceed two times the rest mass of the electron (1.022 MeV), a photon can interact with the nucleus of the target vanishing and being replaced by a newly created electron-positron pair (see Figure 1.7(b) ). The energy of the pair is:

$$E_{e^+} + E_{e^-} = h\nu - 1.022MeV \quad (1.17)$$

The probability related to the pair production process for a given absorber increases with increasing photon energy and for a given photon energy increases approximately with the  $Z^2$  of the absorbing material.

Usually, photons emitted by the rearrangement of the electron shells of an atom are typically referred to as *X-rays* while photons emitted by energy level transitions of the nucleus itself are named  *$\gamma$ -rays*.

### 1.3 Application of nuclear interaction in research

As discussed in Sec. 1.1 and 1.2.1, the interaction of charged and neutral particles with the traversed matter produces electrons, which scatter elastically and inelastically in the medium. For electrons with energy lower than 50 eV inelastic scattering of the electrons causes an excitation of the medium. For higher energies instead, electron scattering causes ionizations that create additional electrons [8]. The created electron can directly interact with the DNA. Moreover, the excitation of the surrounding molecules may convert into free radicals, which are atoms or molecules having unpaired electrons. Thus, they are highly reactive and their probability of interaction with DNA molecule is high. The probability of inducing

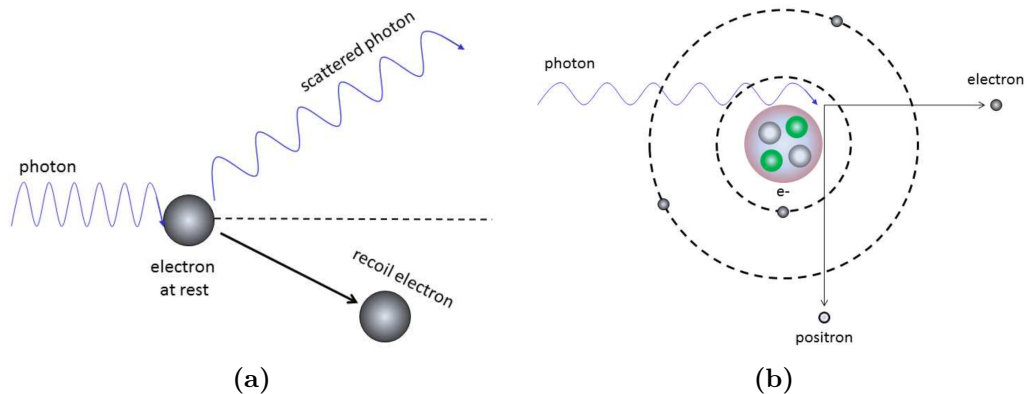


**Figure 1.7:** (a) Scheme of the Compton scattering mechanism. The impinging photon is scattered inelastically on an electron and transfers parts of its energy, depending on the scattering angle; (b) Scheme of the pair production process. A photon of sufficient energy ( $>1.022$  MeV) impinging on a nucleus produces an electron-positron pair. The positron will later annihilate with an electron by emitting two 511 keV photons at opposite directions to each other.

a certain type of damage, is mostly related to the amount of energy released by a radiation in the traversed material. Charged particles are characterized by a high energy transfer associated with a localized energy deposition resulting in the induction of enhanced and unreparable biological damages. On one hand, the main goal of particle therapy is to exploit radiation to selectively induce a damage to the body tumoral site in order to kill malignant cells. On the other hand, space radiation protection deals with the preservation of astronaut's health from the exposure to radiation.

### 1.3.1 Particle therapy

The use of nuclear particles to treat tumors was experimented by the first pioneers during the half of the last century. Charged particles radiotherapy using proton beams was first proposed for clinical application by R. Wilson in 1946 [16], who recognized that the sharp peak of energy deposition curve would offer potential benefits to radiotherapy and thus started a detailed study about proton therapy. Radiotherapy with heavier ions began in 1975 with Tobias et al. [17] at the Bevalac facility at Lawrence Berkeley Laboratory (LBL) in USA, where most of the patient treatments were performed with  $^{20}\text{Ne}$  beams. In 1994 the Heavy-Ion Medical Accelerator (HIMAC) started with carbon ions at National Institute of Radiological Science (NIRS) in Chiba (Japan). At the same time new technical solutions were developed almost in parallel in Switzerland at Paul Scherrer Institute (PSI) and in

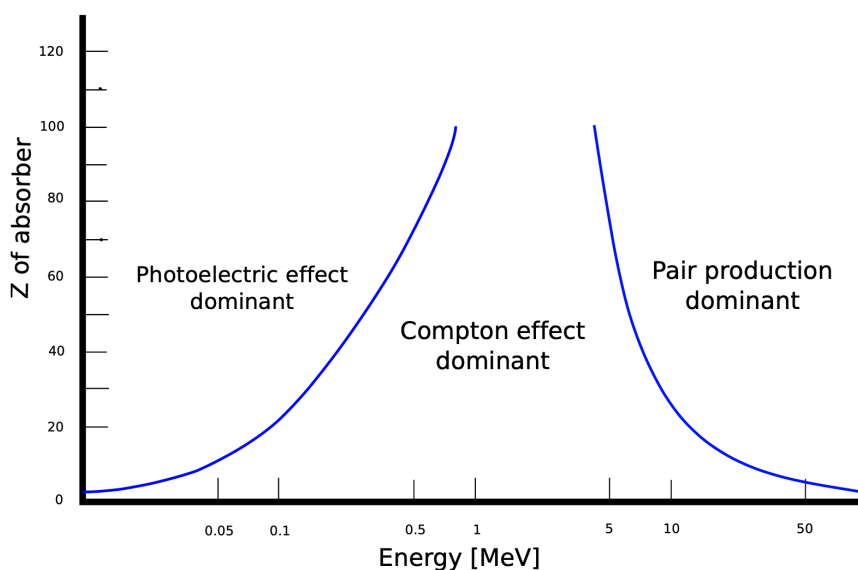


**Figure 1.8:** Probability of the three main interaction mechanisms of photons with matter as a function of their energy. At low photon energies and for absorbers with high atomic numbers photoelectric absorption is predominant. At intermediate energies up to some MeV Compton scattering dominates for any target atomic number. At higher energies the probability for pair production increases with the square of the atomic number of the absorber and increasing photon energy.

Germany at Helmholtzzentrum für Schwerionenforschung (GSI), differing significantly from the previous design adopted at Bevalac and HIMAC. To date, protons and carbon ion radiotherapy has been studied for almost every type of malignancy, including intracranial malignancies, head and neck malignancies, primary and metastatic lung cancers, tumors of the gastrointestinal tract, prostate and genitourinary cancers, sarcomas, cutaneous malignancies, breast cancer, gynecologic malignancies, and pediatric cancers. The rationale of using ions in radiotherapy lies mainly in their favorable depth-dose profile. While electromagnetic radiation (X-rays and megavolt photon beams) shows a steep exponential decrease of dose with depth, charged particles (at present, protons and  $^{12}\text{C}$  ions are the most widely used in particle therapy) exhibit a flat plateau region at the entrance channel and a distinct peak near the end of their range, the so called *Bragg Peak* (BP) (Figure 1.9(a)). Thus, low levels of energy are deposited in tissues proximal to the target volume, and the majority of energy is released inside the target. Distal tissues receive little energy, although, unlike protons, there is energy deposited distally due to carbon nuclear fragmentation [18], as already explained in Sec. 1.1.4.

The position of the peak can be precisely adjusted to the desired depth in tissue by changing the kinetic energy of the incident ions. Protons used in therapy are

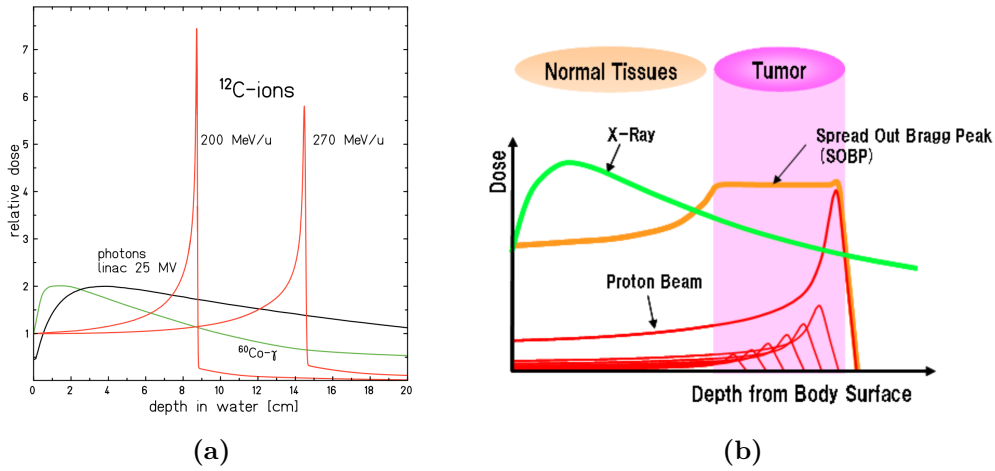


**Figure 1.9:** (a) Depth dose profile of electromagnetic radiation ( $^{60}\text{Co}$  and linear accelerator (linac) spectrum) and Carbon ( $^{12}\text{C}$ ) ions in water [8]; (b) Comparison between dose (Gy) distribution of X-rays and of a SOBP obtained by superimposing several BPs as a function of penetration depth (cm) inside the patient.

accelerated to energies ranging between 60 and 250 MeV, that corresponds to a 15-35 cm range in water, while to reach the same penetration depths, carbon ions must have about a doubled energy. This peculiar behavior of charged particles can be exploited for optimizing the conformality of the dose in the treatment. However, a single monoenergetic beam produces a BP which is too narrow to irradiate the entire cancer volume, therefore several BP with different energies are combined to create the so called *Spread Out Bragg Peak (SOBP)*, so that a uniform dose is delivered in the longitudinal profile across the tumor volume (Figure 1.9(b)). Due to the high spatial precision of charged particle dose deposition, particle therapy treatments are more sensitive to beam range uncertainties than conventional photon treatments. A wrong estimation of the range produces a shift of the BP position, leading to an under-dosage of the tumor volume and an over-dosage of healthy tissue placed before or beyond the tumor. Common error sources are patient motion (e.g. breathing), anatomical changes (for example tumor regression or patient weight loss) occurred during the duration of the treatment (which ranges between two and eight weeks, according to the tumor size, the prescribed total dose and the particle used) and others. One more currently neglected error source could be related to the approximation made by treatment planning system to model the interaction of the primary beam with tissue by rescaling the data in water accordingly. However, the accuracy of this approximation depends on the differences between the tissue elemental composition and water. In particular, this imprecision might limit the accuracy of the treatment planning system if the physical and chemical properties

of the transverse material differ significantly from water, as for bones, which are characterized by a relatively high calcium abundance. Recent studies focused on the evaluation of the dose error when a conventional tissue to-water conversion to model nuclear interactions is applied [19, 20, 21]. Therefore, experimental data measured in specific biological tissues are of paramount importance to find a correction method for improving the treatment planning accuracy.

### 1.3.2 Space radiation protection

The pool of particle species either currently available in radiotherapy (protons and carbon) or considered promising alternative candidates (i.e., helium, lithium and oxygen) are among the most abundant in the space radiation environment. Moreover, the optimum energy range for proton therapy is the same of the solar flare protons and Van Allen trapped protons. Therefore, the shared interest of ion species and energy range between hadrontherapy and space radioprotection allows the interchange of cross sections data. In fact, because radiation environment in space can lead to serious health risks for astronauts, NASA and other space agencies have started since several years the study of the risk assessment for astronauts especially in long duration and far from Earth space missions (like human explorations to Mars [22]). There are three main sources of energetic particles in space: Solar Particle Events (SPEs), Galactic Cosmic Rays (GCR) and the geomagnetically trapped particles.

SPEs are mainly composed by protons emitted from the Sun during coronal mass ejections and solar flares. Even though very large SPEs are rare, their energy spectrum can reach the GeV region and, being unpredictable, they can inflict a lethal dose to the astronauts and affect the stability of electronic devices [23].

GCRs consist of high energy protons and highly energetic charged particles originated from supernovae within the Milky Way Galaxy. GCR particles have energies from 10 MeV/u to the ZeV region (Zetta eV =  $10^{21}$  eV). The peak of the spectrum is in the hundreds of MeV to GeV range [23]. The elemental abundance and energy spectrum of GCRs are well known (86% of protons, 12% of alpha particles, 1% of heavier ions like carbon, silicon and iron), but their biological effects are poorly understood, even though they are one of the most significant hazard for humans in space. As a matter of fact, the GCR radiation cannot be easily shielded because of the nuclear fragmentation into lighter and thus more penetrating ions.

Finally, the geomagnetically trapped particles consist of protons and electrons confined by the Earth magnetic field in two regions, called Van Allen belts. Protons reach energies up to a few hundreds MeV in the inner belt and electrons up to 100 keV in the outer belt. Obviously, GCRs and SPEs are the most critical radiation for the astronauts' health protection during deep space exploration outside the magnetosphere of our planet. A fundamental tenet of radiation protection is that

there are three means to reduce exposure to ionizing radiation: increasing the distance from the radiation source, reducing the exposure time, and by shielding. Distance is not an issue in space, GCR being isotropic. Time in space should be increased rather than decreased according to the plans of exploration and colonization. Clearly, the only effective countermeasure left is passive shielding, whose design and optimization require a detailed knowledge of the fragmentation processes. In fact, the radiation spectra are modified when particles traverse a spacecraft wall due to the atomic and nuclear reactions occurring. As discussed in Sec. 1.1.1 and 1.1.4, the mass stopping power  $S/\rho$  and the fragmentation cross-section per unit target mass  $\sigma_T/A_T$  show an inverse dependence on the atomic weight  $A_T$  of the target ( $Z_T$  is the atomic number of the target).

$$\frac{S}{\rho} = \frac{Z_T}{A_T} \quad (1.18)$$

$$\frac{\sigma_T}{A_T} = A_T^{-1/3} \quad (1.19)$$

Therefore, light materials are more effective for shielding in space. Liquid hydrogen has the maximum performance as shield material, but is not a practically feasible being a low-temperature liquid. Instead, polyethylene can be a good compromise and NASA has used aluminum panels with lighter polyethylene slabs in the crew sleeping quarters on International Space Station (ISS). MC transport codes are extensively used to study the cosmic rays propagation through these and other various media of interest for space applications in order to characterize the radiation spectrum inside the spacecraft and determine the accumulated radiation dose that an astronaut receives. Therefore, experimental data for beam and targets combinations relevant in space radiation applications must be collected for characterizing the interaction of mixed generated radiation field and assess the consequent radiation-induced health risk, as well as to benchmark the MC codes. Such experiments will be of great help to select innovative shielding materials and provide recommendations on space radioprotection for different mission scenarios.

## 1.4 Experimental cross sections

Literature is quite rich in experimental data of nuclear cross sections, but there is a gap in the measurements for light particles species ( $A < 20$ ) currently employed in particle therapy and abundant in the space radiation environment. Moreover, the energy gap in the available measurements is in the therapeutic (between tens and few hundreds of MeV/u) and space radioprotection (between few hundreds of MeV/u to tens of GeV/u) range of interest.

### 1.4.1 Particle therapy

Being the human body mostly composed of hydrogen, carbon, oxygen and nitrogen, water or plastic are the ideal target choice in biological radiation measurements [24, 25]. The available experimental data for the above mentioned targets and a proton incident beam drawn from the EXFOR [26] and Landolt-Börnstein [27] databases were compared to the prediction of different models used for hadron-therapy studies, such as TALYS [28], INCL [29] and ICRU63 [30]. Figures show reaction cross sections (Figures 1.10) and isotopic production cross sections (Figure 1.11, 1.12, 1.13, 1.14) for protons on  $^{12}\text{C}$ ,  $^{16}\text{O}$  and  $^{40}\text{Ca}$  targets. Discrepancies between experimental data and models are pronounced for the isotopic production cross sections at high energies, confirming that models are not able to reproduce experimental data with great accuracy as required in proton therapy applications. Recently, the interest of the particle therapy community focused on the study of ion beams, such as carbon, helium and oxygen, as new and promising ions for cancer treatment purposes. Energy spectra (Figures 1.15, 1.16), angular distributions and yields of H and He isotopes for a 200 MeV/u  $^{12}\text{C}$  ion beam incident on a 12.8 cm water target were performed at GSI (Darmstadt, Germany), in order to investigate the treatment of deep-seated medium-sized tumours in the head and neck region [31]. Double differential fragmentation cross sections and fragments angular distribution (Figure 1.17) of a 95 MeV/u  $^{12}\text{C}$  ion beam on different targets (i.e.,  $\text{C}$ ,  $\text{CH}_2$ ,  $\text{Al}$ ,  $\text{Al}_2\text{O}_3$ ,  $\text{Ti}$  and  $\text{PMMA}$ ) for twenty different angles were measured at GANIL (France), providing spectra of fragments ranging from protons to carbon ion isotopes [32]. Differential fragmentation cross sections measurements of 400 MeV/u  $^{12}\text{C}$  ion beam on C and Au targets were performed at GSI in the frame of the FIRST (Fragmentation of Ions Relevant for Space and Therapy) experiment [33]. Fluxes and kinetic energy spectra of H and He isotopes generated at five different angles with respect to the beam direction in the fragmentation process of 102 MeV/u, 125 MeV/u and 145 MeV/u He beams interacting with a beam stopping PMMA target were measured at the HIT (Heidelberg Ion-beam Therapy) center (Figure 1.18) [34]. A similar work performed at GSI measured the angular distribution and kinetic energy spectra (Figure 1.19) of fragments generated by 120 MeV/u and 200 MeV/u  $^4\text{He}$  beams on PMMA and water targets. The presented experimental results indicate a general gap of measurements in the therapeutic energy range (100 - 400 MeV/u). Fragmentation cross sections data describing the loss of the primary particles and the build up of secondary fragments are required in order to benchmark the existing MC simulation toolkits and the algorithms presently implemented in the TPS.

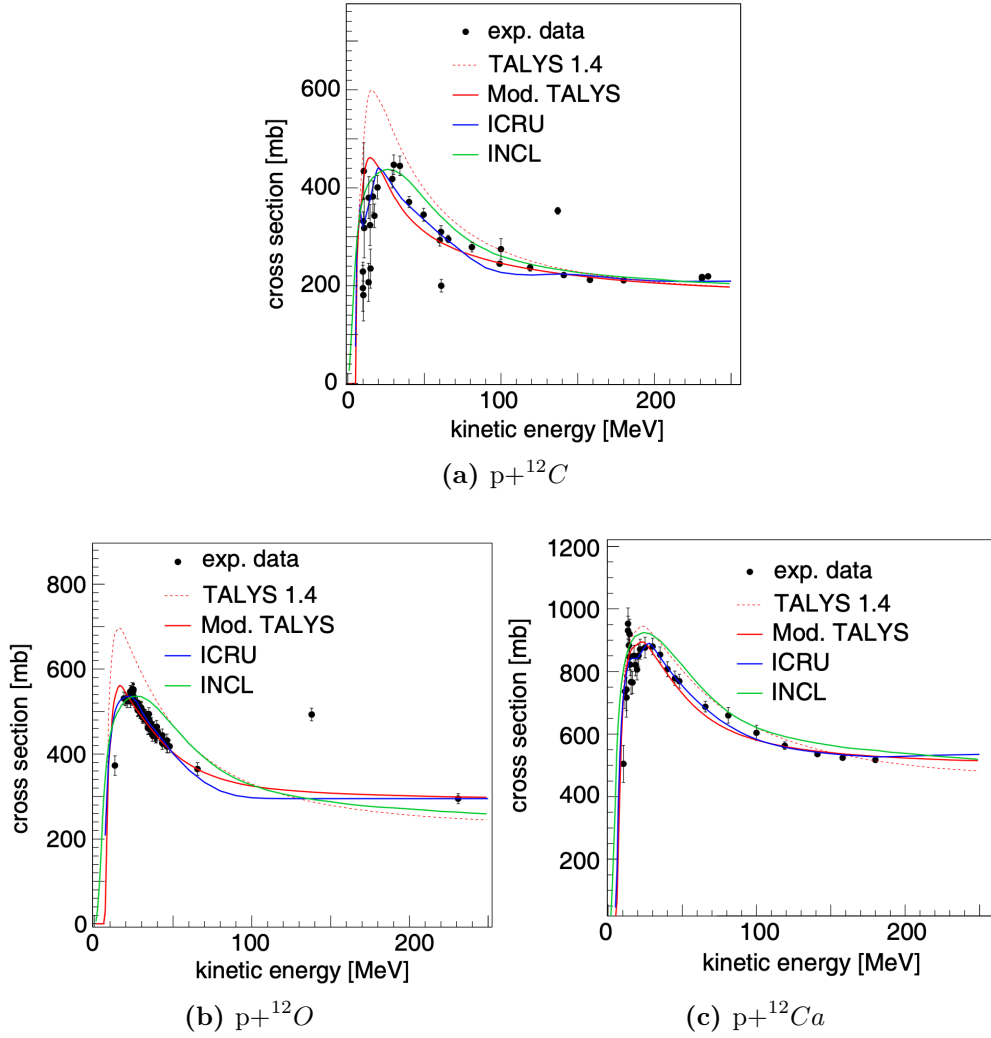


**Figure 1.10:** Reaction cross sections for  $p+^{12}\text{C}$  (a),  $p+^{12}\text{O}$  (b) and  $p+^{12}\text{Ca}$  (c) reaction cross section. Experimental data are drawn from the EXFOR database and are represented by black dots; results of TALYS 1.4 (dashed red), Modified TALYS (solid red), ICRU (solid blue) and INCL (solid green) are also shown.

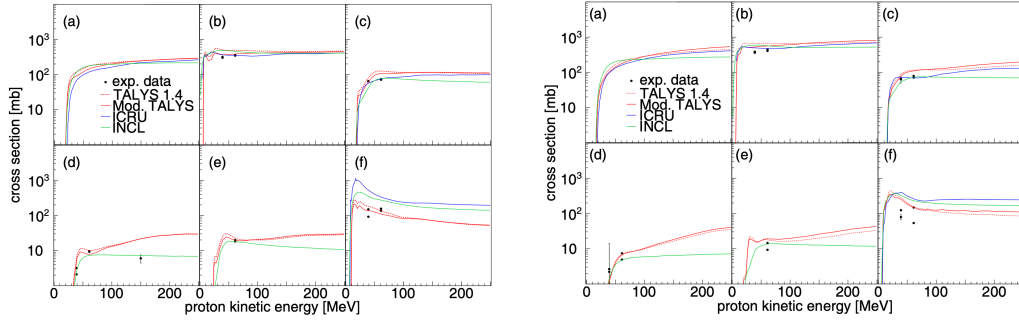


**Figure 1.11:** Reaction cross sections for the production of (a) neutrons, (b) protons, (c) deuterons, (d) tritons, (e)  $^3\text{He}$  and (f)  $^4\text{He}$  from a proton beam interacting with a  $^{12}\text{C}$  target (left panel) and  $^{16}\text{O}$  target (right panel). Experimental data are taken from [27] and are represented by black dots; results of TALYS 1.4 (dashed red), Modified TALYS (solid red), ICRU (solid blue) and INCL (solid green) are also shown.

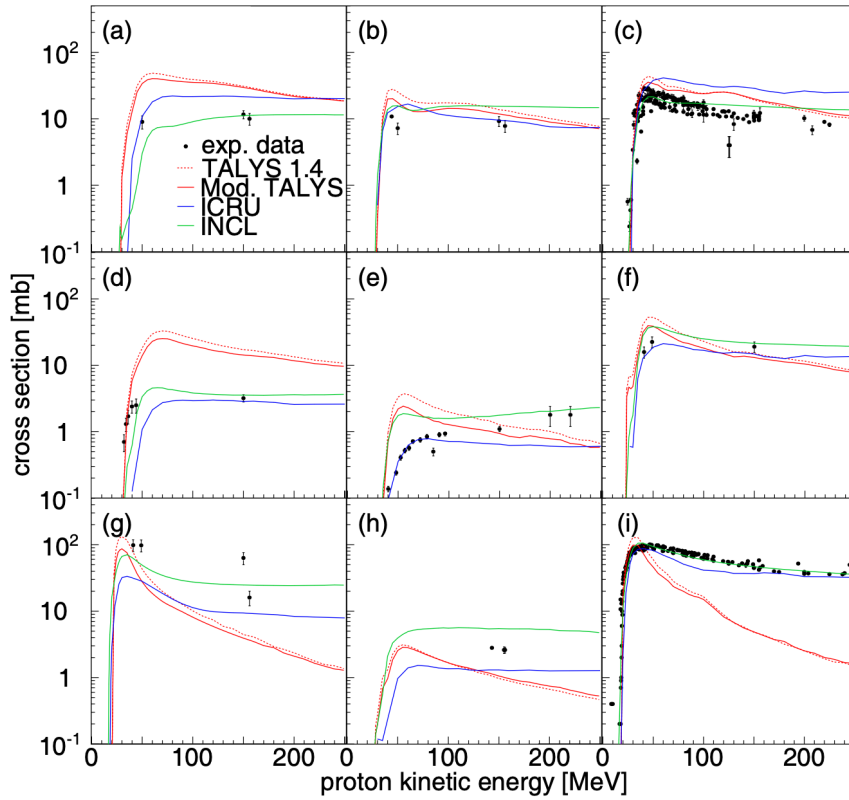


**Figure 1.12:** Reaction cross sections for the production of (a)  $^6\text{Li}$ , (b)  $^7\text{Li}$ , (c)  $^7\text{Be}$ , (d)  $^9\text{Be}$ , (e)  $^{10}\text{Be}$ , (f)  $^{10}\text{B}$ , (g)  $^{11}\text{B}$ , (h)  $^{10}\text{C}$  and (i)  $^{11}\text{C}$  for a proton beam on  $^{12}\text{C}$  target [24].

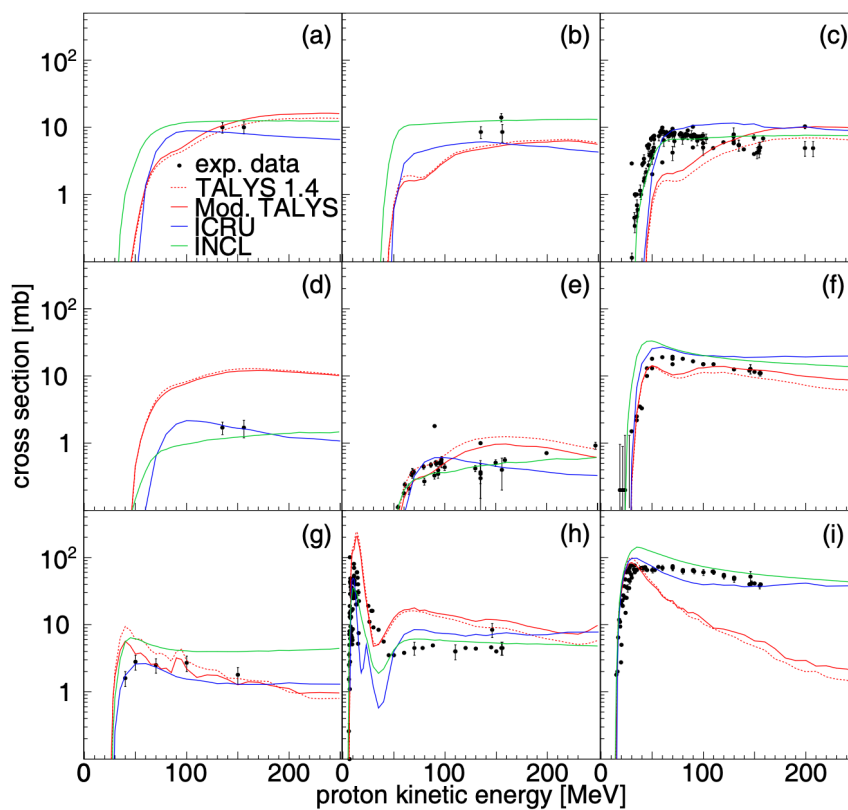


**Figure 1.13:** Reaction cross sections for the production of (a)  ${}^6\text{Li}$ , (b)  ${}^7\text{Li}$ , (c)  ${}^7\text{Be}$ , (d)  ${}^9\text{Be}$ , (e) (f)  ${}^{11}\text{C}$ , (g)  ${}^{14}\text{C}$ , (h)  ${}^{13}\text{N}$  and (i)  ${}^{15}\text{O}$  for a proton beam on  ${}^{16}\text{O}$  [24].

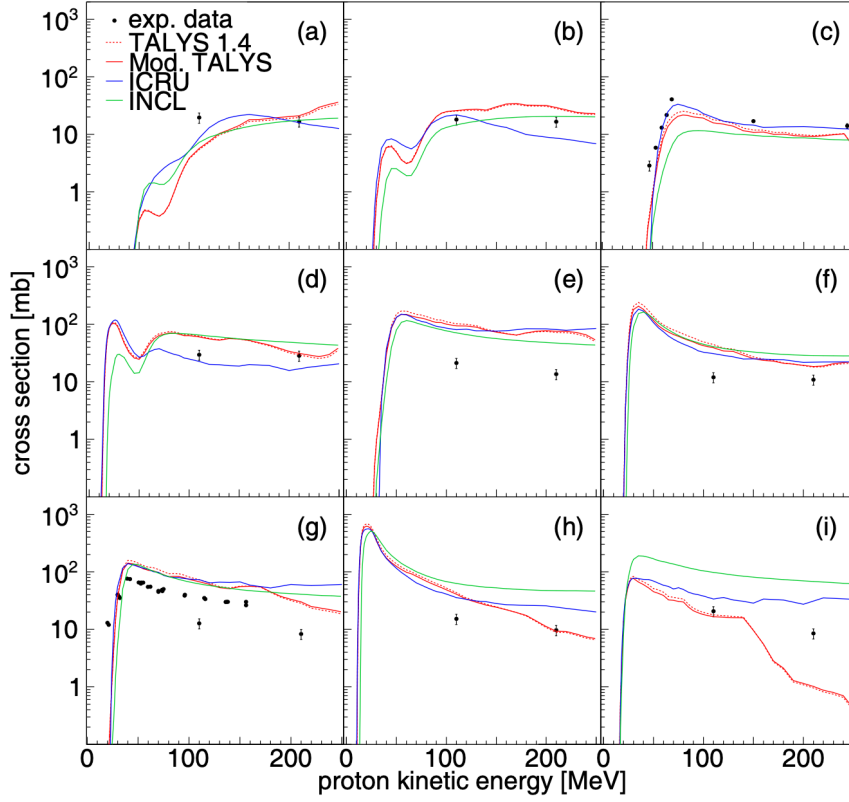


**Figure 1.14:** Reaction cross sections for the production of (a) <sup>28</sup>Si, (b) <sup>32</sup>S, (c) <sup>36</sup>Cl, (d) <sup>36</sup>Ar, (e) <sup>37</sup>Ar, (f) <sup>38</sup>Ar, (g) <sup>38</sup>K, (h) <sup>39</sup>K and (i) <sup>39</sup>Ca for a proton beam <sup>40</sup>Ca [24].

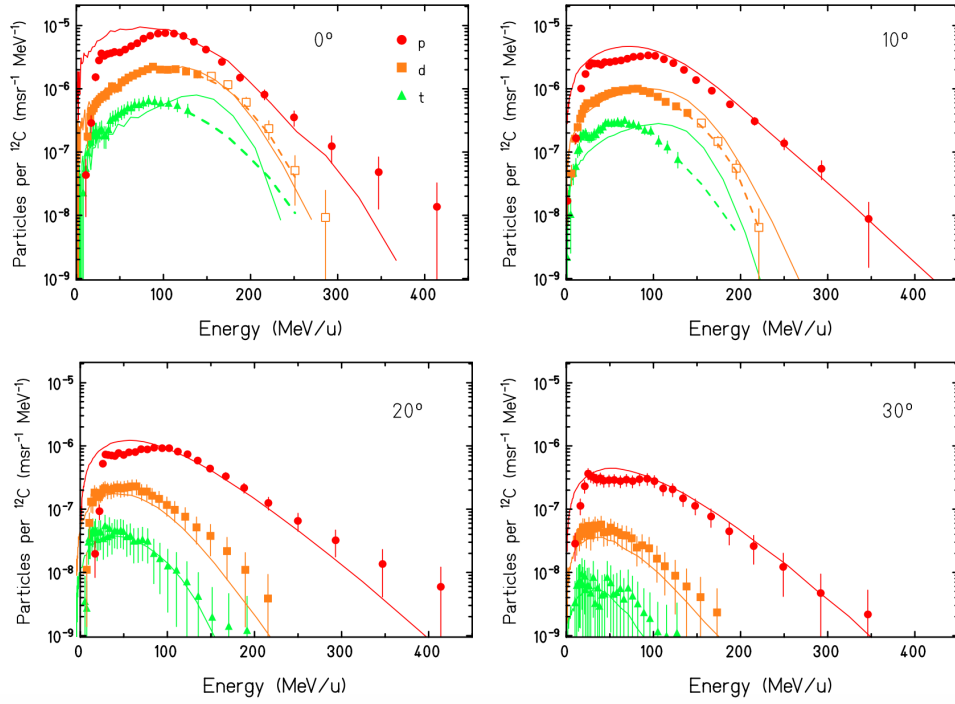


**Figure 1.15:** Energy spectra of secondary protons, deuterons and tritons measured at forward angles from  $0^\circ$  to  $30^\circ$ . The data are compared with simulations of the Monte-Carlo code PHITS (solid lines). The dashed lines indicate an estimated decomposition. [32]

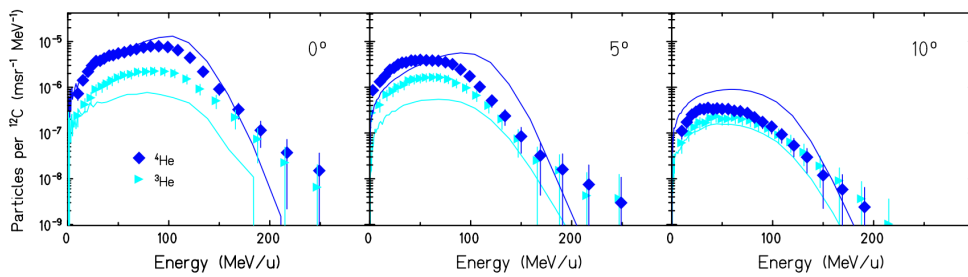


**Figure 1.16:** Energy spectra of secondary  $^3\text{He}$  and  $^4\text{He}$  isotopes measured at forward angles from 0 deg to 10 deg. The data are compared with simulations of the MC code PHITS (solid lines) [32].

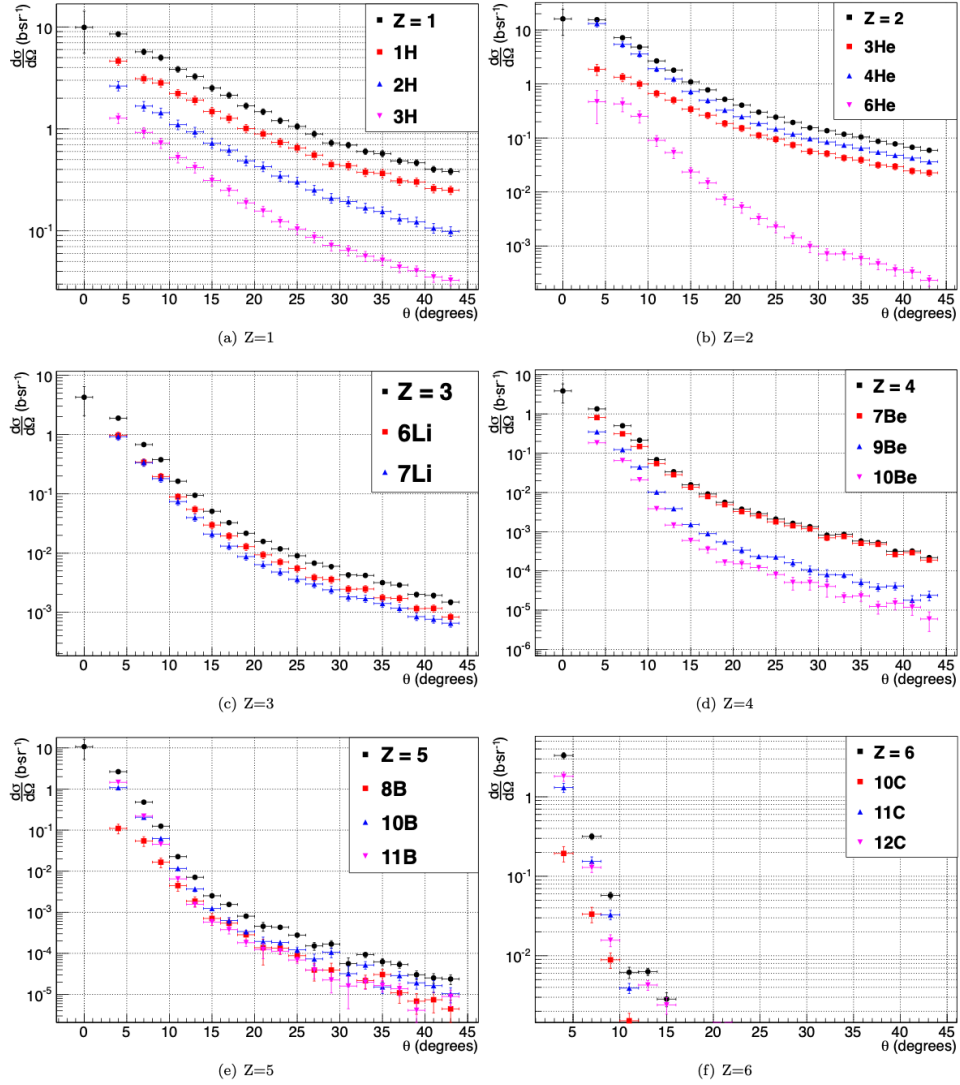


**Figure 1.17:** Angular distributions of fragments resulting from the fragmentation of 95 MeV/u  $^{12}\text{C}$  ions beam on a graphite target. The distributions of the different isotopes are superimposed.

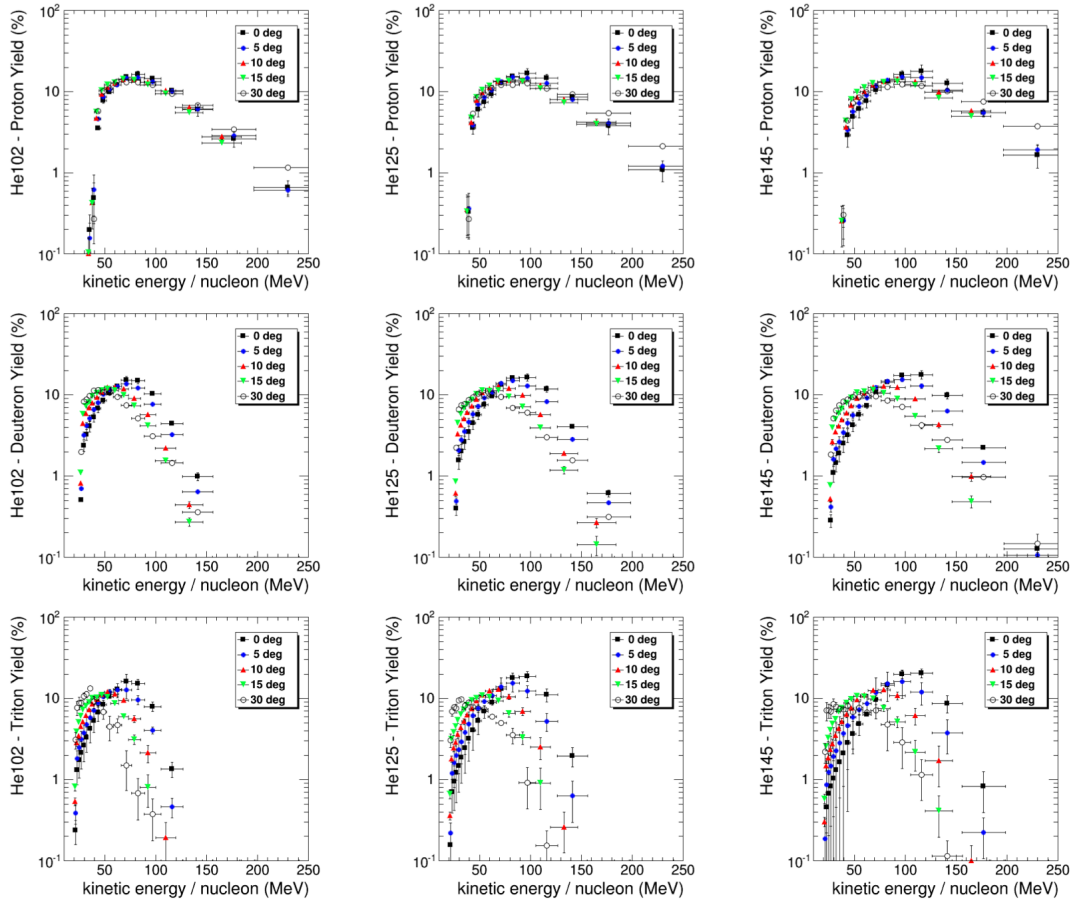


**Figure 1.18:** Relative yield of protons (top plots), deuterons (center), and tritons (bottom) as a function of nucleon kinetic energy for different angles with 102 MeV/u (left plots), 125 MeV/u (center) and 145 MeV/u (right)  $^4\text{He}$  beams [34].

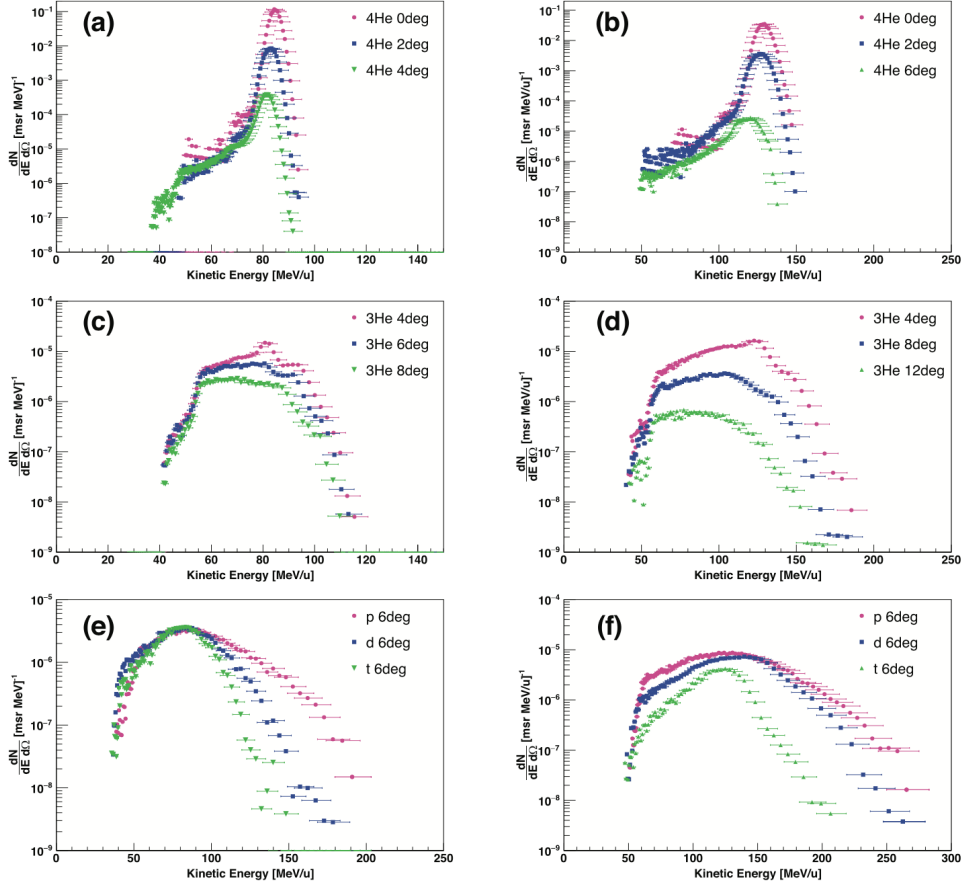


**Figure 1.19:** (a)-(b) Kinetic energy spectra of the primary  $^4\text{He}$  ions with initial energy of 120 MeV/u and 200 MeV/u interacting with a 4.28 and 13.96 cm water target respectively; (c)-(d) Kinetic energy spectra of  $^3\text{He}$  produced by 120 MeV/u and 200 MeV/u  $^4\text{He}$  on 4.28 and 13.96 cm of water respectively; (e)-(f) Kinetic energy spectra of protons, deuterons and tritons produced by 120 MeV/u and 200 MeV/u  $^4\text{He}$  on 4.28 and 13.96 cm of water respectively [35].

## 1.4.2 Space radiation

For the space exploration risk assessment, the atomic and nuclear interactions occurring between the incoming particles and the shielding material of the spacecraft have to be characterized in order to know the composition and energy of particles spectra inside the vessel and at various sites of the solar system. The galactic cosmic ray spectrum shows local peaks in abundance (Figure 1.20) for  ${}^1_1\text{H}$ ,  ${}^4_2\text{He}$ ,  ${}^{12}_6\text{C}$ ,  ${}^{16}_8\text{O}$ ,  ${}^{28}_{14}\text{Si}$ ,  ${}^{55}_{26}\text{Fe}$ , where charge numbers are indicated as lower case. These six nuclei represent the most important contributions to dose in unshielded deep space [36]. For particle energies higher than 10 GeV/n the contribution of nuclear reactions in the energy deposition is dominating. Even though experiments with projectile nuclei from hydrogen to uranium with energies up to 100 GeV/u can be useful to calibrate theoretical models and perform space electronics research, the most relevant ions in the GCR spectrum in the energy range from  $\sim 100$  MeV/n to  $\sim 10$  GeV/n are H and He [37]. Nevertheless, they are also the most important for GCR studies due to their high penetrating power and their large angular spread from the beam [23]. Each symbol of the plots in Figures 1.21 and 1.22 represents all the protons and  ${}^4\text{He}$  cross section measurements available relevant to space radiation as a function of the target and projectile charge [23], while Figures 1.23 and 1.24 show the same available data for heavier fragments [23]. The kinetic energy regions of the plots are typically broken down into four region, namely below the pion threshold at 280 MeV/n, then up to 3 GeV/n and 15 GeV/n chosen to overlap experiments performed at the *Berkeley Bevalac* and the *Brookhaven Alternating Gradient Synchrotron (AGS)* with typical beam energies of 2.1 GeV/n and 14.6 GeV/n, respectively. Hydrogen targets are of particular interest to cosmic ray transport and space radiation shielding, since hydrogenous materials have highly favorable properties for shielding against charged nuclei [36]. The plots show that there are a surprisingly large number of gaps in the experimental data concerning the important galactic cosmic ray nuclei mentioned above in the energy range relevant for space exploration (medium and high). This represents a significant gap in validating theoretical models and need to be filled with more experimental campaign, such as the ones proposed by the FOOT experiment (see Sec. 2.2).

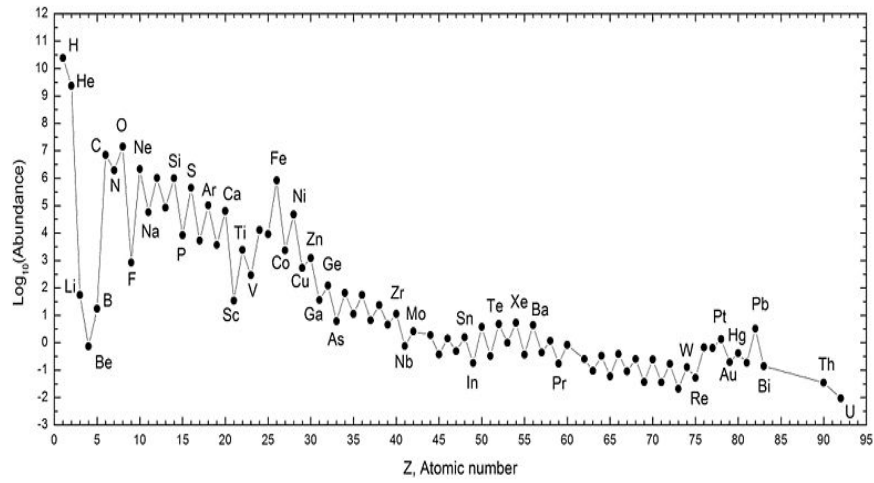


Figure 1.20: Cosmic rays element abundance normalized at Silicon [37] .

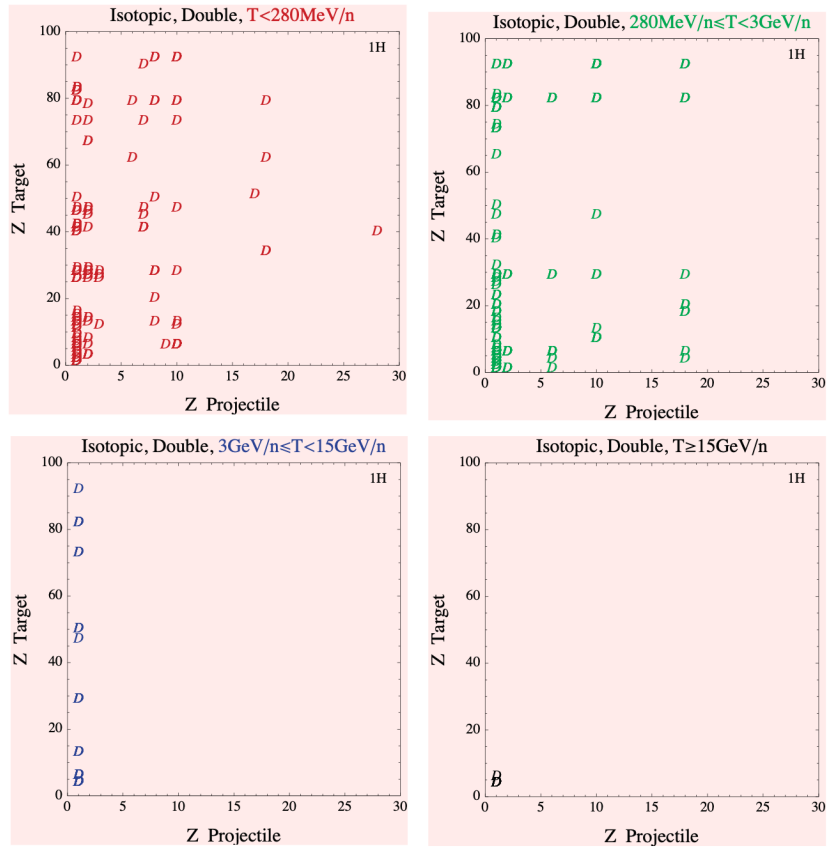


Figure 1.21: Isotopic double differential cross sections for  $^1H$  fragments [23].

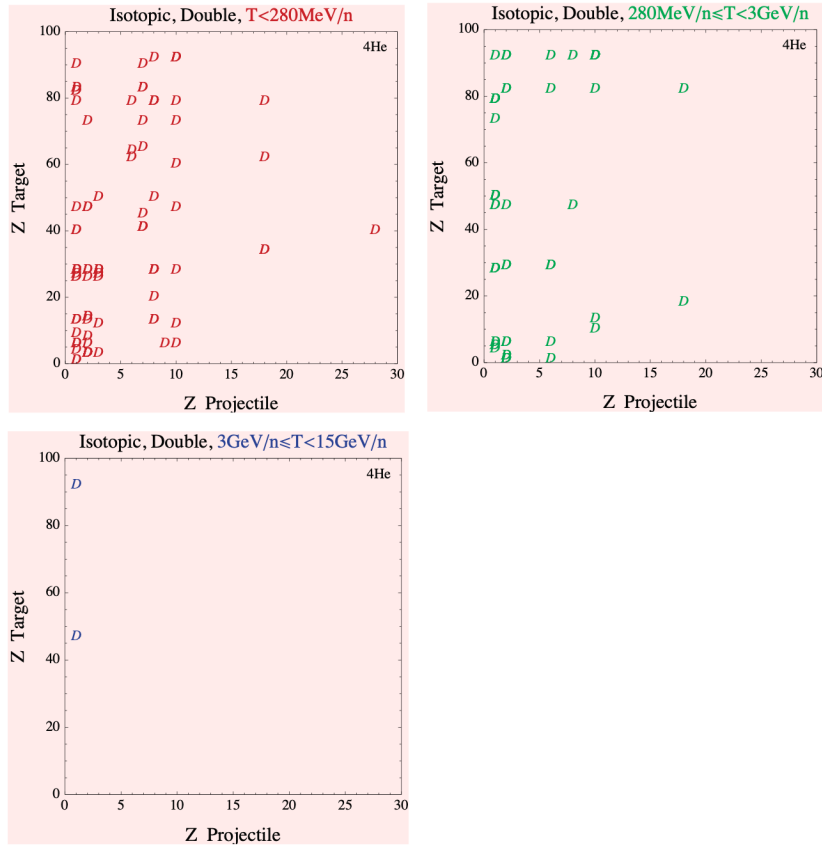
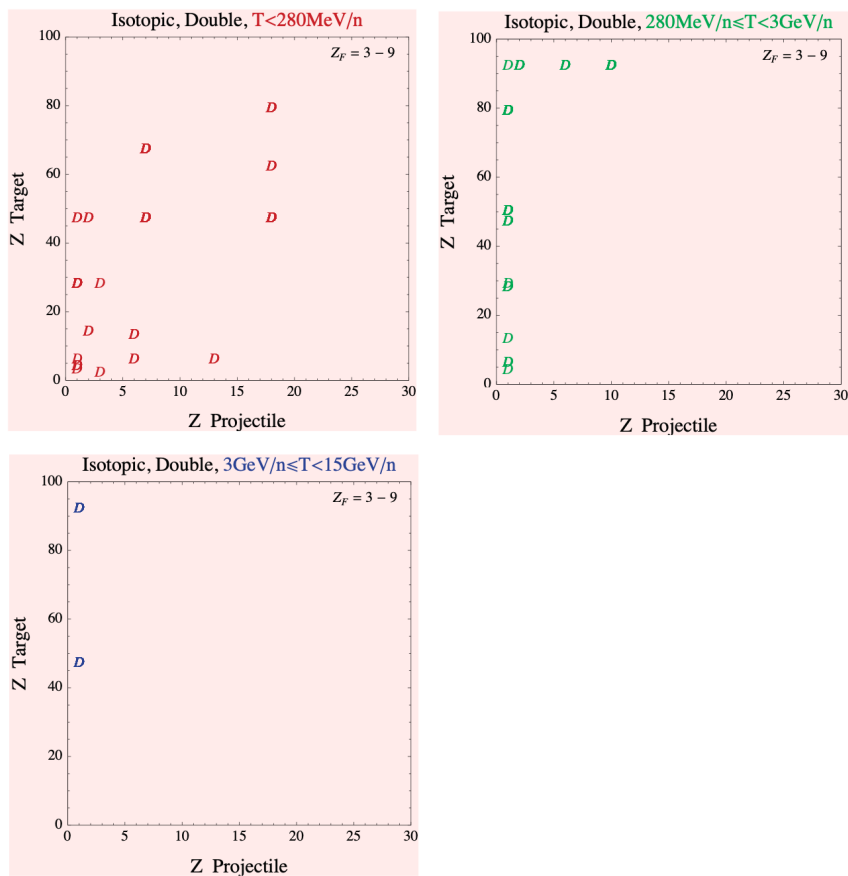
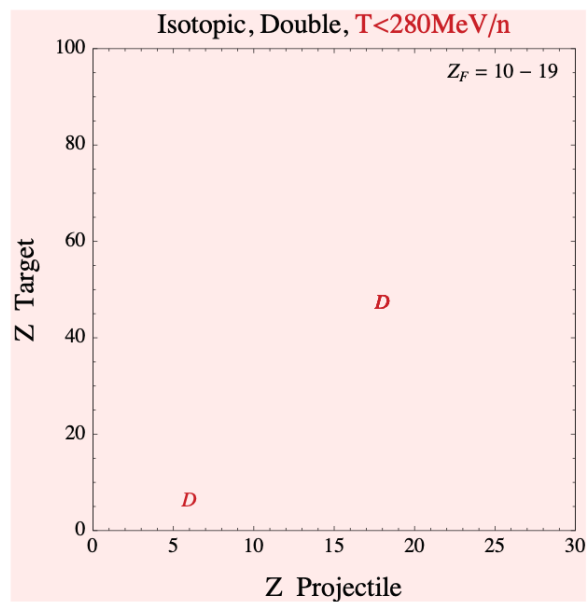


Figure 1.22: Isotopic double differential cross sections for  ${}^4\text{He}$  fragments [23].



**Figure 1.23:** Isotopic double differential cross sections for  $Z = 3 - 9$  fragments. [23].



**Figure 1.24:** Isotopic double differential cross sections for  $Z = 10 - 19$  fragments. [23].



## Chapter 2

# Experimental approaches to fragments detection

In the therapeutic energy range and for the ions of interest (i.e. carbon, helium, oxygen), nuclear fragmentation interactions have not been fully explored so far by experimental measurements, therefore Monte Carlo (MC) simulations are a key tool to predict fragments spectra. However, MC codes have been developed on the basis of incomplete or approximate cross sections data, resulting in a process that feeds on itself. Thus, experiments have been recently performed to characterize fragmentation with a superior accuracy and thus provide data to benchmark the models. Moreover, double differential cross sections for the production of fragments from new ions species of interest in particle therapy (such as oxygen and helium ions [38, 39]) have to be experimentally investigated before their application in the clinics. In particular, nuclear fragmentation process has have to be accurately studied because the biological effectiveness depends on fragment species and energy produced from the interaction of the primary beam with the irradiated target. Accurate measurements of fragments spectra as well as a detailed knowledge of the fragmentation processes are of great importance to estimate the astronauts dose exposure in deep-space missions and for designing proper shielding systems.

As discussed in Sec. 1.1, projectile fragments are generated almost at the same energy of the primary beam, thus travelling a long range and making their detection possible with a relatively simple experimental apparatus, based on energy loss and time of flight measurements. The same experimental setup can be also exploited for the detection of neutrons generated inside targets of interest for space application. Such setup represents the standard system adopted so far for fragmentation studies. The results can be used as a benchmark for the MC models and represent a reference for the evaluation of the impact of nuclear fragmentation on the absorbed dose in treatment planning. In fact, in the Treatment Planning Systems (TPS) the

interaction of the primary beam with tissue is modeled by rescaling data collected in water with a density factor. Anyhow, the different elemental composition of the tissue with respect to water is not accounted. This approximation might limit the TPS accuracy especially if the physical and chemical properties of the transverse material differ significantly from water, as it is case for bone, which is characterized by a relatively high calcium abundance. Therefore, dedicated experimental studies to characterize the interaction of therapeutic beams with tissue-like materials different from water should be performed to improve the effectiveness of treatment plannings.

Since target fragments have a very short range ( $\simeq$  tens of  $\mu\text{m}$ ), they require a more complex experimental setup to be measured and thus a very limited number of data are available. For instance, the standard experimental approach is not a suitable option to measure target fragments. The FOOT experiment, which is presented in details in Sec. 2.2, has been specifically designed to provide not only information about the beam fragmentation, but also an accurate characterization of the fragments generated inside the target material. The planned set of measurements collected by FOOT during dedicated experimental campaigns will fill several of the existing gaps in the nuclear cross sections database allowing for a complete characterization of all fragments, and thus providing isotopic double differential cross sections which are the optimal data for MC benchmarking.

## 2.1 Standard setup

Due to high energy and long range of projectile fragments produced by the nuclear interactions of primary beam with target, the experimental setup optimized for their characterization relies on the detection of ionizing radiation by scintillation light produced in certain materials. The system versatility allows to collect useful data for several targets differing for thickness and material and for beam at both therapeutic and higher energies. Experiments performed with this kind of setup aim at obtaining the following results:

- total yield of all secondary fragments produced by nuclear fragmentation at different target depths (fragments build up);
- angular distributions of the primary beam particles and secondary fragments at different angles;
- kinetic energy spectra of all particle species;

A typical detectors arrangement is shown in Figure 2.1. Once accelerated, the primary beam particles exit the vacuum window, usually made of  $\sim 100 \mu\text{m}$  aluminum, and traverse a thin plastic scintillator (further referred to as *START*)

before impinging on the target. The *START* detector monitors and counts the number of primary particles that will enter the target region. The produced fragments are detected by a  $\Delta E$ - $E$  telescope system consisting of another thin plastic scintillator (further referred to also as *VETO*) coupled with a thick inorganic crystal, such as the Barium Fluoride (further referred to as  $BaF_2$ ) or the LYSO [40]. The *VETO* and the  $BaF_2$  measure the energy release and the total energy of a particle, respectively. The telescope system can be placed at different angles with respect to the primary beam direction (see Figure 2.1) in order to clearly discriminate also lighter and neutral particles or to provide the fragment angular distributions, depending on the experiment goal. The two experimental campaigns presented in Sec. 3 employed a  $BaF_2$  crystal as  $E$  detector and two BC400 scintillators as *START* and *VETO*. The plastic scintillators share the same general structure and detection principles and differ only in active area, thickness and intended use of the output signals. The BC400 material seems an optimal choice, due to its fast rise time ( $\simeq 0.9$  ns), required to obtain precise timing information, and short decay time ( $\simeq 2.4$  ns) for fast single ion counting and low dead time. The organic scintillation material of both *START* and *VETO* detectors is glued to a plastic light guide to maximize the illumination of the photomultiplier. Moreover, the detectors active area, the light guide and the interface to the multiplier are covered with a layer of thin black tape to shield from artificial light sources and to reduce the background noise. The three detectors used during the experimental campaigns analyzed in Sec 3.3 are presented in detail.

The *START* is a 2 mm thick scintillator with an active area of  $10 \times 10$   $cm^2$ . Its two main purposes are to count the number of primary ions impinging on the target and generate timing signals for the Time Of Flight (TOF) measurement. The thickness is chosen as a compromise for maximizing the light output for a variety of particle species and for minimizing the fragmentation of the primary ions inside the detector itself. BC400 represents a good material for this purpose because of its low density ( $\rho = 1.023$   $gcm^{-3}$ ).

The *VETO* is a 9 mm thick scintillator, hexagonally shaped with an inscribed radius of 5.4 cm, thus it covers the complete surface of the  $BaF_2$  detector. Its role is to discriminate between charged and uncharged particles, as well as to separate different ion species by collecting the corresponding energy release. The coupling of the *VETO* and *START* signals provides the trigger to the whole data acquisition, in order to reject the events not generated directly in the target.

The  $BaF_2$  consists of a 14 cm long, hexagonally shaped Barium Fluoride crystal with an inscribed radius of 4.5 cm and directly coupled to a Thorn EMI 9821 QB photomultiplier. Barium Fluoride is an inorganic, dense ( $\rho = 4.88$   $gcm^{-3}$ ) scintillation material with two emission lines, as displayed in Figure 2.2(a): a short

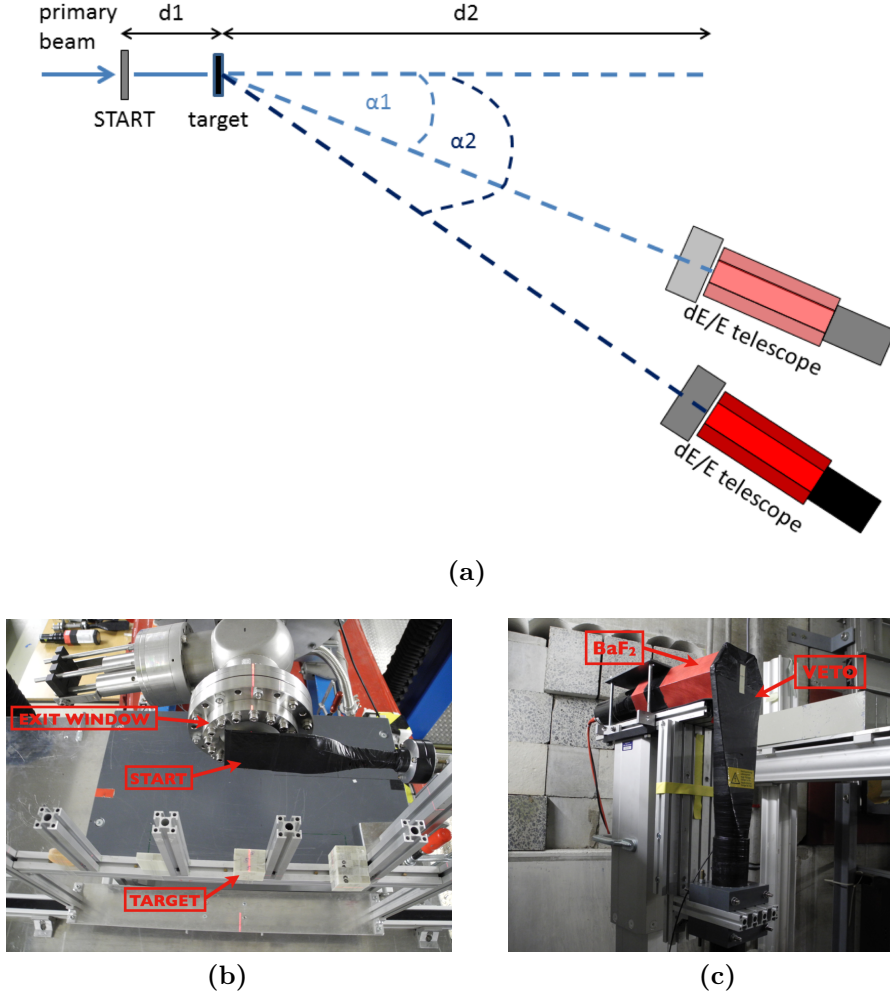


**Figure 2.1:** (a) Scheme of the experimental setup; (b) Photo of the beam exit window, the *START* detector and the targets; (c) Photo of telescope system *VETO-BaF<sub>2</sub>*.  $d_1$  and  $d_2$  indicates the *START*-target distance and the distance between target and the projection of *BaF<sub>2</sub>* position (i.e., center of the beam entrance surface) along the beam line, respectively. Details on the measured angles and target characteristics are reported in Sec. 3.3.

component with a decay time of  $\sim 0.6$  ns and  $\sim 30$  ns length, mainly excited by electrons and photons, and a long component with a decay time of  $\sim 630$  ns and  $\sim 1500$  ns length, mainly excited by charged particles [41]. The signal produced by neutrons behaves in between ions and photons. The short and long component of the *BaF<sub>2</sub>* can be exploited to discriminate incoming photons and neutrons by means of a pulse-shape-analysis [42]. The *BaF<sub>2</sub>* can stop protons up to  $\sim 260$  MeV,

and thus for particles more penetrating it will behave as another VETO element, providing information about energy loss. Neutrons create hadronic showers of light ions (mainly protons) inside the detector material and therefore can be measured [43], making the  $BaF_2$  a valid alternative to organic liquid detectors, usually selected when a mixed type of neutral radiation, such as neutrons and  $\gamma$ -rays, are present. The  $BaF_2$  neutron detection efficiency was evaluated through a dedicated simulation based on GEANT4 code, which calculated the detector response to monoenergetic neutrons with kinetic energies spanning between 10 MeV and 1400 MeV. The  $BaF_2$  neutron detection efficiency  $\epsilon_{BaF_2}$  has been estimated as:

$$\epsilon_{BaF_2}(E_{kin}) = \frac{N_p(E_{kin})}{N_n(E_{kin})} \quad (2.1)$$

where  $N_p$  and  $N_n$  are the number of recoil protons detected by the crystal and the number of incident neutrons, respectively. All the terms are expressed as a function of the incident neutron kinetic energy. Three different kinetic energy threshold values were considered in the simulation, in order to reject the contribution of recoil protons with energies below a certain value. The results are shown in Figure 2.2(b). The energy threshold selected in the analysis of Sec. 3.3.2 was 20 MeV, in order to reject those neutrons not coming from the abrasion phase that should require a dedicated discussion. Independently on the threshold values, two separate behaviours emerge: each neutron detection efficiency curve is characterized by a very fast rise between  $\sim 10$  MeV and  $\sim 200$  MeV followed by slow increase at higher neutron energies. The former is due to elastic scattering resulting in a low neutron energy deposition, while the latter is related to inelastic scattering where a greater amount of energy is released inside the crystal. Moreover, the neutron efficiency decreases as the energy threshold increases, especially below 200 MeV where the amount of recoil protons detected suffer more of the energy threshold imposition. The efficiency correction curve that has to be applied in the off-line analysis of the experimental data is retrieved by fitting the efficiency points retrieved for the simulated energy with the following two separate functions:

$$f(x) = \begin{cases} a_0 + \frac{a_1}{2^{a_2 x}} & x < 200 MeV \\ b_0 + b_1 x + b_2 x^2 + b_3 x^3 & x > 200 MeV \end{cases} \quad (2.2)$$

Due to the sub nanosecond timing response, the high stopping power for charged particles and the good neutron detection efficiency for fast neutrons, the  $BaF_2$  detector is a good choice to perform a secondary particles characterization. The  $BaF_2$  has two main purposes: generating the stop timing signal for the TOF measurement and providing information on the particle residual energy based on the light output.

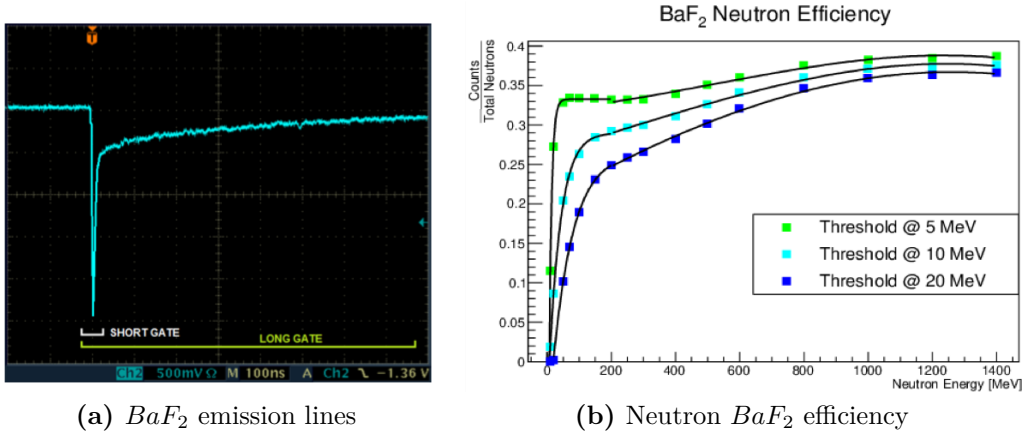


**Figure 2.2:** (a) Typical neutron signal provided by a  $BaF_2$  detector and sent to a Charge to Digital Converter (QDC) (CAEN V792N), where it is integrated over the selected length gates for acquiring the fast and slow decays components. (b) Neutron  $BaF_2$  efficiency evaluated with a GEANT4 simulation. Each point corresponds to the ratio between the number of neutron detected and the number of incident neutron. The black line represents the fit with a sum of an inverse negative power function and a third degree polynomial function.

## 2.2 The FOOT experiment

The FragmentatiOn Of Target (FOOT) project is an applied nuclear physics experiment aiming to measure fragmentation cross sections of relevance for particle therapy and radioprotection in space. The results will be of great help to improve the particle therapy treatment plans quality as well as the design of the spacecraft shielding materials and to benchmark nuclear interaction models. The experiment has been approved and funded by the Italian National Institute for Nuclear Physics (INFN) in 2017 and today it counts more than 90 members in its collaboration. The involved institutions include eleven INFN sections and laboratories, ten Italian universities, three foreign universities and three other research institutions.

The project includes two complementary experimental setups: a setup based on electronic detectors and a magnetic spectrometer to identify fragments heavier than He, and a setup exploiting the emulsion chamber capabilities to detect the light charged fragments ( $Z \leq 4$ ). The construction of the FOOT electronic setup has started in 2018 and will be completed by the end of 2021, in order to take data in the following years. Instead, measurements with the full emulsion chamber setup have been already performed at the research center GSI *Helmholtzzentrum für Schwerionenforschung* (Darmstadt, Germany) in 2019 and 2020 with  $^{16}O$  beam at 200 and 400 MeV/u and with  $^{12}C$  beam at 700 MeV/u impinging on graphite

and polyethylene targets. Most of the detectors of the electronic setup have been built and tested in different calibration campaigns at CNAO (Pavia, Italy), TIFPA (Trento, Italy) and GSI, with different ion beams and different energies.

In this section a comprehensive overview of the FOOT experiment is provided. In Sec. 2.2.1 the strategies conceived to overcome some experimental issues are presented. In Sec. 2.2.2 the design criteria of the experimental apparatus are explained. Finally, in Sec. 2.2.3 and Sec. 2.2.4 the electronic detector setup and the emulsion spectrometer respectively are presented in detail.

### 2.2.1 Experimental strategies

Detecting and identifying all the charged fragments originated from proton-tissue interactions is an exceptionally challenging task because of the very short range of the produced fragments that results in a very low probability of escaping the target. These fragments can travel only few hundreds of  $\mu\text{m}$  at maximum from the emission point, hence even a very thin target ( $\sim\text{mm}$ ) would stop them. At present, a very thin target ( $\sim\mu\text{m}$ ) is almost impossible to mechanically handle without risking to damage it and the interaction probability of the ions beam with the target itself would be too low, requiring an excessively long time to collect a sufficient amount of data. An *inverse kinematics* approach will therefore be pursued, accelerating tissue-like nuclei, such as  $^{16}\text{O}$  or  $^{12}\text{C}$ , into a hydrogen enriched target (further referred to as *laboratory frame*) instead of shooting protons onto tissue-like targets (further referred to as *patient reference frame*). If the kinetic energy is not changed, switching the projectile and target role results only in a reference frame change. In principle, such approach should require a proton target. However, the choice of a pure gaseous hydrogen target has been rejected due to low density and consequent low interaction rate, as well as the impossibility to safely handle it in the therapy and research centers where the experimental campaign will be host. To overcome this issues a carbon ( $C$ ) and an hydrogen enriched compound ( $C_2H_4$ ) targets have been selected. Dealing with an easier to handle target practically translates into a thicker target, which also ensure an increased interaction rate. Once data with  $C_2H_4$  and  $C$  targets have been collected, the cross sections on hydrogen will be retrieved by subtraction as follows:

$$\sigma(H) = \frac{\sigma(C_2H_4) - 2\sigma(C)}{4} \quad (2.3)$$

The same procedure can also be applied to differential cross sections:

$$\frac{d\sigma}{dE}(H) = \frac{\frac{d\sigma}{dE}(C_2H_4) - 2\frac{d\sigma}{dE}(C)}{4} \quad (2.4)$$

$$\frac{d\sigma}{d\Omega}(H) = \frac{\frac{d\sigma}{d\Omega}(C_2H_4) - 2\frac{d\sigma}{d\Omega}(C)}{4} \quad (2.5)$$

This method has been already successfully adopted in a cross sections study involving a  $CH_2$  and  $C$  targets [32], as displayed in Figure 2.3. However, the resulting cross section uncertainties is the quadratic sum of the uncertainties of the two single targets and thus the cross sections on hydrogen are affected by a quite large error.

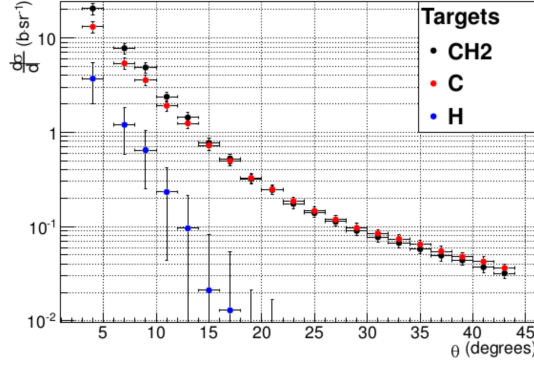


**Figure 2.3:** Combination of the carbon and polyethylene targets angular distribution to obtain the hydrogen angular distribution for  $\alpha$  fragments. The angular distribution on hydrogen has been evaluated with Eq.2.3 [32].

To practically switch coordinates from the *laboratory frame* (further contracted as  $S$ ) to the *patient's reference frame* (further contracted as  $S'$ ) a Lorentz transformation is applied. In the former the proton target is at rest and the ion is moving along  $z$  at a constant velocity  $\beta$  towards the target, while in the latter the ion is at rest and the proton is moving along  $z$  with the same velocity  $\beta$  but in the opposite direction. The 4-momentum of the ion in  $S$  is  $\mathbf{P} = (E/c, p)$  and the 4-momentum of the proton in  $S'$  is  $\mathbf{P}' = (E'/c, p')$ , where  $E$  and  $E'$  are respectively the ion and proton energies. Thus, the 4-momentum components of the proton in the  $S'$  frame can be expressed as:

$$\frac{E'}{c} = \gamma \left( \frac{E}{c} - \beta p_z \right) \quad (2.6)$$

$$p'_x = p_x \quad (2.7)$$

$$p'_y = p_y \quad (2.8)$$

$$p'_z = \gamma \left( -\beta \frac{E}{c} + p_z \right) \quad (2.9)$$

Previous equations can be written in matrix form as:

$$\mathbf{P}' = \Lambda \mathbf{P} \quad (2.10)$$

where  $\Lambda$  is the following 4x4 matrix

$$\begin{pmatrix} E'/c \\ p'_x \\ p'_y \\ p'_z \end{pmatrix} = \begin{pmatrix} \gamma & 0 & 0 & -\beta\gamma \\ 0 & 1 & 0 & 0 \\ 0 & 0 & 1 & 0 \\ -\beta\gamma & 0 & 0 & \gamma \end{pmatrix} \begin{pmatrix} E/c \\ p_x \\ p_y \\ p_z \end{pmatrix} = \begin{pmatrix} \gamma E/c - \beta\gamma p_z \\ p_x \\ p_y \\ -\beta\gamma E/c + p_z \gamma \end{pmatrix} \quad (2.11)$$

Thus, the inverse Lorentz transformation can be expressed as:

$$\mathbf{P} = \Lambda^{-1} \mathbf{P}' \quad (2.12)$$

where the inverse matrix  $\Lambda^{-1}$  is

$$\Lambda^{-1} = \begin{pmatrix} \gamma & 0 & 0 & \beta\gamma \\ 0 & 1 & 0 & 0 \\ 0 & 0 & 1 & 0 \\ \beta\gamma & 0 & 0 & \gamma \end{pmatrix} \quad (2.13)$$

Therefore  $\Lambda^{-1}$  is equal to  $\Lambda$  with a simple change of the  $\beta$  sign as follows:

$$\Lambda^{-1}(\beta) = \Lambda(-\beta) \quad (2.14)$$

In order to correctly apply the Lorentz boost, the inverse kinematics strategy explained requires a resolution on the emission angle of the order of few *mrad*, both in the projectile and fragments directions. A good compromise to have a good interaction rate minimizing the probability of secondary fragmentation within the target should be a target thickness of about 2-4 mm.

### 2.2.2 The design criteria of the FOOT apparatus

A Monte Carlo simulation of 200 MeV/u  $^{16}\text{O}$  beam impinging on a  $\text{C}_2\text{H}_4$  target has been performed using the FLUKA code [44, 10] in order to design and optimize the experimental setup of the FOOT experiment. The fragments production in terms of angular (Figure 2.4 left) and kinetic energy (Figure 2.4 right) has been evaluated. The results show that fragments with  $Z \geq 3$  are forward peaked and mainly confined in a  $10^\circ$  angle with respect to the primary beam direction and their kinetic energy per nucleon is centered around the primary beam value. Instead,

the light fragments are characterized by an extremely broad spectrum in terms both of angular and kinetic energy distribution. This sets the first constraints to be considered on the FOOT detector acceptance. Another fundamental constraint comes from the need to build a compact and "table top" experimental setup, in order to be easily movable and capable to perform measurements in different experimental and treatments room of several European facilities where the beams of interest are available. Due to the large angular aperture of the lighter fragments, the required cost, size and weight of a magnetic spectrometer composed by permanent magnet and high precision tracking detectors able to characterize them would be impracticable in view of a movable setup design. Following these observations, the FOOT setup consists of two alternative complementary setups:

- a setup based on a magnetic spectrometer and several electronic detectors optimized for tracking and identifying fragments with a charge  $Z \geq 4$ , thus covering an angular acceptance up to  $\sim 10$  deg with respect to the primary beam direction
- a setup based on an emulsion chamber spectrometer optimized for the identification of fragments with  $Z \leq 3$ , therefore extending the angular acceptance of the FOOT apparatus up to about 70 deg

The two setups share the upstream region dedicated to the monitoring of the impinging beam.

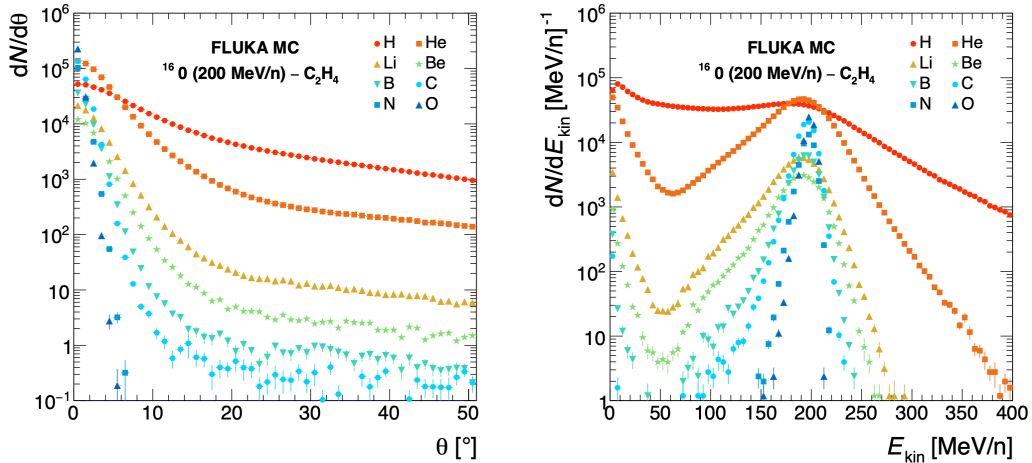


**Figure 2.4:** MC calculation [44, 10] of the angular (a) and kinetic energy (b) distributions of fragments produced by nuclear interaction of a 200 MeV/u  $^{16}\text{O}$  beam impinging on a  $\text{C}_2\text{H}_4$  target.

### 2.2.3 Electronic detector setup

The electronic setup of the FOOT apparatus measures all the needed quantities to precisely identify charge and mass of the heavier fragments ( $Z \geq 3$ ), in order to quantify their production cross section. Specifically, momentum with a resolution  $\sigma(p)/p$  at the level of 3.7%, kinetic energy with a resolution  $\sigma(E_k)/E_k$  at the level of 1.5%, Time Of Flight (TOF) with a resolution at the level of 70 ps are evaluated. The several detectors composing the whole apparatus (Figure 2.5) can be grouped in three different regions:

- Upstream region - A thin plastic scintillator and a drift chamber monitor the primary beam.
- Magnetic spectrometer - Two pixel detectors, a microstrip detector and a permanent magnet system measure the fragments momentum.
- Downstream region - A plastic scintillator and a calorimeter measure the Time Of Flight (TOF) and kinetic energy of the fragments.

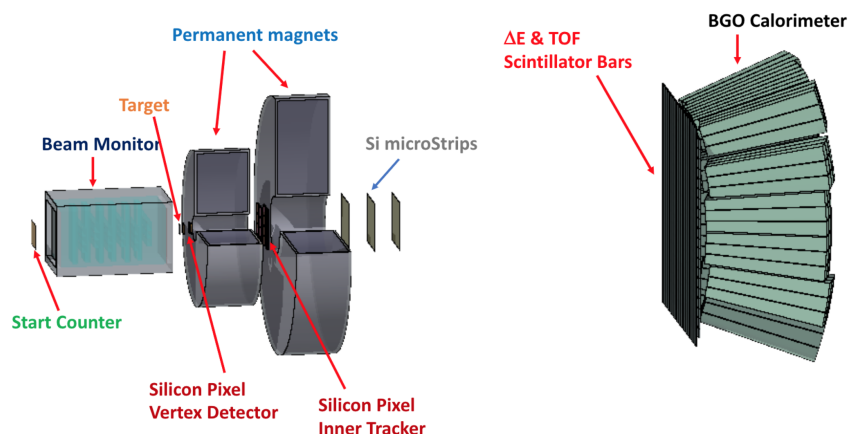


**Figure 2.5:** Schematic view of the FOOT electronic setup (not in scale).

#### Pre-target region

The upstream region is composed of pre-target detectors aiming at monitoring the beam, providing the direction and the interaction point of the beam on the target and counting the number of impinging ions, needed for the cross section measurement.

The **Start Counter (STC)** is placed 44 cm upstream the target and monitors the primary particles rate (with an efficiency  $> 99\%$ ) and provides the trigger signal to the whole experiment, which is combined with the signal of the  $\delta E$ -TOF scintillator detector placed downstream the target to measure the fragments Time Of Flight (TOF). It is a squared 250  $\mu\text{m}$  thick EJ-228 plastic scintillator foil with an active area of  $5 \times 5 \text{ cm}^2$ . The scintillator foil is held by means of an aluminum cage enclosed in a black 3D printed box to provide the light tightness needed for the detector operation (Figure 2.6). The black box has two squared windows, in correspondence of the scintillator, closed with thin (4  $\mu\text{m}$ ) aluminized mylar. 48  $3 \times 3 \text{ mm}^2$  SiPMs (AdvanSiD ASD-NUV3S 1) are in charge to collect laterally the light produced in the scintillator. There are 12 of them on each side, bundled in 8 channels, each reading the series of 6 SiPMs. The WaveDAQ system [45], that handles the readout and powering of the SiPMs, is capable of sampling signals at rates up to 5 Gsamples/s. The collected waveforms are then analyzed offline with a constant fraction discriminator technique to extract the event time  $t_0$ . The WaveDAQ time resolution has been tested with a 700 MeV/u  $^{12}\text{C}$  beam at GSI and found to be of the order of  $\sigma_t \simeq 60 \text{ ps}$ . The STC high performances in terms of efficiency and time resolution can be preserved by using different thicknesses ranging from 250  $\mu\text{m}$  to 1 mm depending on the beam projectiles and energy.

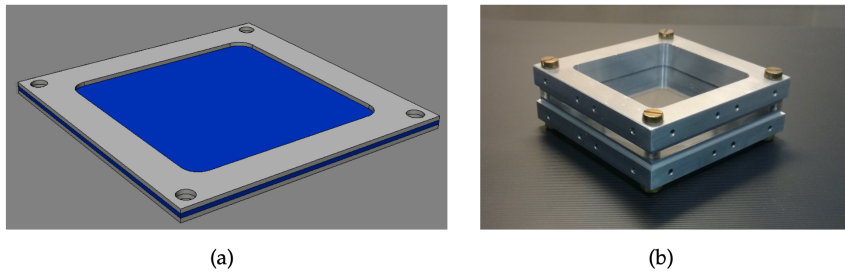


**Figure 2.6:** (a) Technical drawing of the STC and (b) photo of its mechanical frame.

The **Beam Monitor (BM)** is placed after the STC and before the target, in order to measure the direction and impinging point of the ion beam entering the target region. This information is crucial to discard events in which the beam has fragmented in the STC detector producing one or more deviated tracks. In order to discard pile-up vertices a high precision alignment is required between the BM and the devices downstream the target. Moreover, the BM provides also information about the beam spot size, essential to monitor the low intensity beams used for the FOOT acquisitions with the emulsion spectrometer. The BM is a drift chamber consisting of twelve layers of wires, with three drift cells per layer.

Planes with wires oriented along the x and y axes are alternated in such a way to reconstruct the beam profile. The cell shape is rectangular ( $16\text{mm} \times 10\text{mm}$ ) with the long side orthogonal to the beam. The total dimensions are  $11\text{ cm} \times 11\text{ cm} \times 21\text{ cm}$  (Figure 2.7). The BM read-out time, of the order of  $1\ \mu\text{s}$  or less, is fast enough to ensure that tracks belonging to different events are not mixed. The BM operates at  $\simeq 0.9\text{ bar}$  with a  $Ar/CO_2$ , 80/20% gas mixture at a working point ranging between  $1850\text{ V}$  and  $2200\text{ V}$ , depending on the primary beam. An optimal working point of  $\sim 2200\text{ V}$  has been evaluated in recent studies of BM working operations and achievable performances performed in the framework of the FOOT experiment [46] with proton beams. The mean number of hit per event is  $\sim 14$  and the peak of the hit distribution is  $\sim 12$  hits per recorded event in correspondence of the working point. The hit detection efficiency of the BM has been evaluated to be  $\simeq 93\%$  on average. The results show an angular resolution of  $1.62 \pm 0.16\text{ mrad}$  and  $2.1 \pm 0.4\text{ mrad}$  for protons at  $80\text{ MeV}$  and  $228\text{ MeV}$  respectively, while the corresponding spatial resolution at the two beam energies is found to be  $150 \pm 10\ \mu\text{m}$  and  $300 \pm 10\ \mu\text{m}$  in the central part of the cells. The BM high spatial resolution is fundamental to measure the direction of the fragments with an accuracy of few mrad, in order to measure the kinetic energy of the fragments in inverse kinematic.

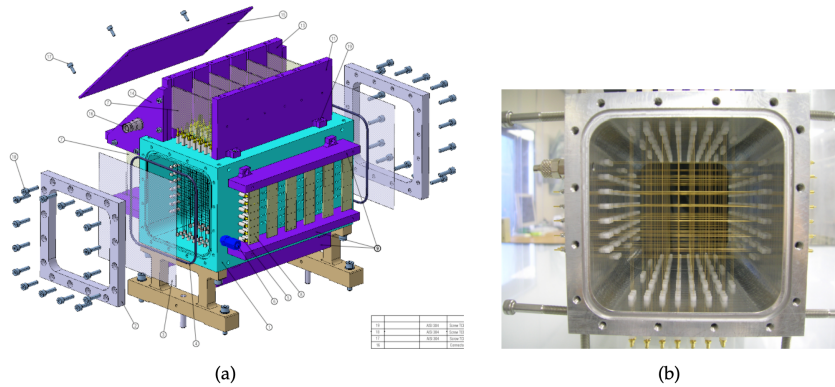


**Figure 2.7:** (a) Technical drawing and (b) photo of the inside of the Beam Monitor.

### Magnetic spectrometer

The magnetic spectrometer includes three stations of pixel and strip detectors allocated upstream, between and downstream of two permanent magnets providing the fragments production vertex and momentum measurement through the tracking in the magnetic field.

The *Vertex detector (VTX)* is composed of four pixel sensor layers, each of  $50\ \mu\text{m}$  thickness in order to minimize the multiple scattering and of  $2 \times 2\ \text{cm}^2$  sensitive, respectively placed along the  $z$  axis at 0.6, 0.9, 2.1, 2.4 cm from the middle of the target. Such arrangement guarantees a geometrical acceptance of about 40 deg. Each layer is equipped with a MIMOSA-28 (M28) Monolithic Active Pixel Sensor (MAPS) (Figure 2.8(a)), which consists of a matrix composed by 928 (rows)  $\times$  960 (columns) pixels of  $20.7\ \mu\text{m}$  pitch, for a total sensitive area of  $20.22\ \text{mm} \times 22.71\ \text{mm}$ . Each sensor is integrated in a dedicated read-out board (Figure 2.8(b)) and includes an amplification and a Correlated Double Sampling (CDS) circuitry. All the pixels CDS output of one row are readout in parallel row by row at the end of the column where 960 discriminators are placed, one per column, each with configurable threshold level. The VTX readout is based on a System on Chip (SoCKit) board housing an Altera FPGA interfaced for the control of the chips. The VTX detector is characterized by a high spatial resolution  $\sigma < 5\ \mu\text{m}$ .

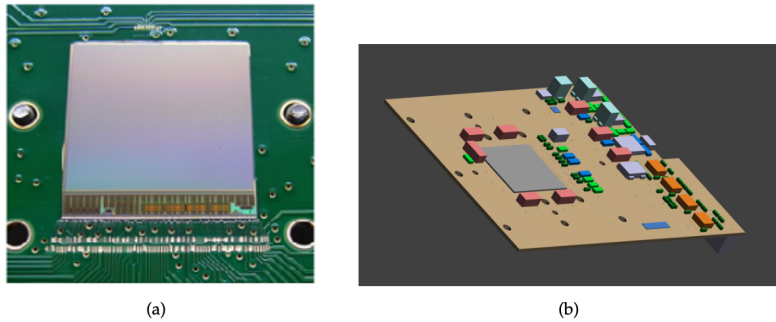


**Figure 2.8:** (a) Picture of a M28 chip. (b) Technical drawing of one of the VTX boards; the gray box in the middle represents the sensor.

The *Permanent Magnet (PM)* is the element in charge to provide the magnetic field to bend the fragments produced in the target. In order to match the requirement of a portable system, limited in weight and size, the choice was a magnetic system in air composed of two magnets in Halbach configuration that ensure a confinement of an approximately bipolar magnetic field in the internal hole of its cylindrical system of permanent magnets. The magnetic field increases with the external cylinder radius while decreases with the gap radius. Two magnets of different dimensions have been selected in order to maintain an angular acceptance of  $\sim 10$  deg for the emitted fragments without losing in resolution on the momentum. Specifically, the first magnet has a gap diameter of 5 cm, while the seconds of 10.6 cm, providing a maximum intensity of 1.4 T and 0.9 T, respectively. The inner tracker placed in-between the two magnets will experience a field of  $\sim 0.6$  T. Each magnet is composed of twelve single pieces of Samarium-Cobalt, selected for its

capability to maintain its features also in a high radiation environment that usually would degrade and damage the magnets' material altering the produced field [47]. A robust external aluminum case will work as safety container and will help in the alignment of the magnets with the tracking stations

The *Inner Tracker (ITR)* will provide tracking of the fragments in the magnetic region. The ITR is composed of two planes of pixel sensors, each one characterized by a sensitive area of  $8 \times 8 \text{ cm}^2$  (Figure 2.9(b) ), each one composed of two ladders similar to the ones implemented in the PLUME project [48] (Figure 2.9(a) ). The layers will be supported by a metallic frame to hold the entire tracker. Each ITR ladder consists of two modules of M28-sensor layers glued on the opposite sides of a support structure made of 2 mm of low density silicon carbide (SiC) foam (Figure 2.9(c) ). An advantage of the M28 sensors is that their tracking performances are not expected to be significantly affected by the residual magnetic field [49].

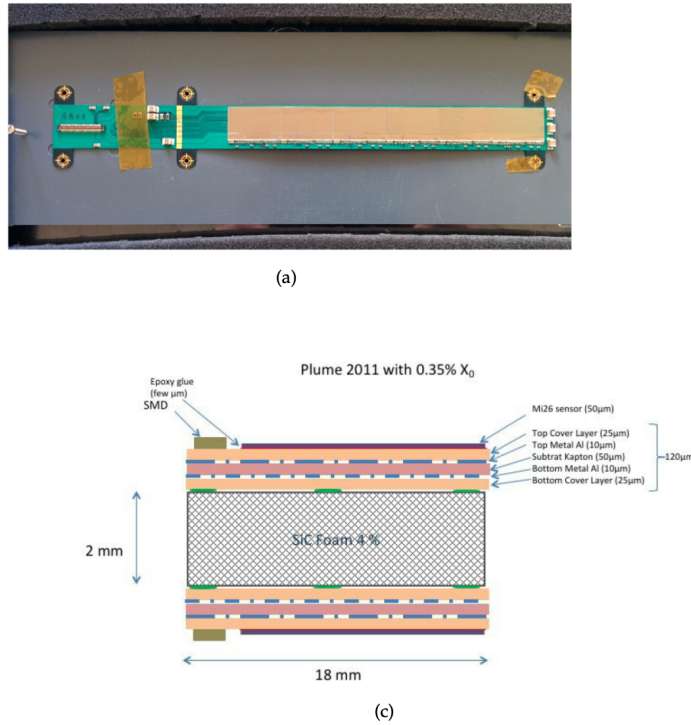


**Figure 2.9:** (a) Picture of a PLUME ladder. (b) Schematic view of the ITR setup. (c) Transversal section of a PLUME ladder.

The *Microstrip Silicon Detector (MSD)* is the final station of the magnetic spectrometer, placed right after the second magnet. The MSD consist of three layers of orthogonally oriented silicon microstrips, each made of two perpendicular

Single-Sided Silicon Detector (SSSD) sensors 150  $\mu\text{m}$  thin glued on a hybrid Printed Circuit Board (PCB) that provides the mechanical support. The layers are separated by a 2 cm gap along the beam direction and the sensitive area covered by the detector is 9.6x9.3  $\text{cm}^2$ . With their 300  $\mu\text{m}$  thickness, each MSD plane can provide an independent  $dE/dx$  measurement. Nevertheless, their thickness could represent an issue in terms of multiple Coulomb scattering and re-fragmentation. A digital readout would provide a spatial resolution of  $\simeq 40 \mu\text{m}$ , but with analog readout a further factor 3 could be easily gained, as shown in [50, 51]. The analog signal amplified by a Low Gain Avalanche Diode mechanism (LGAD) [52, 53, 54] is read by an ADC board.

### Downstream region

It is the distal part of the detector and it is composed of two orthogonal planes of plastic scintillator bars that provide the stop of the TOF and the measurement of the energy loss, together with a BGO calorimeter that provides the fragment kinetic energy measurements. Their distances with respect to the target position will be changed according to the primary beam energy: at 200 MeV/u they will be placed at a distance of about 1 m from the target, while at 700 MeV/u their position will be moved downstream to about 2.9 m. This would permit an improved estimation of the fragments  $\beta = v/c$  thanks to the increased lever arm.

The *Scintillator detector (SCN)* is composed of 40 plastic scintillator bars (EJ-200 by Eljen Technology) arranged orthogonally in two layers. Each bar is 3 mm thick, 2 cm wide and 44 cm long and each layer cover an active area of  $40 \times 40 \text{ cm}^2$ , matching the angular aperture of the heavier fragments. Each bar provides two signal digitized at rates up to 5 Gsamples/s by the same readout of the STC detector, the WaveDAQ system [45]. The SCN provides the measurements of the energy loss  $\Delta E$  and the stop signal for the TOF measurement, as well as the hit position. The formers are of paramount importance for the fragments' charge identification, while the latter can be used as seed for the tracking of the fragments through the bending magnetic field. The bar thickness has been selected as a trade off between the higher scintillation signal and a lower secondary fragmentation probability in the bar itself. The resolution on the TOF and energy measurements are better than 100 ps and 5% for the heavier fragments, respectively. The precision on hit position reconstruction is  $< 8 \text{ mm}$  [55].

The bismuth germanate (BGO) crystals *Calorimeter (CAL)* is the most downstream detector, designed to contribute to the identification of the fragments produced through the measurement of their kinetic energy. Since FOOT will work at a relatively low beam intensity, the ideal material for a calorimeter is a dense

crystal, with high light yield and without strict requirements on the response speed: BGO is a good compromise between performance on one side, mechanical constraints and cost on the other. The high stopping power, guaranteed by the high density of this material ( $\rho = 7.13 \text{ g/cm}^3$ ), coupled to a light yield of  $\sim 10$  photon/keV, meets the requirement of energy resolution  $< 2\%$ . The 320  $\text{Bi}_4\text{Ge}_3\text{O}_{12}$  crystals composing the calorimeter have a truncated pyramid shape with a front (back) face of about  $2 \times 2 \text{ cm}^2$  ( $3 \times 3 \text{ cm}^2$ ) and a length of 24 cm (Figure 2.10(a)). The crystals are positioned with an approximately spherical arrangement ( $\simeq 20 \text{ cm}$  radius) (Figure 2.10(b)) and mechanically divided in modules of  $3 \times 3$  crystals, in order to best handle the weight of the detector. The crystal depth has been chosen in order to minimize the energy leakage especially due to neutrons escaping the calorimeter. Each BGO crystal is coupled to a 25 SiPMs matrix with an active surface of  $2 \times 2 \text{ cm}^2$ . Each SiPM matrix is coupled to a readout board specifically designed to match the dimensions of the SiPMs, ensuring a very compact design of the overall detector. The same board is used also to readout the SiPM temperature sensor, useful to compensate the variation of the system response caused by temperature fluctuations. Several test beams have been performed in a wide energy range (from 70 MeV protons to 400 MeV/u  $^{12}\text{C}$ ), in order to choose the optimal combination of SiPM array, readout configuration and BGO wrappings. The best results were obtained with a Tyvek wrapping.

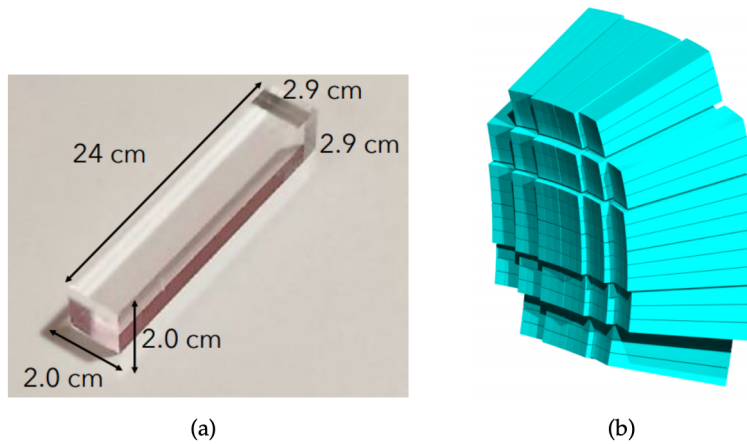


**Figure 2.10:** (a) Picture of a BGO crystal and (b) schematic view of the CAL crystals setup.

## DAQ and trigger

The Data Acquisition (DAQ) system designed for the FOOT electronic setup is designed to acquire the largest sample size with a high accuracy in a controlled and online-monitored environment. To avoid any source of systematic errors due to the trigger selection, the main trigger of the experiment will be a minimum bias trigger based on signals provided by the Start Counter. A fragmentation trigger asking for activity outside the central slabs of the SCN in a logical OR with a prescaled Minimum Bias trigger can also be used to enhance the fraction of recorded fragmentation events. The electronics that will be used to perform the trigger function is a CAEN V2495 board, whose FPGA and internal logic is fully programmable. The maximum acquisition rate in Minimum Bias is dictated by the slowest detectors of the electronic setup, which is the MIMOSA 28 chips in the pixel tracker, with a frame readout time of  $180 \mu\text{s}$ . Therefore the FOOT setup will operate at a maximum rate of about 5 kHz, but in order to reduce the pile-up effects in the MIMOSA chips the actual trigger rate will be of the order of 1 kHz. The DAQ system that will be implemented is a flexible hierarchical distributed system based on Linux PCs, VME crates and boards, detector integrated readout systems and standard communication links like Ethernet, USB and optical fibers. Anyhow, simple information on the DAQ running can be collected from each VME board or data provider at a monitoring rate of the order of seconds, depending on the specific sub-detector system, and provided to a network of PCs connected to the experiment. A further information will come in the form of histograms filled on each PC in the system using local data. Typical histograms will show detector occupancies, particle arrival times, particle energies, collected charges and so on. A third and more powerful online information will come from a fast online event reconstruction performed on the fly on a fraction of events. With a complete reconstruction it will be possible to have, on part of the data, track momentum spectra, TOF, fragment reconstructed charges and masses.

### 2.2.4 Emulsion spectrometer

An *Emulsion Spectrometer (ES)* placed behind the STC and the BM (Figure 2.11 on the left) has been included in the FOOT setup in order to characterize the production of low  $Z$  fragments ( $Z \leq 3$ ), since it extends the angular acceptance up to about  $70^\circ$ . The STC and BM have been used only to perform an on-line control of the beam rate on the active ES surface, to avoid spatial pile-up of events in the ES, and for the monitoring of the beam transverse profile for the absolute flux normalization. The ES will be placed on a remotely controlled table that allows to move the detector in the plane transversal to the incoming beam direction, in order to uniformly distribute the beam on the ES surface. Nuclear emulsion detectors achieve the highest spatial resolution (sub-micrometric) in

tracking ionizing radiation in the three dimensions. The emulsion films employed for FOOT are composed of two 50  $\mu\text{m}$  thick sensitive layers, deposited on both side of a 200  $\mu\text{m}$  plastic base, made of AgBr crystals of 0.2  $\mu\text{m}$  diameter scattered in a gelatine binder. The transversal area is 12 cm x 10 cm. When a ionizing particle passes through a nuclear emulsion film, the trajectory is recorded by all AgBr crystals along its path, producing a latent image. After a chemical process called development, the image is converted into a sequence of silver clusters, or grains, with diameter of 0.6  $\mu\text{m}$ , which can be seen with an optical microscope. After the development, the emulsion is scanned by an automated system. The acquired image is then analyzed by a dedicated software to recognize sequences of dark pixels aligned, which represent the track produced by the penetrating particle. A straight sequence of pixels in one emulsion layer defines a “micro-track”. Two aligned micro-tracks belonging to the top and bottom layers of an emulsion film form a “base-track”. Base-tracks belonging to a straight line along different films, are connected to form “volume-tracks”. Through the propagation of track segments from an emulsion layer to the next, the particle track is reconstructed and the segments fitted. Position and direction can be measured with high accuracy ( $\simeq 0.3 \mu\text{m}$  and 1.2 mrad respectively). The grain density is proportional to the energy loss only over a certain energy range, above which a saturation effect takes place. Emulsion chambers integrate target and detector in a very compact setup and provide a very accurate reconstruction of the interactions occurring inside the target. Moreover, no power supply or any readout electronics is required. Today, recent innovative read-out techniques [56, 57, 58, 59] allow very fast scanning with wide angular acceptances and real time analysis of huge data sets, about one order of magnitude faster than those used in previous experiments [60, 61]. For each data taking with a fixed combination of ion beam, energy and target a different emulsion spectrometer has to be assembled tested and lately scanned and analyzed. The Emulsion Spectrometer for the FOOT experiment has been designed with passive materials alternated to nuclear emulsions films, making three sections with different roles:

- Interaction and vertexing region (Section 1). The first section consists of several elementary cells made of layers of target material, carbon or  $C_2H_4$  (1 mm), alternated with emulsion films (300  $\mu\text{m}$ ) that reconstruct the vertex and position. The length of this section of the spectrometer will be optimized for each different data taking to achieve a statistically significant number of interactions. In GSI 2019 data taking four emulsion spectrometer setups have been tested: for each of the two  $^{16}\text{O}$  beam configurations, at 200 and 400 MeV/u, two different stacks of 30 cells composed of an emulsion film and a target layer of 1 mm of  $^{12}\text{C}$  in one case and of 2 mm of  $C_2H_4$  in the other case have been used. In GSI 2020 data taking with  $^{12}\text{C}$  at 700 MeV/u, two different stacks of 40 cells have been used, one for each of the two aforementioned

targets.

- Charge identification region (Section 2). This section is entirely composed of emulsion films, aiming to reconstruct light fragments charge. The energy loss, and thus the charge, can be retrieved from the grain density, which is observed to be about 30 grains/100  $\mu\text{m}$  for a minimum ionizing particle [62]. The grain density is proportional to the energy loss only over a certain energy range, above which a saturation effect takes place and prevents charge measurements for highly ionizing particles such as carbon ions. To measure their energy loss, after the exposure and before the development, the emulsion films must be kept for an appropriate time (24 h) at a relatively high temperature (above 27° Celsius) and relative humidity (around 95), so to partially or totally erase the tracks. This treatment is called refreshing. The identification of particles with very different energy release can be achieved using the combination of several films, treated with different refreshing procedure after exposure, allowing to overcome the saturation effects of large ionization [62, 63]. Specifically, the refreshing procedure has been optimized for new batches of emulsions used in the FOOT experiment [64]. Section 2 is composed by elementary cells each containing four emulsion films and are dedicated to the low  $Z$  fragments identification. After the radiation exposure and before their chemical development, the emulsion films are treated at different temperature [64]. For each refreshing condition, a track is characterized by three volume variables, which can be combined to identify Hydrogen and Helium nuclei. In GSI 2019 data taking a set of 9 quadruplets of emulsion films refreshed as explained before has been used.
- Tracking region (Section 3). The last section is made of emulsion films (300  $\mu\text{m}$  thick) interleaved with layers of passive absorbers made of high- $Z$  material (Lexan, W and Pb) and is dedicated to the momentum measurements. The section length, the number of passive layers and their thickness will be set according to the incident beam particle and energy. In fact, the accuracy of this method strongly depends on the segmentation of the section in passive layers and on their thickness and material, chosen in order to stop the fragment as in a calorimeter. The lower  $Z$  passive layers are positioned at the beginning of the stack, while the higher  $Z$  layers at the end. By measuring the length of the whole particle track, its kinetic energy can be evaluated on the basis of the correlation between range and momentum. The charged particles momentum can be estimated through the Multiple Coulomb Scattering (MCS) method [65, 66]: by measuring the x-y spatial coordinates and the slope  $(\theta_x, \theta_y)$ , the

particle momentum  $p$  can be evaluated according to the formula:

$$p(\text{MeV}/c) = \frac{13.6}{\beta\delta\theta(\text{mrad})} Z \sqrt{\frac{x}{X_0}} \quad (2.15)$$

where  $\beta$  is the fragment velocity,  $Z$  its charge,  $x$  the traversed distance,  $X_0$  the radiation length in the material and  $\delta\theta$  the deviation of the track slope along its path. The range and MCS methods are two independent procedures to measure energy and momentum, allowing the fragments mass assessment for the isotopic determination.

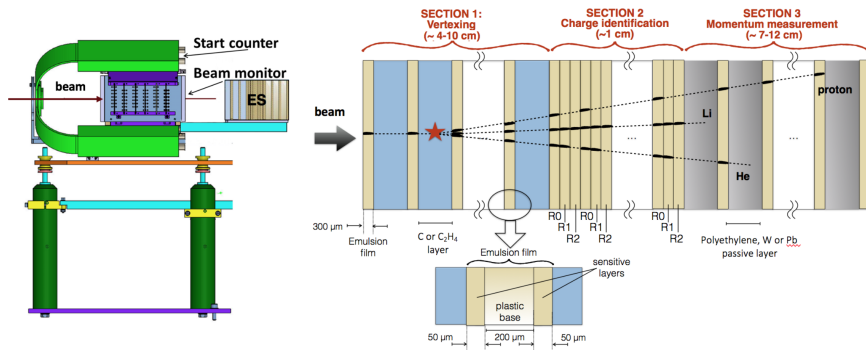


**Figure 2.11:** (Left) Emulsion spectrometer setup placed downstream the Start Counter and the Beam Monitor, with the beam incoming from the left. (Right) Scheme of the emulsion spectrometer composition for the FOOT experiment.



## Chapter 3

# Standard experimental approach to fragments characterization

The technique commonly used to identify particles produced from nuclear reactions between the projectile and target nuclei is based on the fact that different particle species with the same kinetic energy are characterized by a different energy deposition in the same material. Therefore, a telescope system as the one presented in Sec. 2.1 can be exploited for the detection of charged particles and identification of neutrons. The data analysis steps to resolve secondary particles by means of such telescope system are described in details in Secs. 3.1 and 3.2. The discussed methodology is applied to a relevant case for ion therapy in Sec. 3.3.1, providing useful experimental data for the improvement of Treatment Planning when the primary beam interact with a bone region. Moreover, the presented analysis procedure has been exploited in Sec. 3.3.2 to perform a study of secondary neutrons produced in the interaction of a high energy beam with several materials in order to improve space radiation shielding in different mission scenarios.

### 3.1 Particle identification with a $\Delta E - E$ telescope

The typical detectors arrangement presented in Sec. 2.1 is common to a large number of physics experiments aiming to characterize projectile fragments. In the present work, the telescope system is composed of a thin plastic scintillator (here referred to as VETO) and a thick inorganic crystal (in this case a  $\text{BaF}_2$  crystal) selected for both the experiments presented in Secs. 3.3.1 and 3.3.2. A schematic view of the standard apparatus is reported in Figure 3.1. The telescope system

composed of VETO and BaF<sub>2</sub> detectors can be placed at different angles with respect to primary beam direction in order to evaluate the angular distribution of the fragments generated in the target. The detectors characteristics as well the setup have been presented in Sec. 2.1. A particle incident on the telescope loses a small fraction of the energy  $\Delta E$  in the VETO and then, in case of a particle less penetrating than  $\sim 260$  MeV protons, fully stops inside the BaF<sub>2</sub> detector releasing the residual energy  $E$ . For more energetic particles, the BaF<sub>2</sub> detector behaves as another  $\Delta E$  element. The basic principle of the telescope system is the energy loss, ruled by the Bethe-Bloch formula, reported again in the following ( See Eq. 1.1 for details about each terms):

$$S(E) = -\frac{dE}{dx} = \frac{4\pi e^2 Z_t Z_p^2}{m_e v^2} \left[ \ln \frac{2m_e v^2}{\langle I \rangle} - \ln(1 - \beta^2) - \beta^2 - \frac{C}{Z_t} - \frac{\delta}{2} \right] \quad (3.1)$$

According to it, the specific energy loss is strictly related to the charge, mass and energy of the incident particle. Therefore, the quantities  $\Delta E$  and  $E$  are related to the charge and the mass of the particle, which can be identified by the values measured with the two stages of the telescope. The total kinetic energy of the particle impinging on the telescope can be evaluated by coupling the information from the VETO and the BaF<sub>2</sub> detectors. The  $\Delta E$ - $E$  telescope is placed downstream of the target at several angles with respect to the primary beam direction. The time needed to travel the distance between the center of the target, where fragments are assumed to be produced, and the telescope represents the fragment Time of Flight (*TOF*).

Particles identification is performed off-line by means of graphical selections on different two-dimensional scatter plots. Ions of different charge  $Z$  are graphically separated by combining the energy release in the VETO detector (referred to as  $\Delta E$ ) and the one deposited in the BaF<sub>2</sub> detector (referred to as  $E$ ). An example of such two-dimensional plots is shown in Figure 3.3(a), where clusters of particles types can be isolated with a hand-drawn graphical contour as displayed in the figures. Once neutral particles are selected through a graphical cut in the VETO-BaF<sub>2</sub> spectrum as the lower VETO channels corresponding to the pedestals, a further discrimination between neutrons and photons can be provided. Because photons generally produce a very short pulse almost completely included in the BaF<sub>2</sub> short gate, the pulse shape discrimination technique provides a good separation between photons and neutrons. In fact, by plotting the two components of the BaF<sub>2</sub> signal in a 2D plot, the two populations are clearly visible and neutrons can be selected through a hand-made graphical cut (see Figure 3.10). To maximize the discrimination between photons and neutrons, the BaF<sub>2</sub> was operated at a very high voltage (-2100 V). This strategy resulted in a large saturation region visible in the long gate energy spectrum of the BaF<sub>2</sub> at channels higher than  $\sim 370$ .

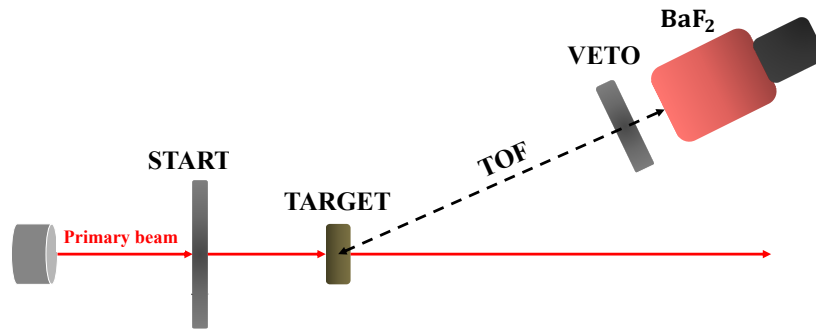
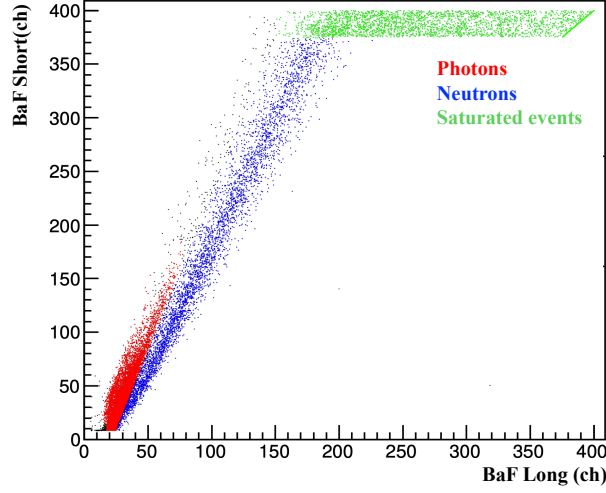


**Figure 3.1:** Scheme of the experimental setup for measuring the yield and kinetic energy of all ion types emerging from the target at different angles.



(a) Polyethylene target

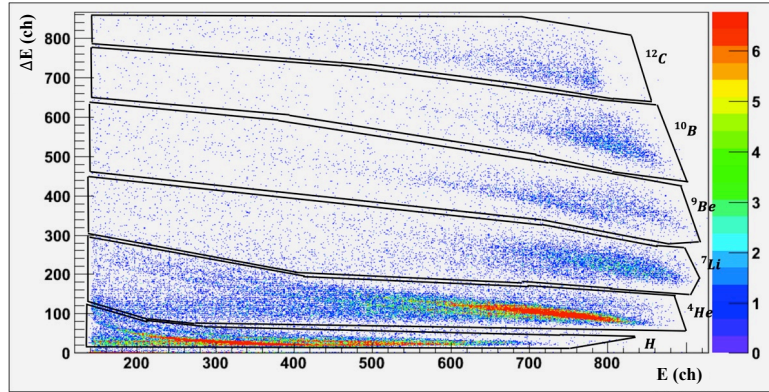
**Figure 3.2:** Example of 2-dimensional plot of the two components (short and long) of the  $\text{BaF}_2$  signal, when the cut on neutral particles is applied. The pulse shape discrimination technique is exploited to identify the population of photons and neutrons in the non saturated region (red and blue dots).

Once each particle species is selected in terms of charge, isotopes can be resolved by applying this first graphical selections to the plot of  $E$  versus TOF, as shown in Figure 3.3(b), and then hand-drawing an additional cut to each isotope population. The most energetic fragments pass through the  $\text{BaF}_2$  detector resulting in escape events on the down-bending right branch below the maximum energy deposition in the spectrum (see Figure 3.3(b)). Once the particle graphical selection is completed, the yield of each fragment type of charge  $Z$  and mass  $A$  is evaluated as the number of events within the graphical cut (referred to as  $\text{count}(Z, A)$ ) normalized by the number of primary particles incident on the target (referred to as  $p_{in}$ ), as follows:

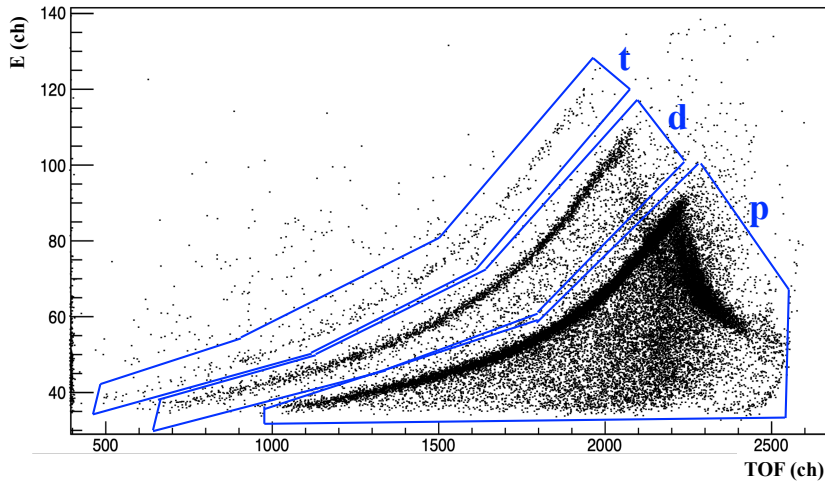
$$\text{yield}(Z) = \frac{\text{count}(Z, A)}{p_{in}} \quad (3.2)$$

Particles exiting the beam line and impinging on the target are counted from the energy spectrum acquired with the START (see Sec. 2.1), whose typical shape is shown in Figure 3.4 (a). The main peak is populated by single primary ions while particles not belonging to the peak are either fragments produced outside of the target or multiple carbon ions hitting the START simultaneously. In order to clean up the distributions and perform a more precise analysis, only events belonging to the primary peak have been selected while the others have been accounted as a normalization factor. Thus, the START main peak was fit with a Gaussian

function (see Figure 3.4 (a)), and only events within  $\pm 3$  standard deviations from the mean value, i.e. those related to a single primary ion, were analyzed. An alternative method to select these events is by selecting with a graphical cut the most populated region in the 2-dimensional plot START-TOF, as depicted in Figure 3.4 (b).



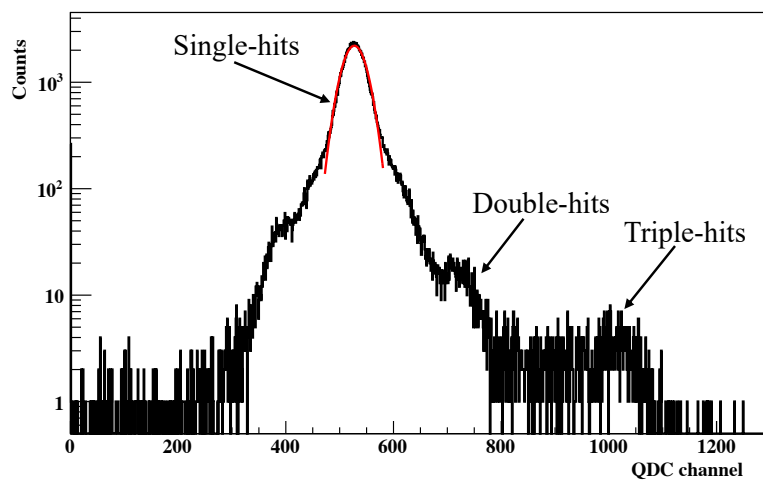
(a)  $\Delta E$ -E 2D plot



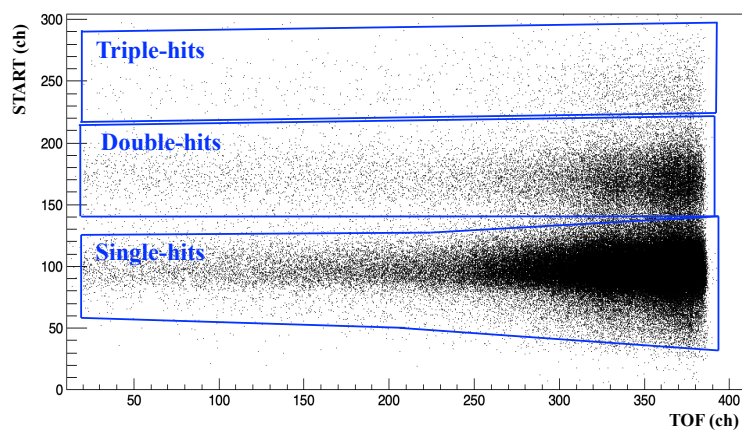
(b) E-TOF 2D plot

**Figure 3.3:** (a)  $\Delta E$ -E plot measured at 4 deg for a 400 MeV/u  $^{12}\text{C}$  impinging on a  $9.095 \text{ gcm}^{-2}$  compact-bone target . The contours are drawn as examples of hand-made selection of each particle species; (b) Correlation between the corresponding E signal and the TOF signal after applying only the graphical selection of hydrogen, in order to visualize its isotopes.

Several corrections are applied to the particle yield of Eq.3.2:



(a)



(b)

**Figure 3.4:** (a) Example of typical energy spectra acquired with the START detector. The peak populated with single primary ions (single hits) is identified and fit with a Gaussian function displayed as a red line. Valid events are selected within 3 standard deviations from the peak mean value. (b) Typical 2-dimensional START-TOF plot. The single-hit region is selected through a hand-made contour of the most populated region.

- *Dead time.* It takes into account the number of events not acquired because of the DAQ limited speed. It can be calculated from the number of trigger events sent to the DAQ (referred to as *free trigger*) and those actually recorded by

it (referred to as *acc trigger*) according to the formula:

$$dt = 1 - \frac{acc\ trigger}{free\ trigger} \quad (3.3)$$

- *Fragmentation outside the target.* It accounts for fragments produced outside the target (e.g. in the detectors). It is calculated by measuring the  $yield(Z)$  without the target and subtracting it from the corresponding value measured with the target.

Furthermore, as the yield is measured at a specific angle value, Eq. 3.2 it has to be normalized by the fraction of solid angle subtended by the telescope system  $\Omega_{BaF_2}$  at that position. After applying all the corrections and normalization, Eq. 3.2 becomes:

$$yield(Z)_{cor} = \left( \frac{count(Z, A)}{p_{in} (1 - dt)\Omega_{BaF_2}} \right)_t - \left( \frac{count(Z, A)}{p_{in} (1 - dt)\Omega_{BaF_2}} \right)_0 \quad (3.4)$$

where the subscripts  $t$  and  $0$  indicate the measurements with and without the target, respectively. The number of recorded events for each measurement run is a compromise between the minimization of the background coming from detector noise and fragmentation processes in the setup (beam line and detectors), and the requirement to acquire enough events to accurately characterize even the reaction channels with the lowest cross section. The error on the particle yields has both a statistical and a systematic contribution. However, the overall uncertainty is dominated by the systematic error, which relates to an incorrect identification of the particles through graphical selection in the 2D  $\Delta E$ -E and E-TOF plots. In order to evaluate its contribution, each fragments population is selected by drawing several contours to include or exclude events of ambiguous nature [67].

## 3.2 Time of Flight technique

Once the charge  $Z$  and atomic mass  $A$  of particles have been identified, the yield and kinetic energy spectra of all particles emerging from the target could be assessed by combining measurements of energy loss in the telescope and the TOF technique [68], which is based on the measurement of the time required by a radiation to travel a given distance through a medium or in vacuum. In this work, the TOF technique is exploited to obtain the kinetic energy spectra of all particles. The TOF measurement is provided by START and BaF<sub>2</sub> detectors acquired through a Time to Digital Converter (TDC). The distance between the two detectors is chosen depending on the energy of the primary ions in order to optimize the time (and then the kinetic energy) resolution and the solid angle covered by the

telescope. However, the raw TOF signal measured by the TDC is provided in channels and it needs to be calibrated first. Assuming that a linear relation links the TDC spectrum channels and the time in  $ns$ , the slope of the line is given by the manufacture and depends on the TDC range selected, while the intercept can be experimentally evaluated by identifying the peak of prompt gammas at any angles. First, a clear selection of all neutral particles can be obtained from the  $\Delta EE$  spectrum, considering that they are characterized by a well-known "punch-through" line, that represents a decreasing energy deposition in the  $BaF_2$  with a zero energy loss in the VETO. Once the selection is applied to the TOF spectrum, the sharp peak of photons can be well distinguished from the broad distribution of neutrons (an example is shown in Figure 3.5(a)). A Gaussian fit is then applied to the photons peak in order to estimate its position (for the time calibration) and its width (for the time resolution). By combining the peak position calculated with the fit and the estimated time needed by the photons to travel from the target center [31], where the interaction point is assumed to be, to the telescope, an evaluation of the intercept value for the calibration line is obtained. Finally, by applying the calibration line to the raw TDC spectrum (see Figure 3.5(a) ), the TOF spectrum calibrated in nanosecond is retrieved, as shown in Figure 3.5(b) as an example. Once the TOF spectrum has been converted to nanosecond, it can be converted into kinetic energy. The total energy  $E$  of a relativistic particle can be expressed as follows:

$$E = \gamma m_0 c^2 \quad (3.5)$$

$$E = m_0 c^2 + E_{kin} \quad (3.6)$$

where  $E_{kin}$  is the particle kinetic energy,  $m_0 c^2$  is its mass at rest and  $\gamma$  is the relativistic Lorentz term, defined as

$$\gamma = \sqrt{1 - \left(\frac{d}{tc}\right)^2} \quad (3.7)$$

By combining Eq. 3.6 and 3.7, the calibrated TOF spectra can be converted into a kinetic energy spectra, as follows:

$$E_{kin} = \left[ \left(1 - \left(\frac{d}{tc}\right)^2\right)^{-1/2} - 1 \right] m_0 c^2 \quad (3.8)$$

where  $d$  is the distance from the target center to the  $BaF_2$  detector. The TOF  $t$  of each particle represent the time required by a fragment to travel from its generation point to the  $BaF_2$ . Thus, the TOF was evaluated by subtracting the

time required by a primary ion to cover the distance between START and target center to the time measured by the acquisition. The flight time of primaries from the START to the mid-target was evaluated by using LISE++ software [69]. This definition assumes that all fragments are produced at the target center, which is valid when the target thickness is much smaller than the TOF distance (as in the present experiments). This method can be applied to all the fragments, charged and neutral, in order to convert the time spectrum in a kinetic energy spectrum. The uncertainty on kinetic energy has been estimated by applying the error propagation rules to Eq. 3.8, thus obtaining the following formula:

$$\frac{\Delta E_{kin}}{E_{kin}} = -\gamma(\gamma + 1) \frac{\Delta t}{t} \quad (3.9)$$

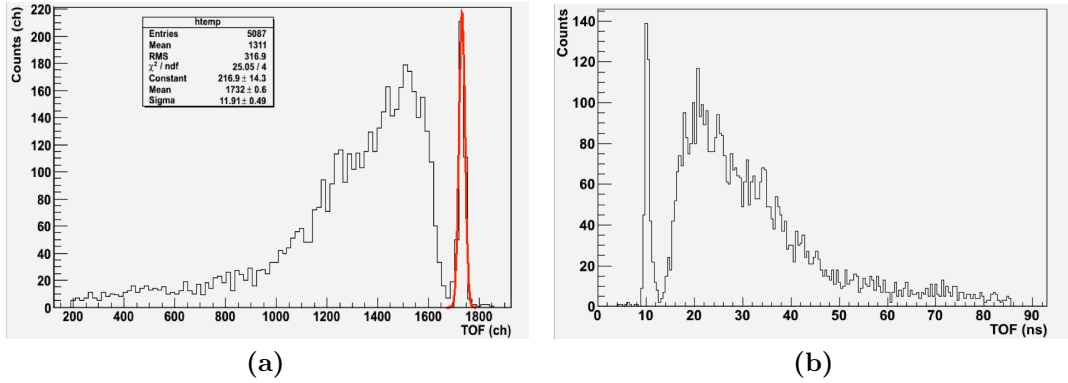


**Figure 3.5:** TOF spectrum of neutral events recorded at 30 deg for a 400 MeV/u  $^{12}\text{C}$  beam interacting with  $9.095 \text{ gcm}^{-2}$  compact bone target. (a) Raw TOF spectrum obtained when only events having a VETO signal below channel 40 are selected. The peak corresponding to gammas is fitted with a Gaussian function displayed in red line. (b) TOF spectrum calibrated in nanoseconds.

### 3.3 Two relevant studies for particle therapy and space radioprotection

The analysis described in details in Sec. 3.1 and Sec. 3.2 is applied in the following to two relevant case studies for particle therapy and space radiation applications, which require specific experimental campaigns to be investigated.

### 3.3.1 Interaction of 400 MeV/u $^{12}\text{C}$ ions with bone-like materials

The interaction of carbon ions with the patient's body is currently modeled in the treatment planning on the basis of experimental data measured in water, while the presence of other biological materials is taken into account by rescaling the values measured in water with a density factor. However, this approximation neglects the influence of the elemental composition, which might become relevant in cases where the material encountered by the beam significantly differs from water and might result in a non uniform and incorrect dose profile. The analysis reported investigate the interaction of a 400 MeV/u  $^{12}\text{C}$  beam with  $9.095\text{ g cm}^2$  (5 cm) thick bone-like materials in order to assess the impact on a treatment plan. Bone is one of the tissues whose elemental composition differs the most from water because of the relatively high calcium abundance. The data were collected in cave A at GSI Helmholtzzentrum für Schwerionenforschung (Darmstadt, Germany) and aim to assess the angular distribution and kinetic energy spectra of secondary particles produced at 0, 2, 4, 6, 7, 10 and 30 deg ( $\pm 0.1$  deg) with respect to the primary beam direction. The mixed radiation field characterized in this study is the results of electromagnetic and nuclear interactions between the  $^{12}\text{C}$  beam and target nuclei. The former cause the ions to slow down as well as to deviate from their initial path due to multiple coulomb scattering; the latter modify the charge and isotope type of the nuclei involved, as well as kinetic energy and direction of the primary beam. The target involved in the analysis is thick enough to have further generations of interactions, namely secondary particles can also undergo both electromagnetic and nuclear reactions, and thus change energy, charge, isotope type and direction. The target material used in this experiment is designed to closely simulate the elemental composition of real bones. The material has a mass number  $A=14.017$  g and a density  $\rho=1.819\text{ gcm}^{-3}$ . The elemental composition is reported in the Tab. 3.1.

Compact Bone - Percentage by weight					
H	C	N	O	Ca	Cl
3.10	31.26	0.99	37.57	27.03	0.05

**Table 3.1:** Elemental composition (percent by weight) of compact bone as specified by the manufacturer Gammex-RMI (Middleton, WI).

The START detector is placed at 16 cm from the beam exit window, the distance between the target center and the START is 17.6 cm and the  $\text{BaF}_2$  is placed at 1.1 cm from the VETO. The  $\Delta\text{E-E}$  telescope is placed downstream of the target and moved to different angles with respect to the primary beam direction up to 30 degrees. The distance between the target and the telescope (referred to as TOF

in Figure 3.1) ranges between 300 and 400 cm depending on the measuring angle. The angular distributions of all produced fragments at different angles has been calculated with Eq. 3.4, after applying a graphical selection of the particle species as explained in Sec. 3.1. The angular distributions provide information on the fragmentation reaction as well as on multiple scattering and absorption processes of the fragments in the target material. Primary ions and heavy particles down to lithium can be detected up to  $\sim 10$  deg, while helium and hydrogen fragments have broader distributions and can still be identified at angles larger than 10 deg. Due to time constraints, the statistics collected in the irradiation time provide a detection limit of  $\sim 10^{-6} msr^{-1} source^{-1}$ . Thus, it is not possible to have a clear separation of the population and thus to characterize the corresponding fragment if the number of particles collected by the  $\Delta E$ -E system is below that value. The angular distributions indicate that protons and helium fragments are the most abundant species generated in the interactions, dominating the spectrum in a narrow forward cone (0 - 5 deg) where their production yield is about three times that of carbon fragments and about one order of magnitude more than all the other fragments. The angular distributions of heavy fragments are well described by a Gaussian or a simple exponential function, while data for light fragments are better reproduced by a superposition of a Gaussian function at small angles and an exponential function at larger ones. Similar conclusions were reported also by [31, 25, 70]. The measured angular distributions together with the corresponding fitting functions are plotted in Figure 3.6(a) for heavy fragments (Li, Be, B and C) and in Figure 3.6(b) for H isotopes (p, d and t) and He particles. The angular distribution width becomes narrower as the fragment charge increases. Deuterons and tritons are characterized by the broadest distribution, but their yield is lower compared to protons and helium particles. The experimentally obtained angular distributions support what is theoretically expected. In fact on one hand, lighter elements are frequently produced by evaporation being emitted isotropically in the centre-of-mass system of the evaporating nuclei. On the other hand, lighter elements suffer more Coulomb scattering, which becomes the most relevant process in generating fragments at large angle. After the particles selection and the calibration of the TOF spectra in time (ns) as explained in Sec. 3.5, the kinetic energy spectra of the primary ions as well as secondary fragments are calculated from the TOF spectra using Eq.3.8. Figure 3.7 reports the kinetic energy spectra of primary beam (Panel (a) ) and secondary heavy fragments (Panel (b), (c), (d) for to boron, beryllium and lithium, respectively) produced. In detail, carbon ions can be detected until 4 deg, boron fragments until 6 deg, beryllium and lithium particles until 7 deg. Figure 3.8 reports the kinetic energy spectra of helium (Panel (a)) and hydrogen fragments measured at three different angles (Panel (b) at 4 deg, Panel (c) at 7 deg, Panel (d) at 30 deg). All the distributions presented in the plots are normalized to the source (i.e. number of primary ions impinging on the target) and to the

solid angle covered by the telescope. At 2 deg, the energy spectra of all secondary charged fragments are characterized by a peak distribution centered at the residual primary beam energy ( $\sim 250 \text{ MeV/u} \pm 10\%$ ), except for hydrogen particles that cannot be separated by others charged fragments in such a narrow cone. The light species detected at large angles (10 and 30 deg) mainly originate from the target atoms de-excitations and from the ablation phase of the nuclear interaction, resulting in energy distributions peaked at much lower values than the primary ions. Increasing the measurement angle, the energy distributions become broader because the detected particles are characterized by a larger particle tracks distribution. In fact, particles involved in central collisions result in a lower kinetic energy when reaching the  $\text{BaF}_2$ , while the ones produced in lateral collision peak around the residual primary beam energy. While the distributions of the heavy fragments down to lithium follow the same trend of primary particles, the distributions of light fragments presents a tail that reaches energies higher than the initial energy of the carbon projectiles. This phenomenon has been already observed [31, 67] and is associated to the Fermi momentum transferred by the nucleus to the fragment [71].

### 3.3.2 Secondary neutrons produced by fragmentation of $^{58}\text{Ni}$ ions in materials relevant for space radioprotection

As discussed in Sec.1.3.2, the health risk associated to extraterrestrial space exploration and colonization deals with isolation, microgravity, and exposure to radiation. Among the risks, radiation is the main showstopper for human space colonization because of the the lack of suitable countermeasures. At present, the only effective countermeasure to space radiation is passive shielding, whose design needs to be constantly improved and optimized. Calculations of the dose equivalent behind aluminum and polyethylene shielding exposed to free space radiation have been performed with analytical (such as the NASA HZETRN code) or MC (GEANT4, FLUKA, PHITS) codes. All models predict a local minimum around  $20 \text{ gcm}^{-2}$  in aluminum, while no pile-up is seen in polyethylene, as displayed in Figure 3.9 [72]. Additional calculations pointed out that  $\sim 50\%$  of the dose equivalent between  $45\text{--}100 \text{ gcm}^{-2}$  of aluminum comes from secondary protons produced through neutron-hydrogen elastic collisions [72]. Thus, neutrons can increase the dose equivalent behind the shield. This effect is not observed when light shielding materials are used, yet all codes predict saturation for high thickness, suggesting that there will be no gain in heavier shelters.

The contribution of neutrons to the total dose is highly dependent on the shielding thickness and material. With light, metal shielding ( $5\text{--}30 \text{ gcm}^{-2}$  aluminum) contained in the spacecraft structure, the neutrons dose rates above 400 km

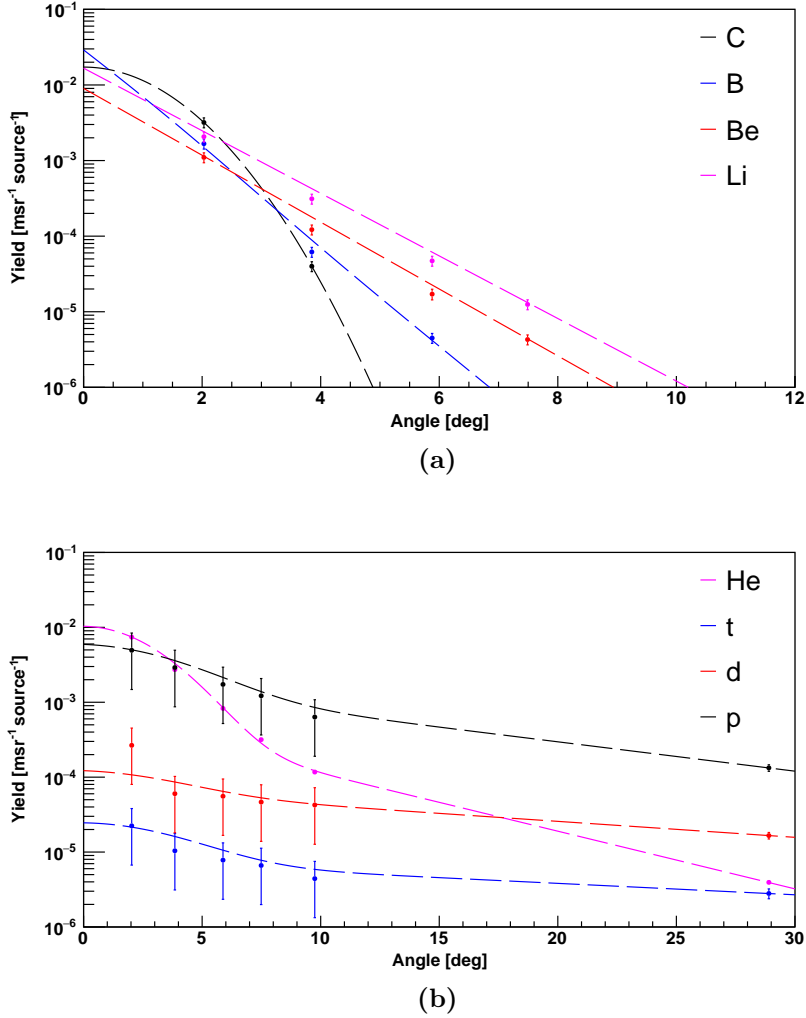


**Figure 3.6:** Angular distributions of secondary (a) heavy (C, B, Be, Li) fragments and (b) light (He, <sup>3</sup>H, <sup>2</sup>H, <sup>1</sup>H) fragments produced at forward angles from 0 to 30 deg by the interaction of 400 MeV/u <sup>12</sup>C beam with 9.095 gcm<sup>-2</sup> (5 cm) compact bone target. Particle yields have been calculated with Eq. 3.4. The results are normalized to the source (i.e. number of primary ions impinging on the target) and to the solid angle covered by the telescope. The dashed lines represent the fitting curves obtained from a combination of a Gaussian and an exponential function.

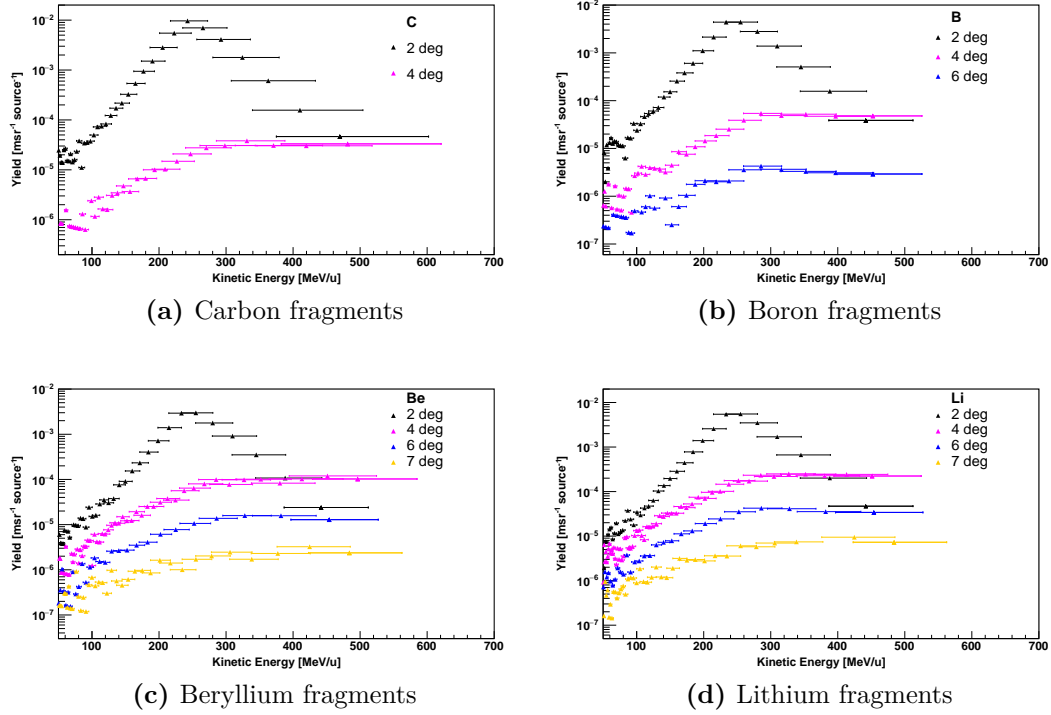


**Figure 3.7:** Kinetic energy spectra of the primary beam ((a) carbon) and secondary heavy fragments ((b) boron, (c) beryllium and (d) lithium) produced by a 400 MeV/u  $^{12}\text{C}$  beam interacting with  $9.095\text{ gcm}^{-2}$  (5 cm) compact bone target and obtained with Eq. 3.8. The yield is normalized to the source (i.e. number of primary ions impinging on the target) and to the solid angle covered by the telescope.

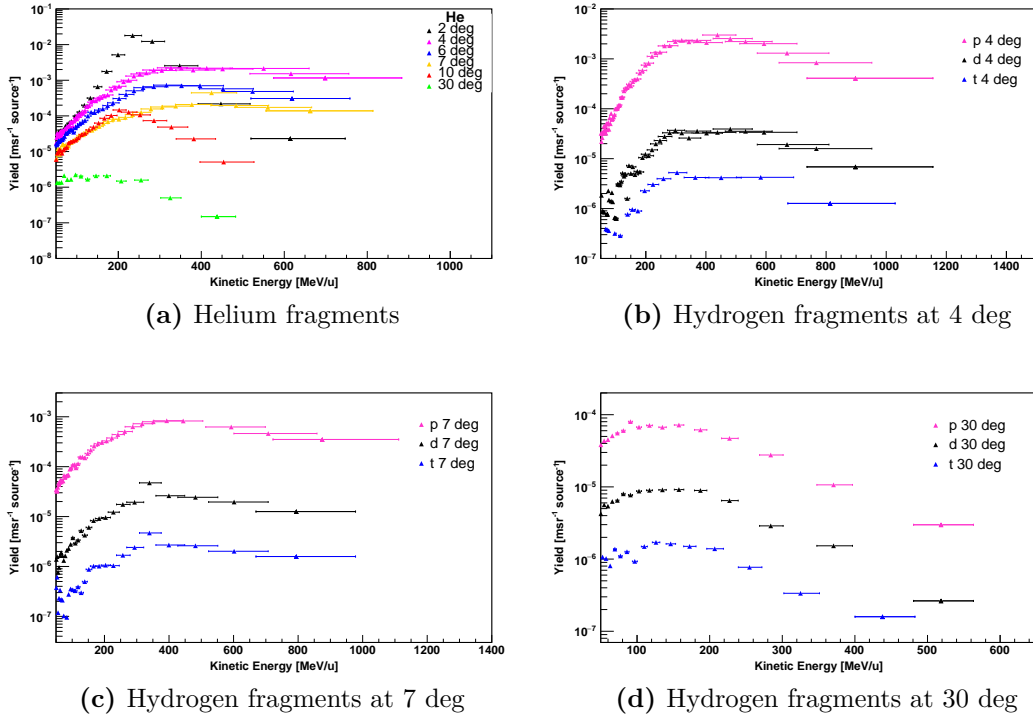


**Figure 3.8:** Kinetic energy spectra of helium fragments and hydrogen fragments (protons, deuterons and tritons) produced by a 400 MeV/u  $^{12}\text{C}$  ions beam interacting with  $9.095 \text{ gcm}^{-2}$  (5 cm) compact bone target. The distributions were calculated with Eq. 3.8. Helium fragments have been detected up to 30 deg with respect to the primary beam direction. Instead, only three reference detection angle have been displayed for hydrogen fragments (4, 7 and 30 deg).

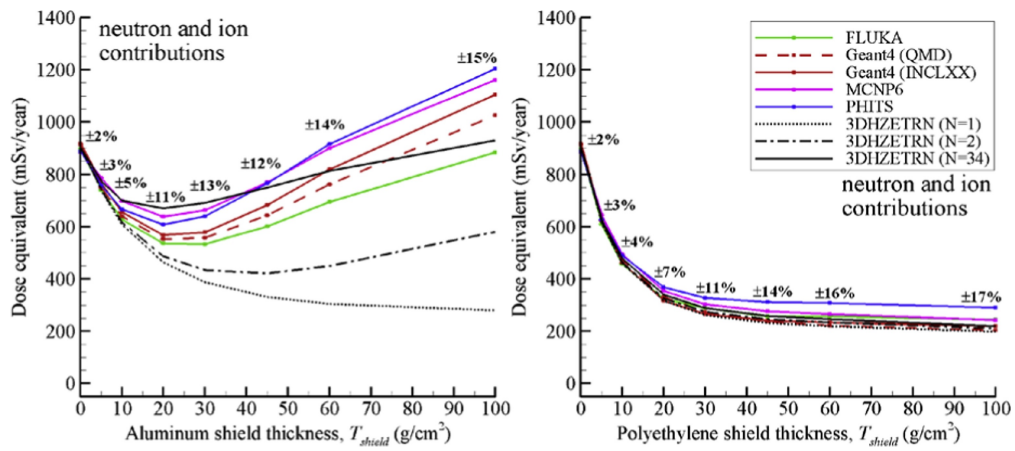


**Figure 3.9:** Total dose equivalent including neutrons and light ions from GCR as a function of the thickness of aluminum (left) and polyethylene (right). Results from different analytical and MC codes (FLUKA, GEANT4, PHITS, HZETRN) are compared. The predictions have some substantial differences, due to the different physics models used and to the lack of reliable cross-sections for the fragmentation of several ions at high energy [22].

altitude were around 0.025 mGy/day, to be compared to 0.46 mGy/day or 0.86 mGy/day from charged particles [73]. The situation does not change on a planet surface: on Mars, the albedo neutrons produced in the top layer of the soil are abundant and they will dominate the exposure. Therefore, for deep planetary bases, the neutrons contribution in dose equivalent can increase up to 90% or more. However, the production of fast neutrons seems to be underestimated by the codes, according to the recent measurements of the Mars Science Laboratory (MSL) both during the transit to Mars and on the planetary surface. Specifically, an excess of neutrons in the 100-1000 MeV has been detected [74, 75]. Most of our knowledge is actually limited to fission-spectrum neutrons, where several experiments have proven their high biological effectiveness, while at high energy very few data are available, and the uncertainties are very high. On the basis of the above discussion, it is clear that the production of fast neutrons is a large contributor to the uncertainties on space radiation risk for both thick shield configurations and planetary missions. Accelerator-based measurements are in those cases an essential tool to characterize the shield and several experiments have been performed to test the relative effectiveness of different materials [76]. The ROSSINI (RadiatiOn Shielding by ISRU and/or INnovative materIals for EVA, Vehicle and Habitat) project, specifically devoted to neutrons characterization in materials relevant of space radiation protection, was then conceived. The aim of the ROSSINI project financed by the European Space Agency (ESA) is to select innovative shielding materials and provide recommendations on space radioprotection for different mission scenarios. The results of these analysis will be of great help to identify suitable shielding materials which could be better than the current adopted standard solution (i.e., polyethylene). The data were collected in cave A at GSI Helmholtzzentrum für Schwerionenforschung (Darmstadt, Germany). The telescope system composed of the VETO and BaF<sub>2</sub> detectors was placed at ~24 deg with respect to the primary beam direction. Along the beam axis, the particle yield is dominated by residual primary ions and heavy fragments. Their abundance, combined with the lower efficiency for detecting neutrons, limit the accuracy in measuring neutral particles in the two-dimensional  $\Delta E$ -E plot. The choice of the 24 deg angle is to maximize the detection of neutrons produced in the abrasion phase (see Sec. 1.1.4) without losing accuracy in the energy spectrum, which is almost the same between 0 and 30 deg [77]. The analysis presented here is for a 1000 MeV/u <sup>58</sup>Ni primary beam impinging on several targets currently used in space or considered as promising candidates for in situ missions. Materials, densities and thicknesses are listed in the Tab. 3.2. In particular, Moon concrete and regolith and Mars regolith are complex materials, whose elemental composition as reported by the manufacturer is reported Tab. 3.3, 3.4, 3.5. The Moon concrete target is directly cut from a solid block of material, while Moon and Mars regolith are composed of a powder placed in boxes of Laminil which define the shape and size

of the target. While distance between VETO and BaF<sub>2</sub> is fixed at  $\sim 1$  cm, the distance between the START and the target center, as well as between the target and the BaF<sub>2</sub>, varies depending on the target type. The values for each datasets are also reported in Tab. 3.2.

Material	Thickness [gcm <sup>-2</sup> ]	D <sub>START-Target</sub> [cm]	D <sub>Target-BaF<sub>2</sub></sub> [cm]
Aluminum $\rho = 2.7$ g/cm <sup>3</sup>	2.03	2.3	340.3
	4.73	3.3	335.3
	10.13	3.8	335.0
	13.50	4.4	337.0
	18.23	5.3	335.0
	31.05	24.7	324.0
Polyethylene $\rho = 0.93$ g/cm <sup>3</sup>	1.50	2.7	339.0
	5.13	5.2	337.0
	7.07	5.7	334.0
	20.74	13.1	320.0
	24.46	15.1	316.5
	29.91	20.8	334.0
Mars Regolith $\rho = 0.93$ g/cm <sup>3</sup>	5.39	5.3	336.7
	10.60	7.6	329.0
	19.44	12.4	329.6
	24.95	16.6	322.5
Moon Regolith $\rho = 1.76$ g/cm <sup>3</sup>	4.72	3.7	338.6
	9.86	4.7	335.0
	22.18	8.2	333.8
	29.92	10.9	330.5
Moon Concrete $\rho = 1.64$ g/cm <sup>3</sup>	5.36	4.0	337.8
	10.99	5.3	335.0

**Table 3.2:** Materials, density and thickness of the targets used in the framework of the ROSSINI experiment. D<sub>START-Target</sub> and D<sub>Target-BaF<sub>2</sub></sub> represent the distance between the START detector and the center of the target and the distance between the latter and the BaF<sub>2</sub> detector, respectively.

Moon Concrete - Percentage by weight										
O	Si	Fe	Ca	Al	Mg	K	Na	Ti	Mn	P
42.83	19.82	10.33	9.33	8.58	3.87	2.13	2.00	0.79	0.17	0.15

**Table 3.3:** Elemental composition (percent by weight) of Moon concrete as specified by the manufacturer.

Moon Regolith - Percentage by weight											
O	Si	Fe	Ca	Al	Mg	Na	Ti	K	P	Mn	Cr
42.72	19.36	12.79	9.53	8.50	2.88	1.87	0.97	0.88	0.28	0.19	0.02

**Table 3.4:** Elemental composition (percent by weight) of Moon regolith as specified by the manufacturer.

Mars Regolith - Percentage by weight										
O	Si	Al	Fe	Ca	Ti	Mg	Na	K	P	Mn
44.48	20.19	12.44	11.11	4.19	2.40	2.11	1.85	0.50	0.39	0.23

**Table 3.5:** Elemental composition (percent by weight) of Mars regolith as specified by the manufacturer.

The analysis procedures presented in Sec. 3.1 and 3.2 can be applied also for the characterization of secondary neutrons. Once neutrons have been identified, their kinetic energy spectra can be evaluated from the calibrated TOF spectrum as reported in Eq.3.8. Finally, the efficiency curve (see Eq. 2.2) is applied to correct the neutron spectrum for the BaF<sub>2</sub> detection efficiency as a function of the kinetic energy.

Figures 3.10(a, b, c, d, e) illustrate the kinetic energy spectra of secondary neutrons produced in several thicknesses of polyethylene, aluminum, Mars regolith, Moon regolith and concrete, respectively.

All energy spectra are peaked between  $\sim 300$  and  $500$  MeV independently of the target material and thickness. In the range of thicknesses considered in the experiment (between  $\sim 1.5$   $gcm^{-2}$  and  $\sim 31$   $gcm^{-2}$ ), the number of neutrons produced increases with the target thickness regardless of the irradiated material. Furthermore, for aluminum, Moon and Mars regolith the peak shifts towards lower energies at increasing target thickness while this behaviour is not clearly evident for polyethylene and Moon concrete. The neutron yield as a function of the target is called build-up curve and can be obtained by integrating the kinetic energy distributions. The results for all materials are shown in Figure 3.11. Several considerations can be made on the basis of the kinetic energy spectra and build-up curves: polyethylene, which currently represents the reference shielding material, seems the best choice with respect to aluminum in terms of neutrons production; Moon regolith provides a lower neutrons production with respect to Moon concrete, at least up to the tested thickness of  $\sim 10$   $gcm^{-2}$ ; in the thickness range analyzed, Mars regolith always represents the best material choice. However, the point corresponding to the thickest aluminum target requires an additional investigation, in order to understand if it is due to a peculiar behaviour of the material once a certain thickness is reached or is only related to analysis issues.

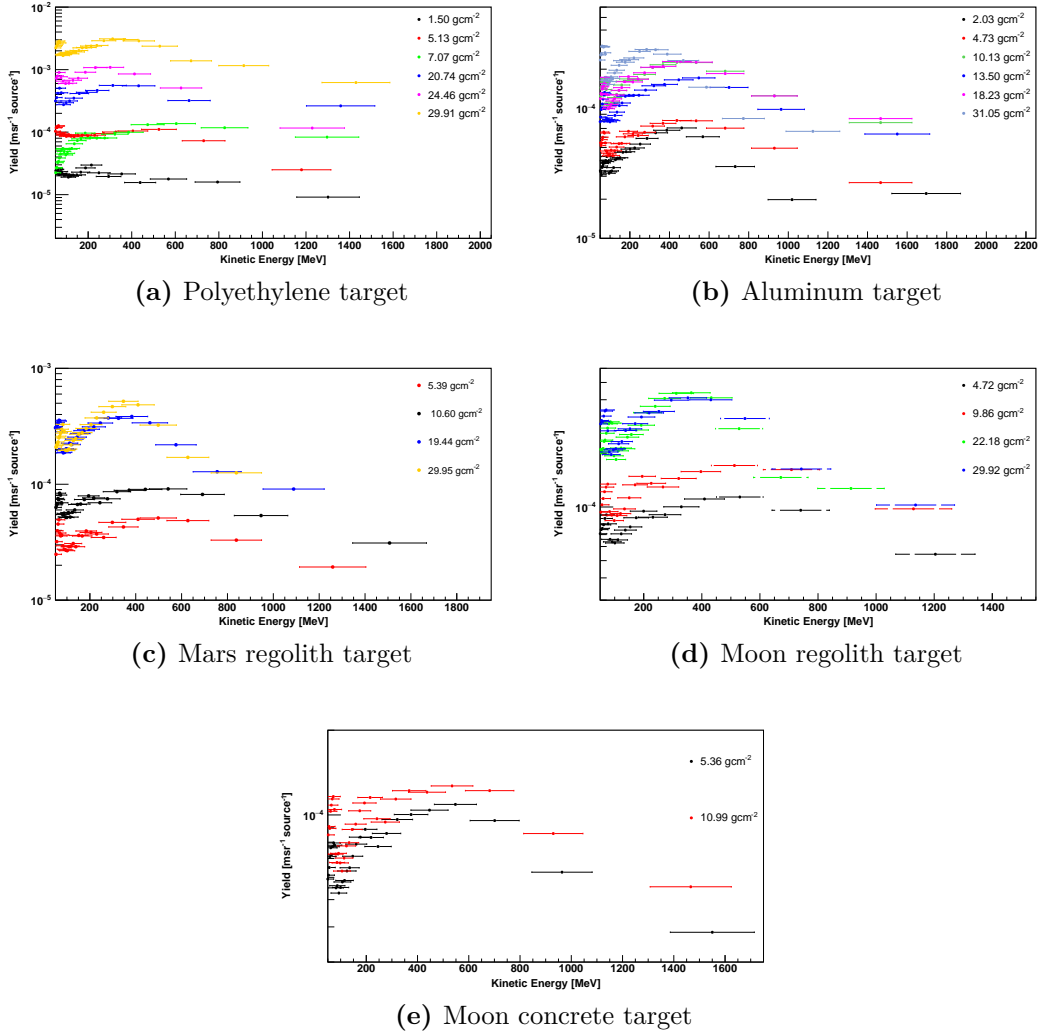


**Figure 3.10:** Kinetic energy spectra of secondary neutrons produced in the interaction of a 1000 MeV/u  $^{58}\text{Ni}$  beam with targets of (a) polyethylene, (b) aluminum, (c) Mars regolith, (d) Moon regolith, (e) Moon concrete. The target thickness is specified on each plot. The distributions have been calculated with Eq. 3.8. Neutron yields have been corrected with the  $\text{BaF}_2$  efficiency curve reported in Eq. 2.1 .

The results of the reported analysis can be compared with data presented in [78], where targets were irradiated with a 968 MeV/u and 972 MeV/u  $^{56}\text{Fe}$  ions beam. The measurements in [78] refer to a different experimental campaign also performed in the framework of the ROSSINI project, thus the irradiated targets are of the same type as those included in this work (see Tab.3.2). While for aluminum, the normalized dose reduction is almost constant independently of the thickness, for polyethylene there is a rapid build-up in the first 2  $\text{gcm}^{-2}$ , followed by a slow drop at larger thickness. Furthermore, polyethylene reduces the dose between  $\sim 15\%$  and  $\sim 50\%$  more than aluminum for any target thickness considered. For Moon and Mars regolith and Moon concrete, the dose reduction is almost the same at any target thickness analyzed and ranges between  $\sim 2\%$  and  $\sim 3\%$ . In conclusion, polyethylene is confirmed to be the best compromise between low neutrons production and dose reduction capability, resulting in the ideal material for the spacecraft hull shielding. Regarding the possibility to exploit in-situ resources, Moon concrete seems to provide always a lower dose reduction with respect to Moon regolith. However, additional target materials and thicknesses should be irradiated with  $^{58}\text{Ni}$  and other light and heavy ions in order to provide a more complete comparison of candidate shielding materials in terms of neutrons production. The GCR simulator present at the NASA laboratory [79] could provide the best radiation source to perform the most realistic analysis. The results reported here are a preliminary study and the analysis is still ongoing. In particular, a dedicated Fluka MC simulation to assess the influence of the irradiation room geometry is being developed in order to account for background neutrons produced in the surrounding walls and setup elements.

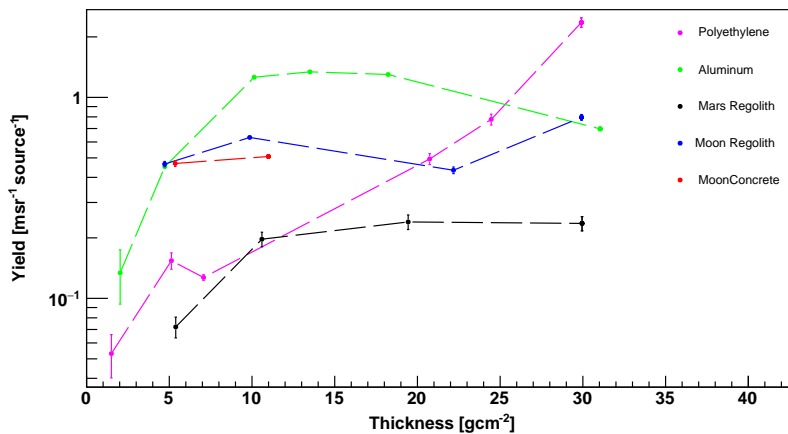


**Figure 3.11:** Neutron yield build-up curves. Each value is obtained by integrating the differential neutron yield spectrum of Figure 3.10 over the entire kinetic energy range. Error bars include both statistic and systematic uncertainties.



# Chapter 4

## Global analysis of the FOOT experiment

At present, the study of fragment reconstruction capability of the FOOT experiment relies on Monte Carlo simulations produced by means of the FLUKA code and a little sample of real data acquired at the GSI laboratory. In this chapter, an extended investigation of the electronic setup performances and fragments reconstruction capabilities is discussed for the only simulated data.

In Sec. 4.1 and 4.2 an overview of the FOOT reconstruction software and the MC simulations at the base of the analysis presented in this work is reported.

Sec. 4.3 present the procedures, as well as their physical basis, adopted to identify each generated fragment in terms of charge and mass.

In Sec. 4.4 the proceeding for the cross sections reconstruction is explained.

Finally, in 4.5 the sensitivity of FOOT performances with respect to the resolution on time of flight, momentum and kinetic energy is investigated.

### 4.1 The analysis software

SHOE (Software for Hadrontherapy Optimization Experiment) is a ROOT based framework for the FOOT reconstruction software. SHOE is able to perform the full reconstruction of the events provided both by experimental campaign in the DAQ raw format (digitized signals) and by the FLUKA [44, 10] simulations in the ROOT ntuple format. Both formats are read and converted in a single software-object by SHOE, in order to use the same reconstruction chain. The SHOE software is composed by a Simulation code and a Reconstruction code, and is organized in:

- *G4Simulation folder* contains everything is needed to run the simulation with Geant4 [80].

- *Simulation folder* contains everything is needed to run the simulation with FLUKA.
- *libs folder* contains the framework and all the classes needed to handle the reconstruction of the many FOOT subdetectors and the event display.
- *Reconstruction folder* contains the executables and macros to run the events reconstruction.

Specifically, the global analysis of FOOT is managed by the Reconstruction folder and the event reconstruction is divided in two parts:

- *Level0* - It is in charge of the interpretation of both experimental and Monte Carlo data, applying the required detectors calibration constants, resolutions and efficiencies in order to produce hit, cluster and track objects. The track reconstruction in magnetic field is based on a Kalman filter algorithm, which is a technique of common use to estimate the state of a system affected by some kind of noise, by combining the output of different sensors. Specifically, a state vector describes the state of an ion track at any surface of one or more detectors. The Kalman filter is based on the succession of alternating phases: the prediction step, where the current state vector is extrapolated to the following detector surface or sensor, and the predicted noise due to multiple scattering and the energy loss are taken into account; the filter step, where the predicted state vector is corrected by means of an error based on the current sensors measurement. Thus the output of a Kalman filter is the mean value of the state estimate and the covariance matrix of its error. SHOE is fully interfaced with the external GENFIT library [81], providing both primary particles reconstruction, by using the BMN hits, and fragments track reconstruction, by combining the VTX, ITR and MSD hits and by matching the extrapolated tracks with the SCN and CAL hits.
- *HighLevel* - It is in charge of the fragment identification and cross section measurement by combining objects built from different detectors, in order to identify the different fragment and the primary beam particles and their tracks.

A scheme of the SHOE code structure is presented in figure 4.1.

## 4.2 Monte Carlo simulations

Monte Carlo (MC) simulations drove the design and optimization of FOOT detectors, helping to identify possible critical aspects in the layout. Through several

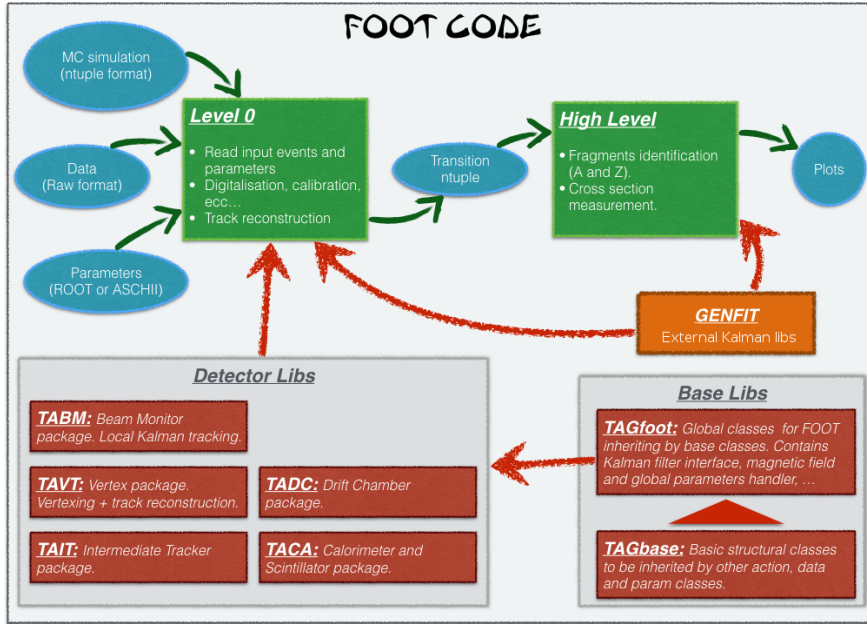


Figure 4.1: SHOE code scheme.

simulations the expected performances of the detectors were investigated and the different information they provide was combined in order to reconstruct the events and study how to improve the experimental accuracy. FLUKA [44, 10] is the MC code adopted to perform the simulations of the FOOT experimental setup, since it is an extremely robust code, being compared with a great amount of experimental data set and nowadays massively chosen in particle, nuclear and medical physics studies. FLUKA can simulate the transport and the interactions of photons, leptons, hadrons and ionized nuclei from a few keV (or from thermal energies for neutrons) up to cosmic ray energies in complex geometries, magnetic fields and in a wide range of materials [82]. Detailed information about MC simulation input file built for the FOOT experiment, its geometry and physics features and the specific output structure can be found in [83]. The simulations used in the analysis of this work makes use of the full geometry presented in Section 2.2.3. The origin of the reference frame in the FOOT geometry implemented in FLUKA coincides with the center of the target, and the detectors are disposed along the z axis, which is also the beam axis. The results presented in this section refer to an oxygen primary beam at 200 MeV/u and 700 MeV/u, chosen as reference energies for particle therapy and space radiation protection, respectively. In the case of 700 MeV/u, the MSD are placed at 62 cm in front of the target with a 5 cm gap between planes, the SCN is placed at 290 cm of distance from the target and the

CAL has a lateral shift of 9.77 cm in order to account for magnetic deflection. The 2-dimension schemes of the geometry used by FLUKA simulations for 200 MeV/u and 700 MeV/u primary beam are presented in Figure 4.2 (a) and (b), respectively. The targets are graphite (C) with a density  $\rho = 1.83 \text{ g/cm}^3$ , and polyethylene ( $C_2H_4$ ) with a density  $\rho = 0.94 \text{ g/cm}^3$ , both of them are 5 mm thick. As expected, the fragmentation rate is higher in carbon targets due to the higher density with respect to polyethylene (3.78 % and 2.79 %, respectively). The number of primary particles in the MC simulation for each combination of beam energy and target, as well as the corresponding number of interactions, is presented in Table 4.1. Because a low energy threshold for photons and electrons production leads to very long computing times and huge output files, a first set of simulations were performed with a transport threshold for photons, electrons,  $\gamma$ -ray and  $e^+e^-$  pairs set to 1 GeV. In the frame of FLUKA, this means that these particles are produced but they deposit their energy in the same point of creation. This allowed to considerably speed up the simulation runs and shrink the output files to an acceptable size. Moreover,  $e^+e^-$  pairs transport was switched off inside magnets and calorimeter, while photon transport was allowed everywhere, since it does not affect computing resources significantly. These choices were dictated by a trade off to keep under control the size of output files and CPU time, that would have been increased of  $\sim 30\%$ .

Target	Beam energy	Primary particles	Interaction events
C <sub>2</sub> H <sub>4</sub>	200 MeV/u	$5 \cdot 10^7$	1397243
	700 MeV/u	$1 \cdot 10^7$	121118
C	200 MeV/u	$1 \cdot 10^7$	377837
	700 MeV/u	$5 \cdot 10^6$	81533

### 4.3 Fragments identification

Since from MC is possible to retrieve all the hits belonging to the same fragment, a simulated track consists of a series of *hits* for each detector. All these reconstructed tracks are converted into *Track Objects* by the analysis code, which is based on ROOT and C++ classes. The analysis chain is then applied to this *Track Objects*, which is analogue to the one that should be produced in Level0 of SHOE during a real data acquisition. The first step of the analysis chain consists in the characterization of each generated particle. A nuclear fragment is uniquely identified when its charge Z and mass number A are correctly measured. The fundamental quantities for the fragments identification are the time of flight, momentum and kinetic energy release. Therefore, only particles tracked down by means of the magnetic spectrometer and measured by both SCN and CAL have been considered

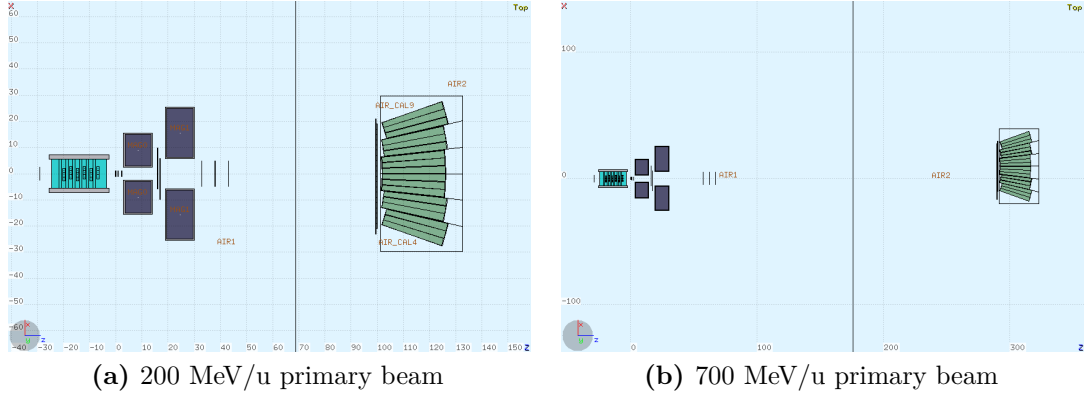


**Figure 4.2:** 2D view of the simulated FOOT geometry obtained with Flair GeoViewer [84] for a 200 MeV/u (a) and 700 MeV/u (b) primary beam.

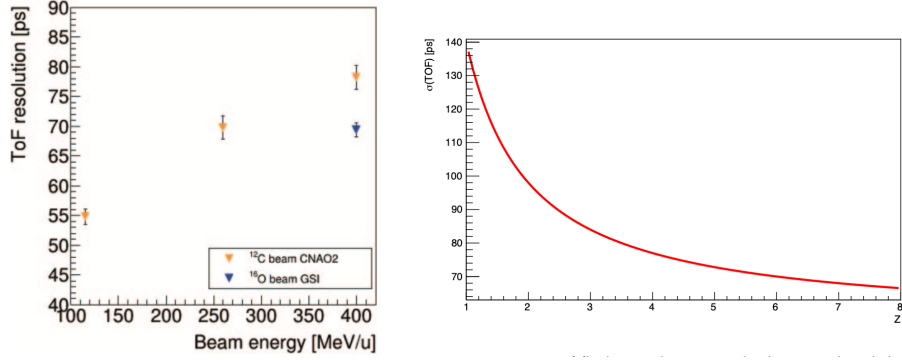
in the presented analysis. In the following, details about the quantities required for the fragments identification are presented.

The **Time of Flight** (TOF) is measured in FOOT using two timestamping stations, both built by plastic scintillators coupled to Silicon Photomultipliers (SiPM). The former is the SC placed before the target to count the incoming ions and to provide the start time, the latter is the SCN, placed in the downstream region to evaluate the fragment  $dE/dx$  and to assess the stop time. The evaluation procedure of time resolution of the FOOT apparatus can be found in [85]. The TOF resolution has been obtained from the performance measured during several experimental tests. The average TOF resolution for beams and energies experimentally tested ranges between 54 ps and 84 ps as a function of the beam kinetic energy, as reported in Figure 4.3(a), and it scales with the inverse of the energy released in the SCN, which increases with the charge of the particle according to Eq.1.1. Therefore, to reproduce this experimental trend, the time measurement resolution  $\sigma(TOF)$  has been empirically parametrised as a function of the particle charge as follow:

$$\sigma_{t_{SCN}} = A + \frac{B}{Z} \quad (4.1)$$

with A and B equal to 56 and 84, respectively. Referring to Eq.4.1, the time of flight resolution for C ions is  $\sigma(TOF) \simeq 70$  ps, while for H ions  $\sigma(TOF) \simeq 140$  ps. The trend of TOF resolution as a function of the particle charge is reported in Figure 4.3(b).

In order to reproduce the TOF experimental measurement, the *true* TOF value, which is the one produced by the simulation, is properly smeared in the analysis procedure. The tracking through the magnetic field provides the fragment path  $L$  from the production point to the entrance face in the SCN, that coupled with



(a) TOF resolution as function of beam energy (b) TOF resolution applied in the analysis procedure as a function of Z

**Figure 4.3:** (a) Measured TOF resolution as a function of the  $^{12}\text{C}$  and  $^{16}\text{O}$  beam energy [85]; (b) Time of Flight resolution applied to simulated data in the analysis procedure as a function of the particle charge Z.

the measurements of TOF and charge Z provides the velocity of the fragment in  $c$  units as follow:

$$\beta \cdot c = \frac{L}{TOF} \quad (4.2)$$

The *momentum* ( $p$ ) resolution takes into account the magnetic spectrometer detectors resolution, the magnetic field intensity and spatial extension and the MCS scattering, which decreases as the particle energy and mass increase. The studies performed by means of the Kalman filter on the basis of the spatial resolutions of the magnetic detectors spectrometers (few  $\mu\text{m}$  for M28 chips and few tens of  $\mu\text{m}$  for MSD) proved that in principle the momentum resolution improves with the primary particle energy, and therefore also with the fragment momentum, due to the reduction of MCS effect. However, in our case the difference is negligible and it can be considered constant. Because of the lower momentum of the light fragments, their resolution is slightly worse than for the heavier ones. The momentum relative resolution is derived from the MC generated and reconstructed momentum, respectively referred to as  $p_{gen}$  and  $p_{reco}$ , as follows:

$$\frac{\sigma(p)}{p} = \frac{p_{gen} - p_{reco}}{p_{reco}} \quad (4.3)$$

Studies about momentum resolution [83] show that a mean resolution of  $\sigma(p)/p=3.7\%$  can be assumed as a good approximation for all fragments, both for data collected at 200 MeV/u and 700 MeV/u. Then, the  $p$  reconstruction has been

determined by applying a Gaussian smearing of 3.7% to the all the momentum values obtained from FLUKA simulations.

The **Energy loss** ( $\Delta E$ ) has been reconstructed by the energy deposited in the plastic scintillator. Its resolution has been parametrized as a function of the deposited energy according to the results obtained in experimental tests as follows:

$$\sigma(\Delta E) = \alpha + \frac{\beta}{\Delta E} \quad (4.4)$$

with  $\alpha=0.904$  MeV and  $\beta=18.6$  MeV<sup>2</sup>.  $\sigma(\Delta E_{SCN})/\Delta E_{SCN}$  has been limited to the range [5 - 15]% according to the experimental results. The resolution associated to  $\Delta E$  measurement coincides with the one of SCN:

$$\sigma(\Delta E)/\Delta E = \sigma(\Delta E_{SCN})/\Delta E_{SCN} \quad (4.5)$$

The **Kinetic energy** ( $E_{kin}$ ) has been estimated by the energy deposition in the calorimeter. In order to take into account the energy deposited by charged fragments produced in re-fragmentation processes, the energy released in the calorimeter is retrieved from the sum of the energy releases in all the crystals hit by the fragment, as it will be done in real experimental data-taking where crystals are individually read and the energy deposited by different particles is summed up. However, neutrons production due to inelastic interactions leads to a systematic underestimation of  $E_{kin}$ , because they may deposit their energy far from the original fragment track or even escape the detector. The fraction of reconstructed energy obtained by the sum of the one released in the scintillator and calorimeter and their *true* production energy for a <sup>12</sup>C fragments generated by a 200 MeV/u and 700 MeV/u <sup>12</sup>O beam on a polyethylene target is reported in Figure 4.4 (a) and (b), respectively. The events in the tail increase from ~20% to ~80% when the primary beam energy increases from 200 MeV/u to 700 MeV/u due to the above mentioned neutron production and the higher energy deposition in other detectors and in air, which can not be experimentally measured. The same behaviour can be observed for all the other reconstructed fragments.

The resolutions of the calorimeter is evaluated as follow:

$$\frac{\sigma(E_{kin})}{E_{kin}} = \frac{c_1}{\sqrt{E_{kin}}} + \frac{c_2}{E_{kin}} + c_3 \quad (4.6)$$

where  $c_1=1.84$ ,  $c_2=96.16$ ,  $c_3=0.37$  are detector dependent constants. The FOOT calorimeter has been preliminary tested with H, He and C beams at different energies, finding that the CAL resolution is dominated by the constant term  $c_3$ , which is related to physics processes, electronic noise and detector related issues (intercalibration errors, longitudinal leakage, etc.). A relative resolution on the deposited energy in the calorimeter  $\sigma(E_{kin})/E_{kin} = 1.5\%$  has been estimated and thus applied as a Gaussian smearing to the MC kinetic energy production.

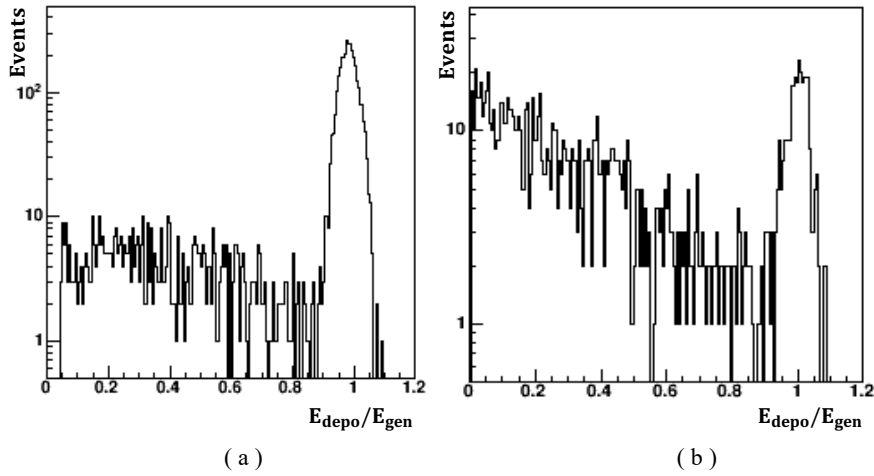


**Figure 4.4:** Ratio between the particles reconstructed energy in the scintillator and calorimeter and their *true* production energy for a  $^{12}\text{C}$  fragments generated by a 200 MeV/u (a) and 700 MeV/u (b)  $^{12}\text{O}$  beam impinging on a  $\text{C}_2\text{H}_4$  target.

### 4.3.1 Charge identification

The fragment charge  $Z$  is measured by combining  $\Delta E$  and TOF measurements of the SCN detector in Eq.1.1 and then by inverting it. The energy loss per unit path length ( $dE/dx$ ) can be obtained as the ratio between the energy release in the SCN and the thickness of the two SCN layers, while  $\beta$  is related to the TOF measurement according to Eq.4.2. As shown in Figure 4.5, the SCN and TOF resolutions allow the discrimination of eight regions in the  $\Delta E$ -TOF plane, each one related to different fragment charge. Charge identification for a 200 MeV/u and 700 MeV/u  $^{16}\text{O}$  beam impinging into a polyethylene target is presented in Figure 4.6 (a) and (b), respectively. In Tab. 4.2 the  $Z$  values and their resolutions estimated through this method are reported. The peaks result well separated from each other, allowing a clear charge determination. The charge resolution improves with increasing fragment charge, spanning from  $\sim 6\%$  for hydrogen to  $\sim 2\%$  for oxygen in the case of a  $^{16}\text{O}$  primary beam at 200 MeV/u. The presence of a secondary peak before the primary peak of hydrogen both for 200 MeV/u and 700 MeV/u  $^{16}\text{O}$  primary beam is at the moment under further investigation.

Fragment	200 MeV/u		700 MeV/u	
	$Z$	$\sigma(Z)$ [%]	$Z$	$\sigma(Z)$ [%]
H	1.01	6.7	0.9	15.0
He	2.02	3.7	2.0	8.7
Li	3.03	3.2	2.99	5.8

Be	4.06	4.0	4.00	4.4
B	5.07	3.0	5.01	3.5
C	6.11	2.9	6.02	3.2
N	7.14	2.9	7.03	3.1
O	8.19	2.8	8.04	2.9

**Table 4.2:** Reconstructed Z for fragments generated by a  $^{16}\text{O}$  beam impinging on a  $\text{C}_2\text{H}_4$  target at 200 MeV/u and at 700 MeV/u.

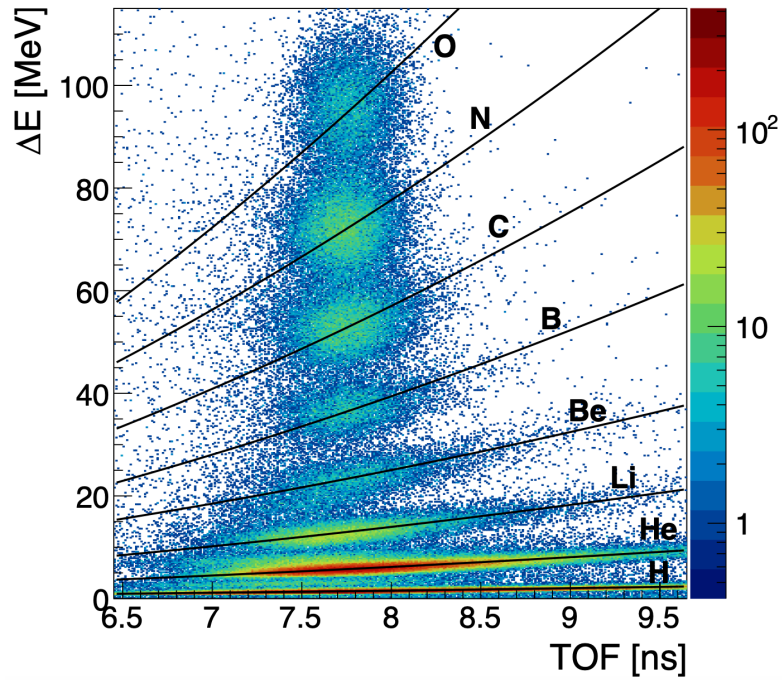


**Figure 4.5:** Charge identification of fragments produced by a  $^{16}\text{O}$  beam at 200 MeV/u using the energy loss in the SCN  $\Delta E$  and the TOF measurement performed together to the SC. Black lines represent Bethe-Bloch curves related to each fragment.

### 4.3.2 Mass identification

The redundancy of subdetectors in the FOOT electronic apparatus is the key factor for the isotopic discrimination. As a matter of fact, the measurements of Time of Flight, momentum and kinetic energies can be combined to perform the isotopic identification in three different ways, as follows:

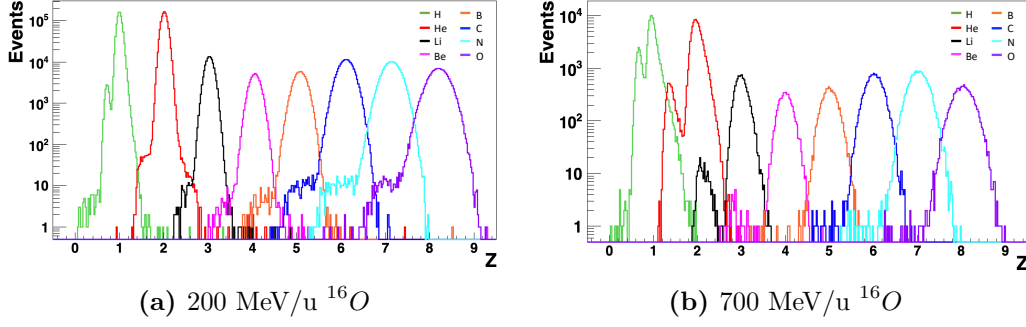


**Figure 4.6:** Z distributions of the reconstructed fragments produced by a  $^{16}\text{O}$  beam at 200MeV/u (a) and at 700 MeV/u (b) impinging on a polyethylene target.

- *Combination of  $p$  and TOF*

The fragment mass  $m$  is related to the momentum  $p$  and particle velocity in c units  $\beta$  according to the expression:

$$p = m\gamma\beta c \quad (4.7)$$

where

$$\gamma = \frac{1}{\sqrt{1 - \beta^2}} \quad (4.8)$$

Thus, the mass number  $A_1$  can be calculated using  $p$  and  $TOF$  as follow:

$$A_1 = \frac{m}{u} = \frac{1}{u} \frac{p}{\gamma\beta c} \quad (4.9)$$

where the atomic mass unit is  $u=931.494 \text{ MeV}/c^2$ . Consequently its resolution can be evaluated as:

$$\begin{aligned} \sigma(A_1) &= \sqrt{\left(\frac{\partial A_1}{\partial p} \sigma(p)\right)^2 + \left(\frac{\partial A_1}{\partial \beta} \frac{\partial \beta}{\partial TOF} \sigma(TOF)\right)^2} \\ &= \frac{1}{u} \frac{p}{\beta c} \sqrt{\frac{1}{\gamma^2} \left(\frac{\sigma(p)}{p}\right)^2 + \frac{\gamma^2}{\beta^2} \frac{L^2}{c^2 TOF^2} \sigma^2(TOF)} \end{aligned} \quad (4.10)$$

### 4.3 – Fragments identification

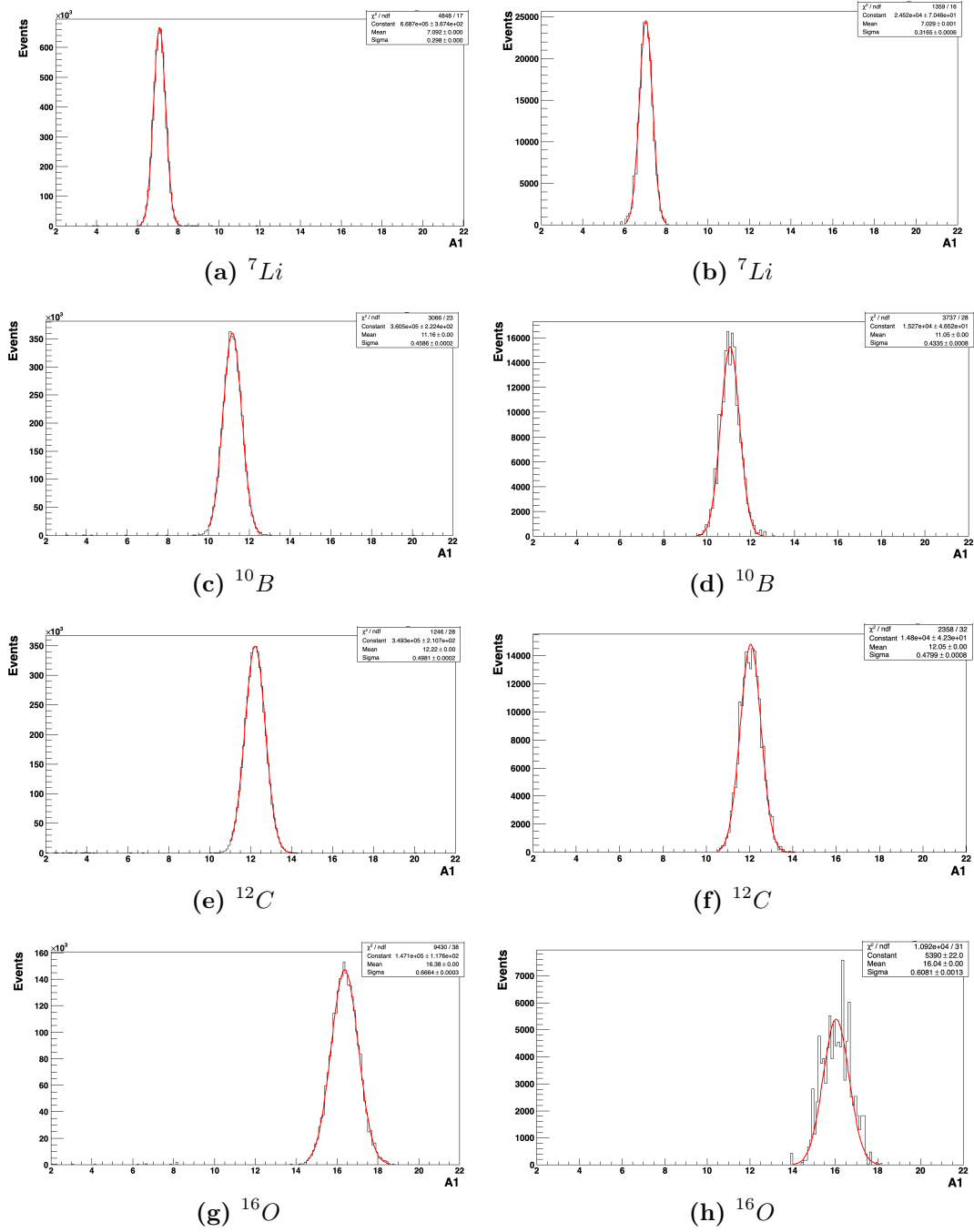


**Figure 4.7:**  $A_1$  distributions for the isotopes of fragments produced by a  $^{16}\text{O}$  beam at 200 MeV/u (left column) and at 700 MeV/u (right column) impinging on a  $\text{C}_2\text{H}_4$  target.

- *Combination of TOF and  $E_{kin}$*

The kinetic energy can be related to the mass of the fragment as follows:

$$E_k = (\gamma - 1)mc^2 \quad (4.11)$$

Thus, the mass number A2 and its resolution can be written as follow:

$$A_2 = \frac{m}{u} = \frac{1}{u} \frac{E_k}{(\gamma - 1)c^2} \quad (4.12)$$

$$\begin{aligned} \sigma(A_2) &= \sqrt{\left(\frac{\partial A_2}{\partial E_k} \sigma(E_k)\right)^2 + \left(\frac{\partial A_2}{\partial \beta} \frac{\partial \beta}{\partial TOF} \sigma(TOF)\right)^2} \\ &= \frac{1}{u} \frac{E_k}{\beta c} \frac{\gamma}{\gamma - 1} \sqrt{\frac{1}{\gamma^2} \left(\frac{\sigma(E_k)}{E_k}\right)^2 + \frac{\beta^2 \gamma^4}{(\gamma - 1)^2} \frac{L^2}{c^2 TOF^2} \sigma^2(TOF)} \end{aligned} \quad (4.13)$$

- *Combination of  $p$  and  $E_{kin}$*

The particle total energy can be expressed as the sum of its kinetic and rest energies, or as a function of the particle momentum, as follow:

$$E = E_k + mc^2 \quad (4.14)$$

$$E = \sqrt{p^2 c^2 + m^2 c^4} \quad (4.15)$$

By combining the previous two equation, the mass can be described as:

$$m = \frac{p^2 c^2 - E_k^2}{2c^2 E_k} \quad (4.16)$$

Therefore, the mass number A3 and its resolution can be expressed as follow:

$$A_3 = \frac{m}{u} = \frac{1}{u} \frac{p^2 c^2 - E_k^2}{2c^2 E_k} \quad (4.17)$$

$$\begin{aligned} \sigma(A_3) &= \sqrt{\left(\frac{\partial A_3}{\partial p} \sigma(p)\right)^2 + \left(\frac{\partial A_3}{\partial E_k} \sigma(E_k)\right)^2} \\ &= \frac{1}{u} \frac{1}{E_k} \sqrt{p^4 \left(\frac{\sigma(p)}{p}\right)^2 + \frac{p^2 c^2 + E_k^2}{4c^4} \left(\frac{\sigma(E_k)}{E_k}\right)^2} \end{aligned} \quad (4.18)$$

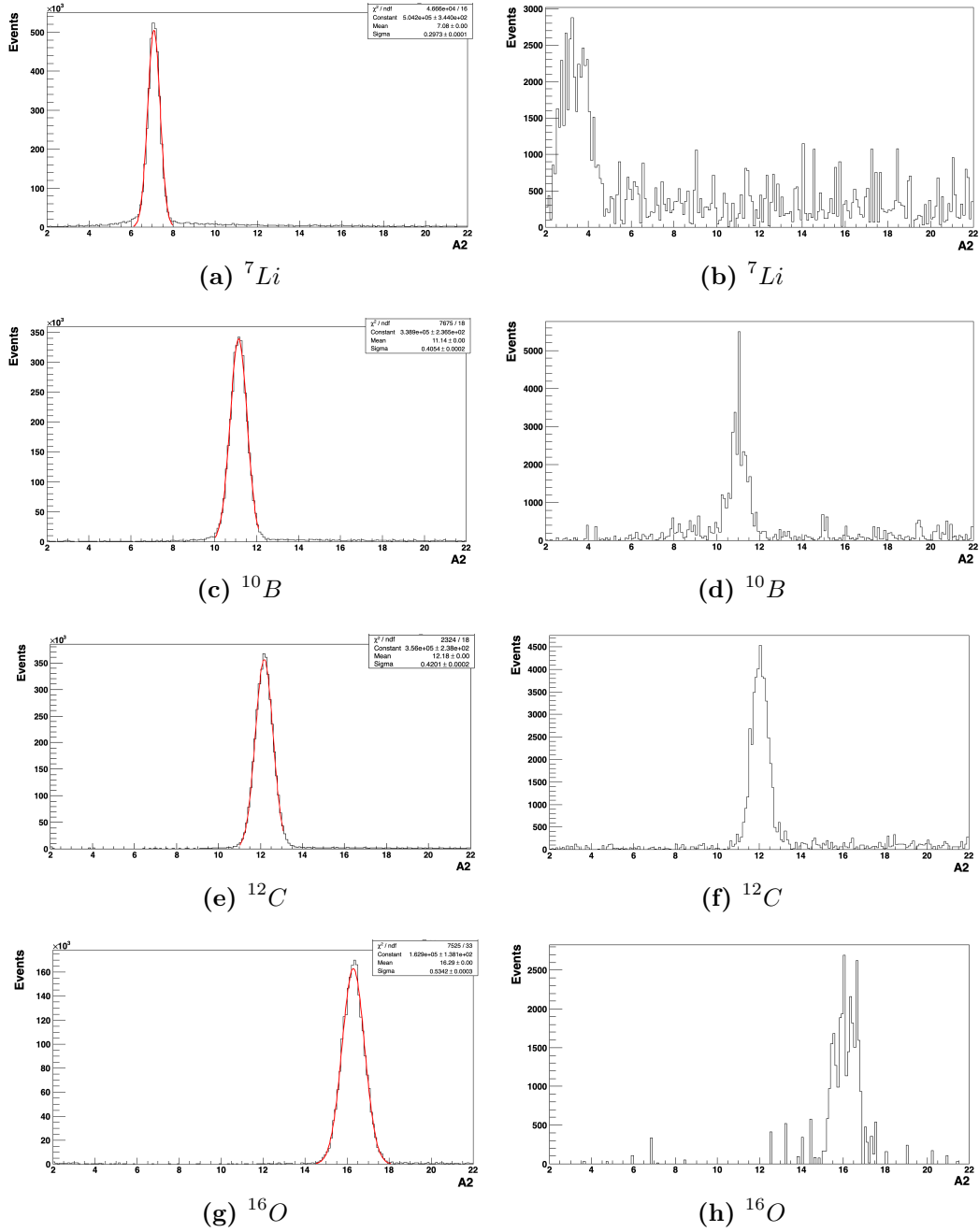


**Figure 4.8:**  $A_2$  distributions for the isotopes of fragments produced by a  ${}^{16}\text{O}$  beam at 200 MeV/u (left column) and at 700 MeV/u (right column) impinging on a polyethylene target.

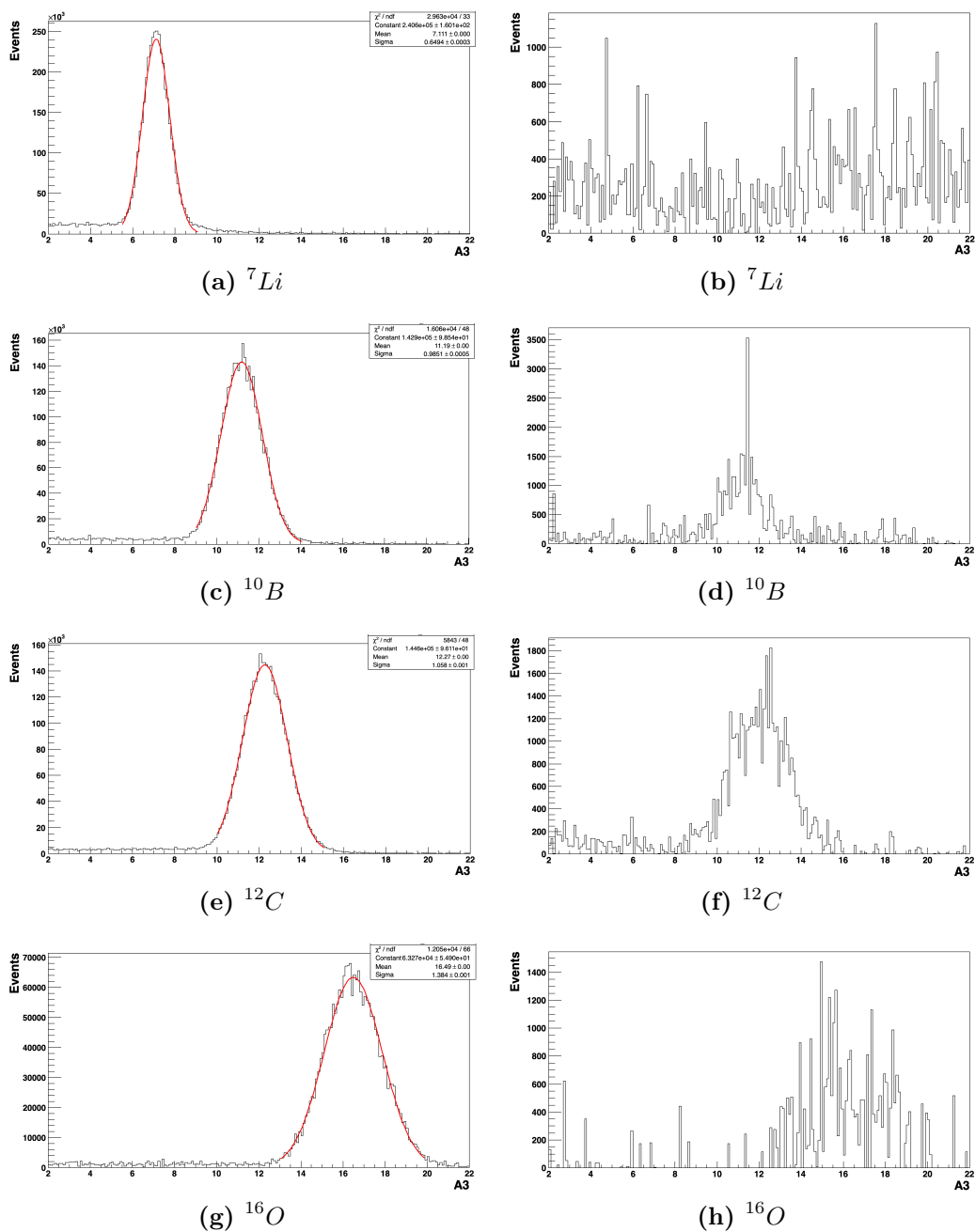


**Figure 4.9:**  $A_3$  distributions for the isotopes of fragments produced by a  $^{16}\text{O}$  beam at 200 MeV/u (left column) and at 700 MeV/u (right column) impinging on a polyethylene target.

The three different mass determinations exhibit an obvious correlation because of the presence of a common sub-detector for each couple of A definition. Figures 4.7, 4.8, 4.9 show the distributions of the obtained  $A_1$ ,  $A_2$ ,  $A_3$  values respectively for some selected fragments produced by  $^{16}\text{O}$  beam at 200 MeV/u and 700 MeV/u impinging on a polyethylene target. The number of mass peak positions retrieved with the three method are centered around the expected values with in some cases a shift completely included in the resolution. The width of the distributions is due to the resolutions applied to the quantities involved in the mass evaluation. The mass resolution is  $\sim 3.5\%$  for  $A_2$  and slightly worst for  $A_1$ , while it is larger than  $8\%$  in the  $A_3$  case due to the error propagation in Eq. 4.18. The tail corresponding to an underestimation of the mass is visible in all the  $A_2$  and  $A_3$  reported plots is due to an underestimation of the fragment kinetic energy, mainly caused by neutron emission inside the calorimeter. The tail is especially pronounced in the case of a 700 MeV/u, as already discussed in Sec.4.3.1.

A fit procedure that simultaneously contains the three correlated mass number ( $A_1$ ,  $A_2$ ,  $A_3$ ) is implemented in order to retrieve the best value. Two different approaches could be applied:

- **Standard  $\chi^2$  minimization**

The method relies on the minimization of a function defined as follow:

$$\chi^2 = \frac{(TOF - \overline{TOF})^2}{\sigma^2(TOF)} + \frac{(E_{kin} - \overline{E_{kin}})^2}{\sigma^2(E_{kin})} + \frac{(p - \overline{p})^2}{\sigma^2(p)} + \mathbf{A}^T \mathbf{B} \mathbf{A} \quad (4.19)$$

where  $TOF$ ,  $E_{kin}$ ,  $p$  are the reconstructed quantities and  $\sigma(TOF)$ ,  $\sigma(E_{kin})$ ,  $\sigma(p)$  their uncertainties, while  $\overline{TOF}$ ,  $\overline{E_{kin}}$ ,  $\overline{p}$  are the fit output parameters.  $\mathbf{A}$  is the difference vector between the reconstructed number of mass values ( $A_1$ ,  $A_2$ ,  $A_3$ ) and the mass output parameter ( $\overline{A}$ ), defined as:

$$\mathbf{A} = (A_1 - \overline{A}; A_2 - \overline{A}; A_3 - \overline{A}) \quad (4.20)$$

The matrix  $\mathbf{B}$  takes into account the correlation between  $A_1$ ,  $A_2, A_3$  by collecting the evaluation of their uncertainties.  $\mathbf{B}$  is related to the correlation matrix  $\mathbf{C}$ , which is expressed by:

$$\mathbf{B} = (\mathbf{C}\mathbf{C}^T)^{-1} \quad (4.21)$$

$$\mathbf{C} = \begin{pmatrix} \frac{\partial A_1}{\partial TOF} \sigma(TOF) & \frac{\partial A_1}{\partial p} \sigma(p) & 0 \\ \frac{\partial A_2}{\partial TOF} \sigma(TOF) & 0 & \frac{\partial A_2}{\partial E_{kin}} \sigma(E_{kin}) \\ 0 & \frac{\partial A_3}{\partial p} \sigma(p) & \frac{\partial A_3}{\partial E_{kin}} \sigma(E_{kin}) \end{pmatrix} \quad (4.22)$$

The best values of the outfit parameter are obtained minimizing the  $\chi^2$  function.

- **Augmented Lagrangian Method (ALM)**

The ALM method is based on the minimization of a Lagrangian function  $\mathcal{L}$  defined as follow:

$$\mathcal{L}(\vec{x}; \boldsymbol{\lambda}; \mu) \equiv f(\vec{x}) - \sum_{a=1}^m \lambda_a c_a(\vec{x}) + \frac{1}{2\mu} \sum_{a=1}^m c_a^2(\vec{x}) \quad (4.23)$$

$f(\vec{x})$  is the objective function and is expressed as

$$f(\vec{x}) = \frac{(TOF - \overline{TOF})^2}{\sigma^2(TOF)} + \frac{(E_{kin} - \overline{E_{kin}})^2}{\sigma^2(E_{kin})} + \frac{(p - \overline{p})^2}{\sigma^2(p)} + \mathbf{A}^T \mathbf{B} \mathbf{A} \quad (4.24)$$

while the last two terms are defined as

$$\begin{aligned} \sum_{a=1}^m \lambda_a c_a(\vec{x}) + \frac{1}{2\mu} \sum_{a=1}^m c_a^2(\vec{x}) &= \lambda_1(A_1 - \overline{A}) + \lambda_2(A_2 - \overline{A}) + \lambda_3(A_3 - \overline{A}) \\ &+ \frac{1}{2\mu} \left( (A_1 - \overline{A})^2 + (A_2 - \overline{A})^2 + (A_3 - \overline{A})^2 \right) \end{aligned} \quad (4.25)$$

$c_a$  are the constraints,  $\boldsymbol{\lambda}$  is a  $m$ -dimension vector of Lagrangian multipliers  $\lambda_a$ , and  $\mu$  is the penalty parameter. The last term of Eq. 4.23, called *penalty term*, is a function of the constraints weighted by a positive penalty parameter  $\mu$ . Eq. 4.23 is performed by iteration: unconstrained minimization of  $\mathcal{L}(\vec{x}; \boldsymbol{\lambda}; \mu)$  is solved and new  $\boldsymbol{\lambda}$  and  $\mu$  values are selected at each step. The procedure is reiterated until the required levels of agreement is reached.

Only the standard  $\chi^2$  minimization method was implemented in the present work, because it was already demonstrated that the two methods provide similar results for what concern both the mean value and the associated uncertainty [83]. By plotting the  $\chi^2$  value as a function of the fragment number of mass, as presented in Figure 4.10 for the case of  $^{12}\text{C}$  produced respectively by a 200 MeV/u and 700 MeV/u oxygen beam into a polyethylene target, a long tail of wrong reconstructed mass due to underestimation of kinetic energy is evident at high  $\chi^2$  values. In order to improve the relative resolution on the mass value determination, a  $\chi^2$  cut can be required. The cut value has been selected in order not to reduce too much the statistics for the heavier fragments ( $Z \geq 3$ ), which decreases of  $\sim 20\%$  with a  $\chi^2 < 5$  cut. Cleaning up the distributions is particularly useful to separate different isotopes of the same element. The achievable mass resolution after the application of the  $\chi^2$  cut ranges between  $\sim 3.5\%$  and  $\sim 4.5\%$ , as reported in Table 4.3 for the most abundant produced isotopes. Specifically, the improvement after the  $\chi^2$  cut with respect to the mass  $A_1$  is  $\sim 0.5\%$  and to the masses  $A_2$  and  $A_3$  is  $\sim 3\%$  for both the cases at 200 MeV/u and 700 MeV/u. Due to the frequent underestimation of the fragment kinetic energy at 700 MeV/u, the determination of the fragment mass number at high energies is only performed through the  $A_1$  estimation, which combines *TOF* and *p* measurements and therefore does not present any tail.

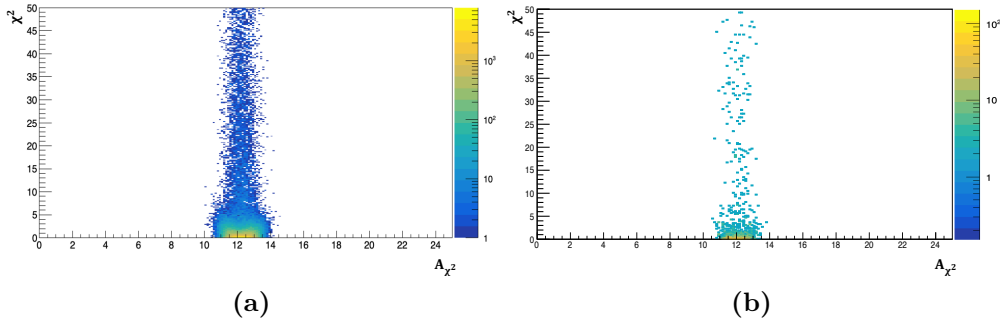


**Figure 4.10:**  $\chi^2$  versus  $A_{\chi^2}$  for  $^{12}\text{C}$  fragments produced by 200 MeV/u (a) and 700 MeV/u (b)  $^{16}\text{O}$  beam impinging on a  $\text{C}_2\text{H}_4$  target, respectively. To discard the badly reconstructed fragments belonging to the tail, a  $\chi^2 < 5$  cut can be applied.

Fragment	$A_{\chi^2}^{cut}$ - 200 MeV/u	$A_{\chi^2}^{cut}$ - 700 MeV/u
$^6\text{Li}$	$6.1 \pm 0.3$	$6.0 \pm 0.2$
$^7\text{Li}$	$7.1 \pm 0.3$	$7.0 \pm 0.3$
$^8\text{Li}$	$8.1 \pm 0.3$	$8.0 \pm 0.3$
$^7\text{Be}$	$7.1 \pm 0.3$	$7.0 \pm 0.3$
$^8\text{Be}$	$8.3 \pm 0.4$	$8.3 \pm 0.4$

${}^9\text{Be}$	$9.1\pm 0.4$	$9.0\pm 0.4$
${}^8\text{B}$	$8.2\pm 0.3$	$8.0\pm 0.3$
${}^9\text{B}$	$9.3\pm 0.3$	
${}^{10}\text{B}$	$10.2\pm 0.4$	$10.1\pm 0.4$
${}^{11}\text{B}$	$11.2\pm 0.5$	$11.1\pm 0.4$
${}^{12}\text{B}$	$12.2\pm 0.5$	$12.1\pm 0.5$
${}^9\text{C}$	$9.3\pm 0.4$	$9.1\pm 0.3$
${}^{10}\text{C}$	$10.2\pm 0.4$	$10.1\pm 0.5$
${}^{11}\text{C}$	$11.2\pm 0.5$	$11.1\pm 0.5$
${}^{12}\text{C}$	$12.2\pm 0.5$	$12.1\pm 0.5$
${}^{13}\text{C}$	$13.2\pm 0.5$	$13.1\pm 0.5$
${}^{14}\text{C}$	$14.2\pm 0.6$	$14.2\pm 0.6$
${}^{12}\text{N}$	$12.2\pm 0.5$	$12.2\pm 0.5$
${}^{13}\text{N}$	$13.3\pm 0.5$	$13.2\pm 0.5$
${}^{14}\text{N}$	$14.3\pm 0.6$	$14.1\pm 0.6$
${}^{15}\text{N}$	$15.3\pm 0.6$	$15.1\pm 0.6$
${}^{14}\text{O}$	$14.3\pm 0.6$	$14.1\pm 0.5$
${}^{15}\text{O}$	$15.4\pm 0.6$	$15.1\pm 0.6$
${}^{16}\text{O}$	$16.4\pm 0.7$	$16.1\pm 0.6$

**Table 4.3:** A values and relative precision obtained by fitting with a Gaussian function the mass distribution of each fragment obtained after a standard  $\chi^2$  minimization with a  $\chi^2 < 5$  cut for a  ${}^{16}\text{O}$  beam at 200 MeV/u and 700 MeV/u impinging on a  $\text{C}_2\text{H}_4$  target.

## 4.4 Cross section measurements

The capability of the detectors to perform cross section measurements has been evaluated relying only on MC simulated data, by considering odd events as real data and the even as MC ones. At the end, the comparison between the Fluka generated cross sections and the reconstructed ones has been accomplished. The mass  $A$  and charge  $Z$  identification is required for the reconstruction of the fragments yield as a function of the emission angle  $\theta$  or the production energy  $E_{kin}$ , indicated as  $Y(\theta)$  and  $Y(E_{kin})$  respectively. The production differential cross sections are defined as follow:

$$\frac{\sigma_f}{d\theta} = \frac{(Y_f(\theta) - Bgk_f)^U}{N_{prim}N_t\Omega_\theta\epsilon} \quad (4.26)$$

$$\frac{\sigma_f}{dE_{kin}} = \frac{(Y_f(E_{kin}) - Bgk_f)^U}{N_{prim}N_t\Omega_E\epsilon} \quad (4.27)$$

Subscript  $f$  indicates the  $f^{\text{th}}$  fragment defined by the reconstructed  $Z$  and  $A$  values,  $Bkg$  is the *background* present in each fragment production, and  $U$  the *unfolding* process, both explained in details in the following,  $N_{prim}$  is the number of primary beam particles,  $N_t$  is the number of target scattering center,  $\Omega_\theta$  and  $\Omega_E$  are the angular and energy phase spaces respectively,  $\epsilon$  is the reconstruction efficiency. The study presented in this work focuses on the identification of carbon isotopes, which are emitted in a very small angle. For this reason, the results only refer to  $\frac{\sigma_f}{dE}$ . Details of all the terms involved in Eq. 4.27 are presented in the following:

- The yield distribution  $Y(E)$  has been retrieved selecting before the charge  $Z$  and then applying the mass identification  $A$  evaluated with the standard  $\chi^2$  minimization method. Only fragments which cross all the detectors reaching the calorimeter and survive the  $\chi^2 < 5$  cut are taken into account. Their distribution is then fitted with the sum of several Gaussian functions, each one characterizing a specific isotope. The three parameters describing each Gaussian function represent the number of events of the isotope, its mass and the relative resolution. Figures 4.11 (a) and (b) show carbon isotopes reconstruction for a 200 MeV/u and 700 MeV/u  $^{16}\text{O}$  beam impinging on a polyethylene target. At 700 MeV/u the statistics is too poor to correctly identify  $^9\text{C}$ .

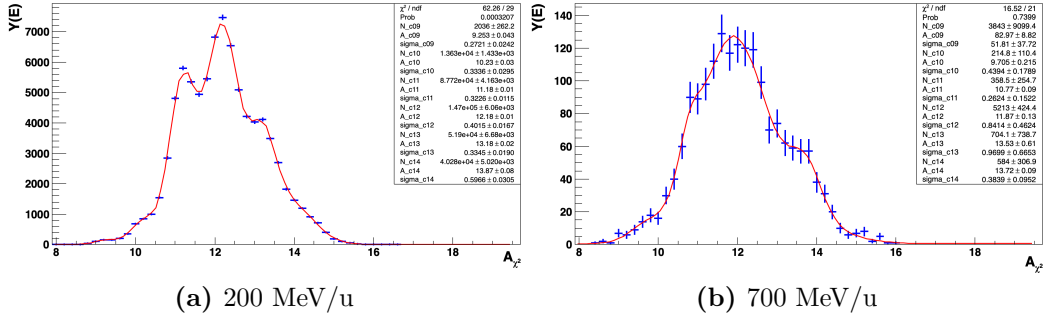


**Figure 4.11:** Blue dots represent the reconstructed yield for carbon fragments produced by a 200 MeV/u (a) and 700 MeV/u (b)  $^{16}\text{O}$  beam impinging on a  $\text{C}_2\text{H}_4$  target as a function of the mass number  $A$  evaluated with the standard  $\chi^2$  minimization method. The red solid lines show the fit with the sum of six Gaussian function, each one for a specific carbon isotopes ( $^9\text{C}$ ,  $^{10}\text{C}$ ,  $^{11}\text{C}$ ,  $^{12}\text{C}$ ,  $^{13}\text{C}$ ,  $^{14}\text{C}$ ). For the case at 700 MeV/u the statistics is too poor to identify  $^9\text{C}$ .

- The background evaluation  $Bkg$  represents the probability that the mass number of a fragment, called  $a$ , is misidentified as a different one, called  $b$ ,  $c$ ,

etc. These probabilities  $t$  can be expressed through a matrix, as follows:

$$\begin{pmatrix} t^{aa} & t^{ab} & t^{ac} & \dots \\ t^{ba} & t^{bb} & t^{bc} & \\ t^{ca} & t^{cb} & t^{cc} & \\ \vdots & & & \ddots \end{pmatrix} \quad (4.28)$$

The diagonal elements of the matrix represent the probability of a correct mass number identification, while the other elements outside the diagonal correspond to the misidentification probability and will be used to correct the cross section evaluation. At the moment, the  $Bkg$  evaluation has been quantified using the truth of MC, afterward it will be extracted by data.

- The detector precision provides a finite resolution of the kinematic quantities reconstructed that in a differential cross section measurements can in some cases conduct to a wrong counts of the produced fragments in a defined energy range. The so called *unfolding* process, indicated as  $U$  in Eq. 4.27, corrects the measured distribution from the mentioned experimental effects by means of a correction matrix  $\mathbf{A}$ , which correlates the true kinetic energy distribution  $\mathbf{x}$  and the measured one  $\mathbf{y}$ , as follow:

$$\mathbf{Ax} = \mathbf{y} \quad (4.29)$$

In order to obtain the true distribution, the correlation matrix must be inverted and applied to the experimental measured quantities:

$$\mathbf{x} = \mathbf{A}^{-1}\mathbf{y} \quad (4.30)$$

Because of the inversion of the matrix in not a trivial task, advanced and robust statistics procedure are required [86]. This step was performed by means of the ROOT Unfolding Framework (*RooUnfold*) [87] package.

- In the results referring to MC data, the number of primary particles  $N_{prim}$  is the number of primary particles generated in the simulation, while in the real data analysis is provided by the SC detector.
- The number of scattering centers  $N_t$  can be expressed as a function of the Avogadro's number  $N_A$ , the target density  $\rho$ , mass number  $A$  and thickness , as follow:

$$N_t = \frac{\rho N_A z}{A} \quad (4.31)$$

- The phase space  $\Omega_E$  is expressed as function of the energy lower and upper limits of the  $i^{th}$  bin of the corresponding yield distribution of the fragment  $f$ , as follows:

$$\Omega_E = E_{max}^f - E_{min}^f \quad (4.32)$$

$E_{min}^f, E_{max}^f$  are the above mentioned limits. In the present work, the energy bins width have been selected in order to have almost the same amount of particles in each bin. The energy bin selection for carbon fragments evaluation in the case of 200 MeV/u and 700 MeV/u Oxygen beam impinging on a  $C_2H_4$  target is showed in Figure 4.12 (a) and (b), respectively. The relative numerical values are reported in Table 4.4.

Beam energy	Bin separation [MeV/u]
200 MeV/u	50, 120, 164, 176, 182, 188, 194, 200, 225, 300
700 MeV/u	550, 620, 664, 676, 682, 688, 694, 700, 725, 800

**Table 4.4:** Energetic bin separation selected for the analysis presented in this work for a 200 MeV/u and 700 MeV/u  $^{16}O$  beam impinging on a polyethylene and graphite target.

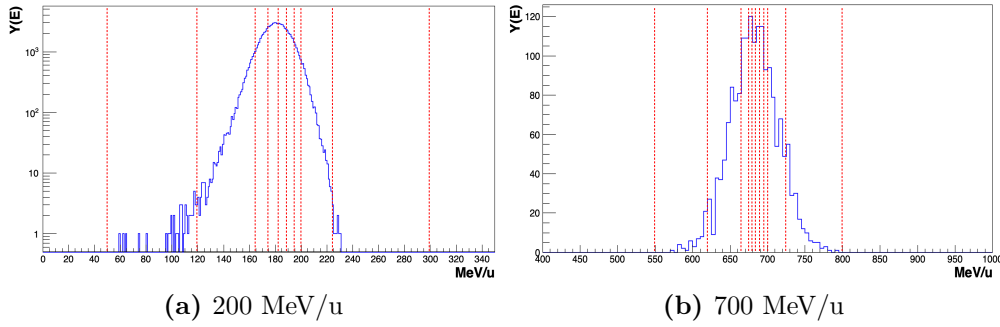


**Figure 4.12:** Solid blue line represents the energetic yields of  $^{12}C$  fragments produced by a 200 MeV/u (a) and 700 MeV/u (b)  $^{16}O$  beam impinging on a polyethylene target. The vertical red dashed lines represent the energetic bins selection reported in Tab. 4.4.

- The efficiency  $\epsilon$  should take into account the processes of measurement and reconstruction used for the cross section evaluation. A preliminary estimation of  $\epsilon$  considers the percentage of tracks with a given charge  $Z$  and mass number  $A$  that are not reconstructed because of physical reasons, such as fragments that are not able to cross all the detectors because of their too low energy, fragments that undergo re-fragmentation in some elements of the apparatus before reaching the calorimeter, fragments emitted at large angle out of the detector geometrical acceptance or low quality reconstructed fragments that do not pass the  $\chi^2$  threshold (see Figure 4.13(a)). Thus the efficiency has

been evaluated for each energy interval, as follow:

$$\epsilon = \frac{c_i}{n_i} \quad (4.33)$$

$c_i$  is the number of correctly reconstructed fragments within the  $i^{\text{th}}$  bin, while  $n_i$  is number of *true* fragments generated in the same bin. An example of efficiency evaluation for the case of  $^{12}\text{C}$  fragments generated by a 200 MeV/u oxygen beam on a polyethylene target is reported in Figure 4.13. Because the efficiency is evaluated accordingly to the binomial distribution, its variance can be expressed as:

$$\sigma^2(\epsilon_i) = \overline{\epsilon_i^2} - \overline{\epsilon_i}^2 \quad (4.34)$$

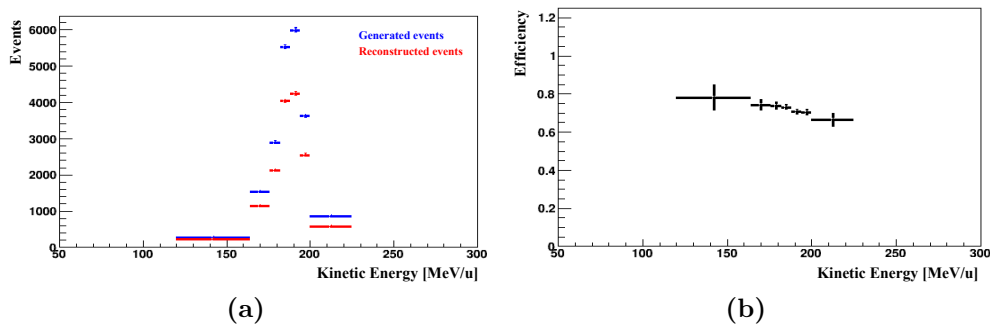


**Figure 4.13:** (a) Comparison between the generated (red dots) and reconstructed (blue dots)  $^{12}\text{C}$  particles as a function of the kinetic energy produced by a 200 MeV/u  $^{16}\text{O}$  beam impinging on  $\text{C}_2\text{H}_4$  target and (b) corresponding efficiency evaluated with Eq. 4.33.

The total reconstruction cross section has been evaluated summing all the differential cross section bin and have been compared with the total generated cross sections for carbon isotopes ( $^9\text{C}$ ,  $^{10}\text{C}$ ,  $^{11}\text{C}$ ,  $^{12}\text{C}$ ,  $^{13}\text{C}$ ,  $^{14}\text{C}$ ) produced by a 200 MeV/u and 700 MeV/u  $^{16}\text{O}$  beam impinging on polyethylene and carbon targets evaluated following the procedure presented above, while the cross sections on hydrogen can be retrieved according to Eq. 2.4. The numerical comparisons for both beam energies and targets are presented in Tab. 4.5 and 4.6. The number of primary particles in the MC simulation used to evaluate the cross sections estimation here reported (see Tab. 4.1) is a trade off between the approximately minimum sample size that should be required in real data acquisition to get good results and the one that can realistically be acquired with the DAQ system presented in Section 2.2.3. Clearly, by increasing the statistics, the agreement between MC predicted and reconstructed results improves. Specifically, the agreement with the generated cross section of the most produced carbon fragments (i.e.,  $^{11}\text{C}$ ,  $^{12}\text{C}$ ,  $^{13}\text{C}$ ,) is inside  $\sim 25\%$

for both the samples at 200 MeV/u. Therefore, the cross section on a hydrogen target can be confidently retrieved by applying the method presented in Sec. 2.2.1 to  $^{12}\text{C}$  at 200 MeV/u. In order to check all the analysis chain of the target cross sections combination presented in Sec. 2.2.1, the evaluated cross section have been compared with the MC prediction too. The result is reported in Tab. 4.7. The good agreement between MC cross section prediction and the reconstructed value validate the combination method. The statistics for the case of C target is too poor to perform a reliable cross section reconstruction both in direct and inverse kinematics. Only statistical errors are reported in the results presented, but a real data acquisition will be more likely affected by systematic errors, for example possible misalignment of the tracking detectors resulting in an incorrect momentum estimation, fragments kinetic energy underestimation due to neutron production, cross feed probability. All these contributions have been investigated by varying the resolution of the detected quantities (see Sec. 4.5). In Figure 4.14 the true and measured  $^{12}\text{C}$  cross sections are compared, for the case of polyethylene and graphite targets both at 200 MeV/u and 700 MeV/u.

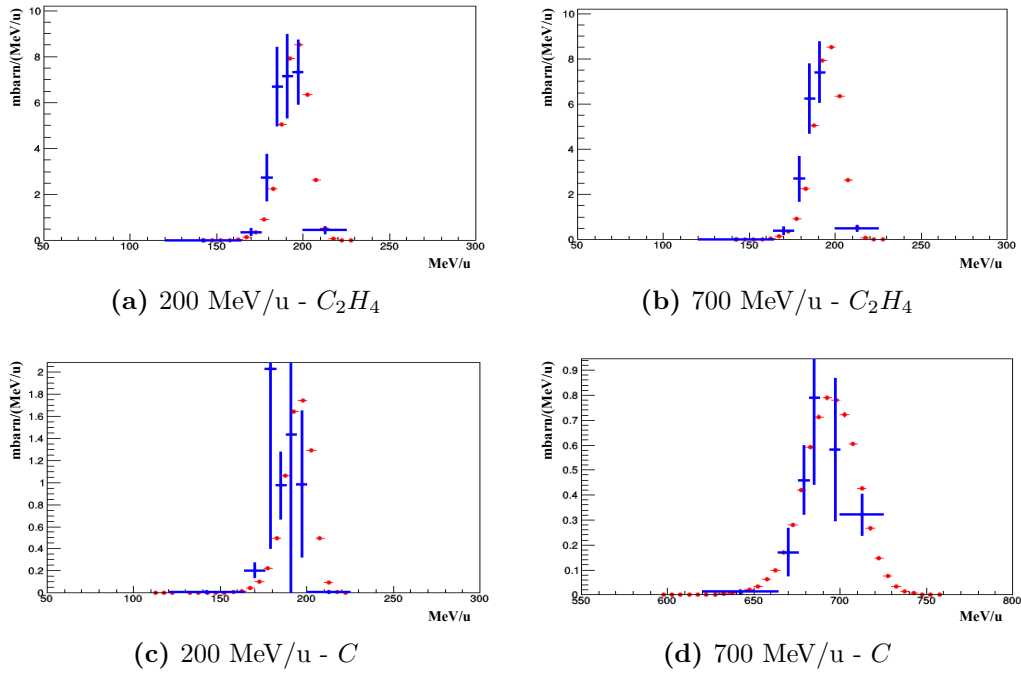


**Figure 4.14:** Comparison between the MC (red dots) and reconstructed (blue dots) differential cross sections as a function of the fragment kinetic energy for  $^{12}\text{C}$  produced by a 200 MeV/u (left column) and 700 MeV/u (right column)  $^{16}\text{O}$  beam impinging on  $\text{C}_2\text{H}_4$  and C target.

Beam energy	Fragment	Target : $C_2H_4$		
		$\sigma_{gene}$ [mbarn]	$\sigma_{reco}$ [mbarn]	$\frac{\sigma_{reco}}{\sigma_{gene}}$
200 MeV	$^9C$	2.7±0.1	1.1±0.1	0.4±0.3
	$^{10}C$	15.7±0.2	8.5±0.3	0.5±0.1
	$^{11}C$	122.0±0.6	88.6±1.2	0.7±0.03
	$^{12}C$	174.1±0.7	182.1±2.1	1.0±0.01
	$^{13}C$	99.42±0.5	83.3±1.3	0.8±0.02
	$^{14}C$	27.68±0.2	27.85±0.8	1.0±0.04
700 MeV	$^9C$	3.6±0.1	–	–
	$^{10}C$	15.2±0.2	7.4±1.1	0.5±0.3
	$^{11}C$	95.5±0.4	40.9±2.6	0.4±0.2
	$^{12}C$	148.4±0.6	155.3±8.3	1.0±0.1
	$^{13}C$	97.9±0.4	42.5±3.1	0.4±0.2
	$^{14}C$	38.69±0.3	49.7±5.7	1.3±0.1

**Table 4.5:** Difference between the total cross section predicted with MC Fluka simulation ( $\sigma_{gene}$ ) and the reconstructed value ( $\sigma_{reco}$ ) for all carbon isotopes ( $^9C$ ,  $^{10}C$ ,  $^{11}C$ ,  $^{12}C$ ,  $^{13}C$ ,  $^{14}C$ ) generated by a 200 MeV/u  $^{16}O$  beam impinging on  $C_2H_4$  target.

Beam energy	Fragment	Target : C		
		$\sigma_{gene}$ [mbarn]	$\sigma_{reco}$ [mbarn]	$\frac{\sigma_{reco}}{\sigma_{gene}}$
200 MeV	$^9C$	0.9±0.02	0.7±0.1	0.7±0.3
	$^{10}C$	3.8±0.04	1.6±0.1	0.4±0.2
	$^{11}C$	24.1±0.1	22.0±0.7	0.9±0.04
	$^{12}C$	36.3±0.1	27.4±0.8	0.8±0.04
	$^{13}C$	25.3±0.1	18.8±0.6	0.7±0.1
	$^{14}C$	8.1±0.1	7.3±0.4	0.9±0.1
700 MeV	$^9C$	1.3±0.02	–	–
	$^{10}C$	4.2±0.04	1.4±0.3	0.3±0.6
	$^{11}C$	20.5±0.1	18.6±1.7	0.9±0.1
	$^{12}C$	31.5±0.1	25.8±2.0	0.8±0.1
	$^{13}C$	23.2±0.1	14.3±1.4	0.6±0.2
	$^{14}C$	8.5±0.1%	2.2±0.4	0.3±0.7

**Table 4.6:** Difference between the total cross section predicted with MC Fluka simulation ( $\sigma_{gene}$ ) and the reconstructed value ( $\sigma_{reco}$ ) for all carbon isotopes ( $^9C$ ,  $^{10}C$ ,  $^{11}C$ ,  $^{12}C$ ,  $^{13}C$ ,  $^{14}C$ ) generated by a 200 MeV/u  $^{16}O$  beam impinging on C target.

Beam energy	Fragment	Target : H		
		$\sigma_{MC}$ [mbarn]	$\sigma_{reco}$ [mbarn]	$\frac{\sigma_{reco}}{\sigma_{gene}}$
200 MeV	$^{12}C$	25.3±0.03%	23.1±3.3	0.9±0.2
700 MeV	$^{12}C$	21.2±0.03%	52.4±15.4	–

**Table 4.7:** Difference between the cross section predicted with MC Fluka simulation ( $\sigma_{gene}$ ) and the reconstructed value ( $\sigma_{reco}$ ) for  $^{12}C$  generated by a 200 MeV/u  $^{16}O$  beam impinging on  $H$  target.

## 4.5 Analysis of performances

A systematic study varying the resolution on TOF,  $p$  and  $E_{kin}$  has been performed in order to understand which detectors mostly affect the precision on the mass determination, that reflects in a different number of each isotopes and cross section reconstruction with respect to MC prediction, referred to as  $\sigma(A)$ ,  $\frac{N_{reco}}{N_{MC}}$  and  $\frac{\sigma_{f,reco}}{\sigma_{f,MC}}$  respectively. In fact, the mass number  $A$  retrieved through a  $\chi^2$  minimization procedure, as well as the number of each isotope events, depends on the resolutions achieved on the measurements of these three quantities. Their estimation thus affect also the cross section reconstruction, as explained in Sec. 4.4. In principle, the energy release  $\Delta E$  should be considered in the systematic study too, but due to the negligible value of the energy released in the plastic scintillator with respect to the one in the calorimeter it was not taken into account. All the results presented in this section refer to a MC simulation of 200 MeV/u  $^{16}O$  beam impinging on a polyethylene target, with the  $A$  determination obtained through a standard  $\chi^2$  minimization approach after the application of a  $\chi^2 < 5$  cut. The resolutions tested for TOF,  $p$  and  $E_{kin}$  are reported in Tab.4.8 and were chosen in a reasonable range, according to the evidence presented in Sec. 4.3. All the results of the systematic study referring to  $^{12}C$  are reported in Tab.4.9. The results for the other carbon isotopes fragments ( $^9C$ ,  $^{10}C$ ,  $^{11}C$ ,  $^{13}C$ ,  $^{14}C$ ) scale in the same way and are presented in Appendix 6. In order to facilitate the interpretation of the results, Figure 4.15 reports the dependence of  $\sigma(A)$ ,  $\frac{N_{reco}}{N_{MC}}$  and  $\frac{\sigma_{f,reco}}{\sigma_{f,MC}}$  separately from the TOF,  $p$  or  $E_{kin}$  resolution, keeping the other two fixed at the standard precision (respectively  $\sigma(TOF) \simeq 70$  ps,  $\sigma(p)/p \simeq 3.7\%$  and  $\sigma(E_{kin})/E_{kin} \simeq 1.5\%$ ). Some general remarks can be underlined:

- $\sigma(A)$  value spans between 2.1 and 4.0%;  $\sigma(A)$  strongly depends on the TOF resolutions, doubling its value when changing  $\sigma(TOF)$  from 40 ps to 90 ps; its dependence on the resolution of  $p$  and  $E_{kin}$  is weaker and quite similar, worsening by about 15% and 18% when varying the former between 2.5%

and 5% and the latter between 1% and 2.8%. At present, the detectors performances allow to identify the fragments mass with a resolution  $\sigma(A)$  of  $\sim 3\%$ .

- The number of events reconstructed as  $^{12}C$  globally depends on the resolution of the reconstructed quantities showing a globally good agreement with the MC prediction, but a general overestimation is under investigation.  $\sigma(\text{TOF})$  has the major impact, varying the overestimation of  $^{12}C$  fragments correctly identified from 1% to 12%. The impact of the resolution on  $p$  is the smallest one, worsening the overestimation from 4% to 9% when varying it between 2.5% and 5%, while the resolution on  $E_{kin}$  changes the overestimation from 6% to 11% while moving it between 1% and 2.8%. At present, the number of  $^{12}C$  reconstructed events overestimate the MC prediction of  $\sim 7\%$ .
- The cross section reconstruction for  $^{12}C$  fragment presents an agreement with the generated value inside 8%, with a global underestimation probably caused by a not yet understood factor in the efficiency determination. As for the other checks, it strongly depends on TOF resolution, while the dependence on  $p$  and  $E_{kin}$  resolutions is much weaker. Comparing the cross section behaviour with the one on the number of reconstructed fragments, it is clear that we are overestimating the efficiency by a constant factor that is now under investigation.

As a conclusion, as better the kinematical quantities are reconstructed, as lower is the difference with the expected results, forcing to obtain the better precision for each subdetectors. All the results of the studies on  $\sigma(A)$ ,  $\frac{N_{reco}}{N_{MC}}$  and  $\frac{\sigma_{f,reco}}{\sigma_{f,MC}}$  referred to  $^{12}C$  are also reported in Figure 4.16, where one of the three quantities TOF,  $p$  or  $E_{kin}$  is maintained constant at his standard value while the other two change.

$\sigma(\text{TOF})[\text{ps}]$	$\sigma(p)[\%]$	$\sigma(E_{kin})[\%]$
40	2.5	1.0
50	3.0	1.3
60	3.5	1.6
70	4.0	1.9
80	4.5	2.2
90	5.0	2.5

**Table 4.8:** Resolution values on TOF,  $p$  and  $E_{kin}$  used for the determination of the precision of the mass number  $A$ .

$\sigma(\text{TOF})[\text{ps}]$	$\frac{\sigma(p)}{p}[\%]$	$\frac{\sigma(E_{kin})}{E_{kin}}[\%]$	$\sigma(A)[\%]$	$\frac{N_{reco}}{N_{MC}}$	$\frac{\sigma_{f,reco}}{\sigma_{f,MC}}$	
40	3.7	1.5	$2.2 \pm 0.2$	$1.01 \pm 0.01$	$0.92 \pm 0.01$	
50			$2.5 \pm 0.3$	$1.01 \pm 0.01$	$0.93 \pm 0.01$	
60			$2.8 \pm 0.5$	$1.03 \pm 0.02$	$0.94 \pm 0.01$	
70			$3.2 \pm 1.5$	$1.07 \pm 0.03$	$0.95 \pm 0.01$	
80			$3.7 \pm 2.3$	$1.13 \pm 0.05$	$0.97 \pm 0.01$	
90			$4.0 \pm 3.9$	$1.12 \pm 0.09$	$0.94 \pm 0.01$	
70	2.5	1.5	$2.9 \pm 0.6$	$1.04 \pm 0.01$	$0.94 \pm 0.01$	
	3.0		$3.1 \pm 0.8$	$1.06 \pm 0.02$	$0.95 \pm 0.01$	
	3.5		$3.2 \pm 1.4$	$1.06 \pm 0.03$	$0.95 \pm 0.01$	
	4.0		$3.3 \pm 1.6$	$1.08 \pm 0.03$	$0.96 \pm 0.01$	
	4.5		$3.4 \pm 1.7$	$1.09 \pm 0.04$	$0.96 \pm 0.01$	
70	5.0	1.5	$3.4 \pm 1.8$	$1.09 \pm 0.04$	$0.97 \pm 0.01$	
	3.7		1.0	$3.1 \pm 0.3$	$1.06 \pm 0.01$	$0.94 \pm 0.01$
			1.3	$3.2 \pm 1.4$	$1.06 \pm 0.03$	$0.94 \pm 0.01$
			1.6	$3.3 \pm 1.5$	$1.08 \pm 0.03$	$0.96 \pm 0.01$
			1.9	$3.4 \pm 1.7$	$1.09 \pm 0.04$	$0.96 \pm 0.01$
2.2		$3.4 \pm 1.9$	$1.09 \pm 0.04$	$0.96 \pm 0.01$		
70	3.7	2.5	$3.5 \pm 2.0$	$1.11 \pm 0.05$	$0.96 \pm 0.01$	

**Table 4.9:** Variation of  $\sigma(A)$ ,  $\frac{N_{reco}}{N_{MC}}$  and  $\frac{\sigma_{f,reco}}{\sigma_{f,MC}}$  as a function of the resolutions on TOF,  $p$  or  $E_{kin}$ , keeping the other two variables fixed at the standard precision (respectively  $\sigma(\text{TOF})=70$  ps,  $\sigma(p)/p=3.7\%$ ,  $\sigma(E_{kin})/E_{kin}=1.5\%$ ), for  $^{12}\text{C}$  fragment generated by a 200 MeV/u  $^{16}\text{O}$  beam impinging on a  $\text{C}_2\text{H}_4$  target, as obtained with the  $\chi^2$  method approach after the application of a  $\chi^2 < 5$  cut.

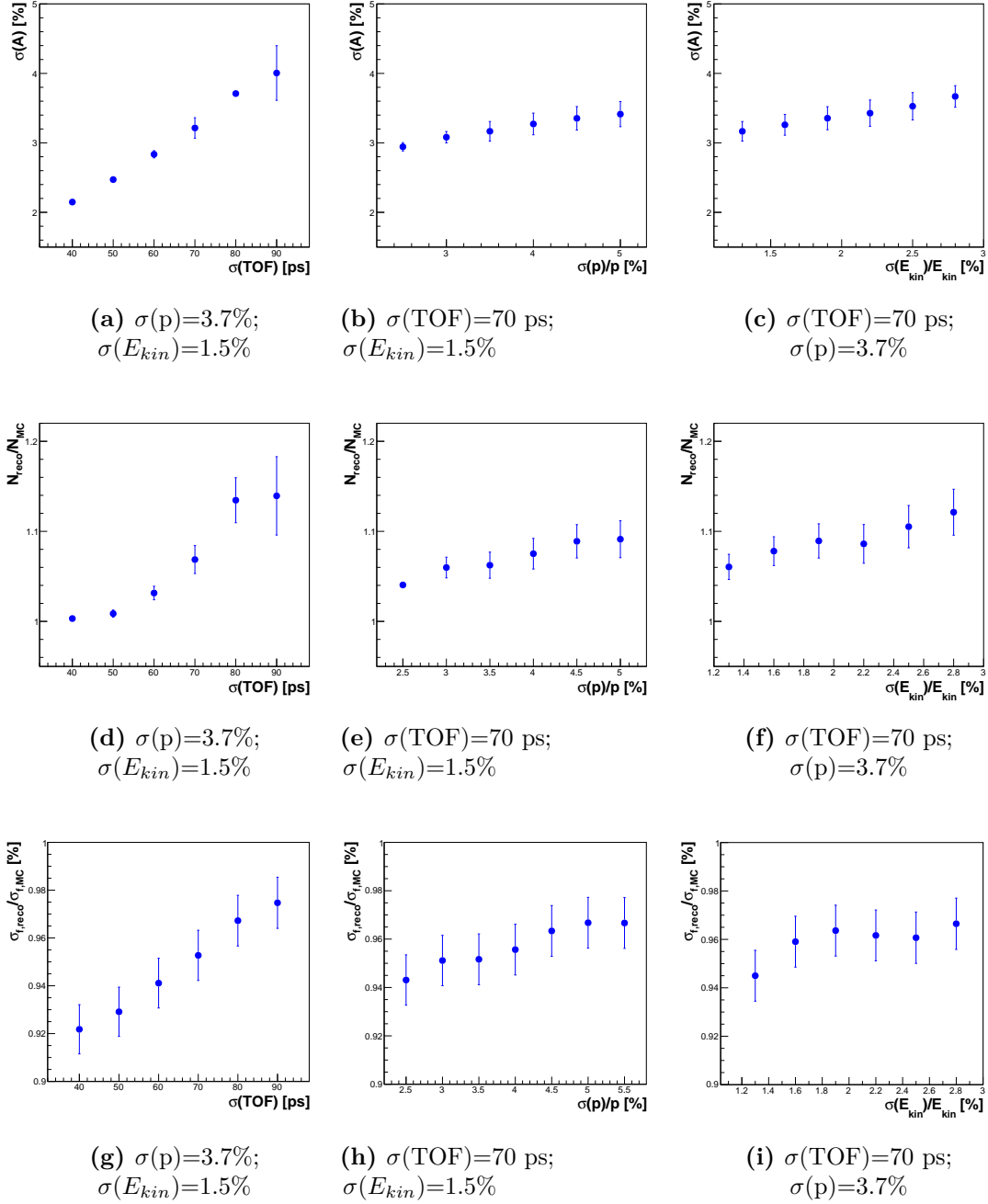


**Figure 4.15:** Percentage precision on the determination of the mass number  $A$  for the  $^{12}\text{C}$  fragment as obtained with the  $\chi^2$  method approach after the application of a  $\chi^2 < 5$  cut. The plots show the dependence of (a)  $\sigma(A)$  as a function of  $\sigma(\text{TOF})$  (with  $\sigma(p)=3.7\%$  and  $\sigma(E_{kin})=1.5\%$ ); (b)  $\sigma(p)$  (with  $\sigma(\text{TOF})=70$  ps and  $\sigma(E_{kin})=1.5\%$ ); (c)  $\sigma(E_{kin})$  (with  $\sigma(\text{TOF})=70$  ps and  $\sigma(p)=3.7\%$ ).

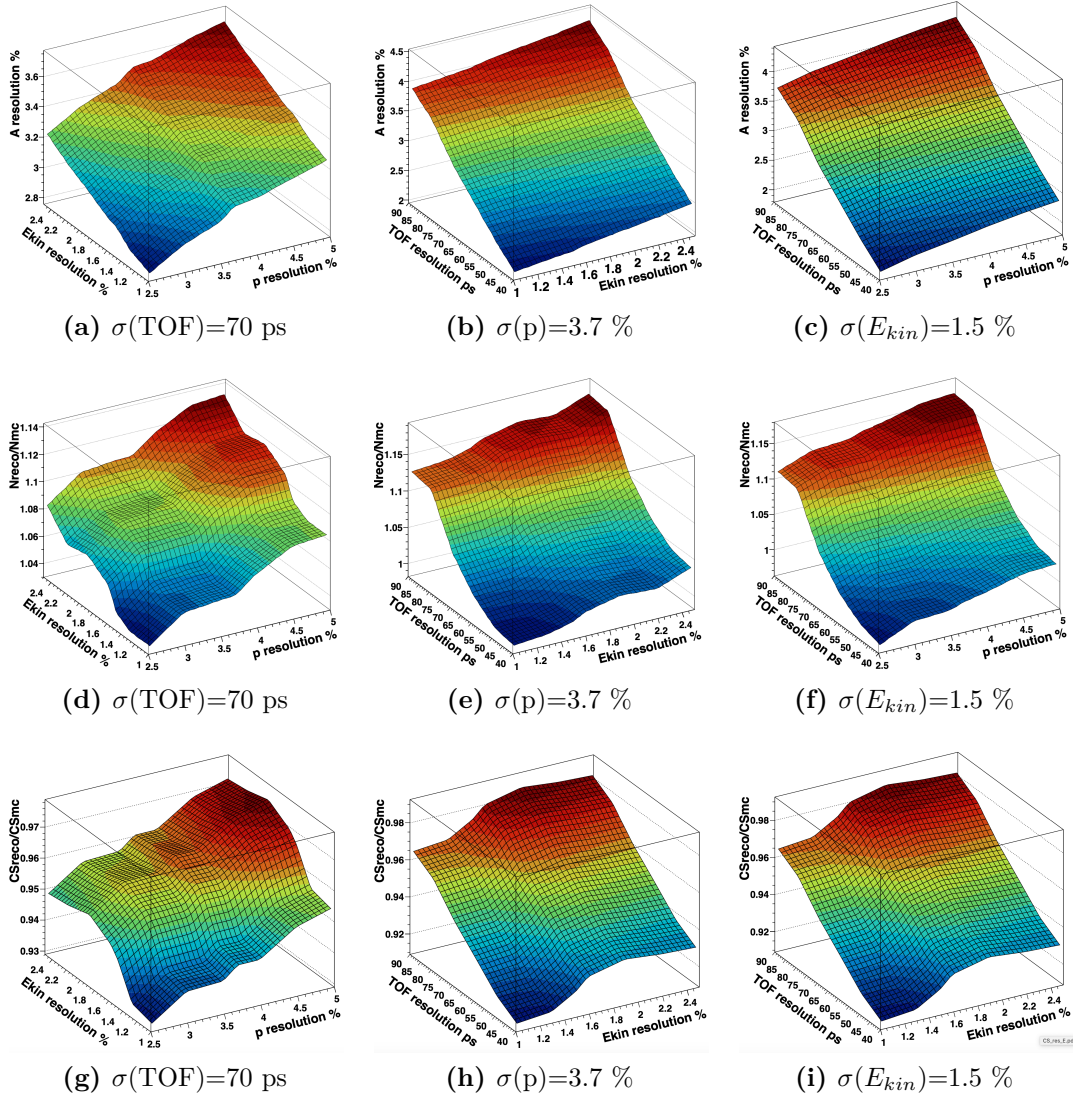


**Figure 4.16:** Percentage precision on the determination of the mass number  $A$  for the  $^{12}\text{C}$  fragment as obtained with the  $\chi^2$  method approach after the application of a  $\chi^2 < 5$  cut. Plot (a) refers to the  $A$  resolution as a function of  $\sigma(p)$  (X axis) and  $\sigma(E_{kin})$  (Y axis) accuracies when  $\sigma(\text{TOF})=70$ ps; plot (b) refers to the  $A$  resolution as a function of  $\sigma(E_{kin})$  (X axis) and  $\sigma(\text{TOF})$  (Y axis) accuracies when  $\sigma(p)=3.7\%$ ; plot (c) refers to the  $A$  resolution as a function of  $\sigma(p)$  (X axis) and  $\sigma(\text{TOF})$  (Y axis) accuracies when  $\sigma(E_{kin})=2.5\%$ ;



# Chapter 5

## FOOT real data analysis

A component of primary importance in the FOOT electronic setup is the  $\Delta E$ -TOF system, which is composed of the start counter (STC) and the scintillator (SCN) detectors, presented in details in Sec. 2.2.3. Summarizing the relevant features of such detectors, the STC is a 250  $\mu\text{m}$  thin plastic scintillator with a 5 cm transverse size, while the SCN is made of 40 bars of plastic scintillator arranged in two orthogonal layers of 20 bars each. A single bar has an active area of 44 x 2  $\text{cm}^2$  and a thickness of 3 mm. The system aims at measuring energy loss and TOF of the fragments generated in the target in order to characterize their charge and velocity. The STC provides the start time for the TOF measurements and the SCN provides the stop time and energy loss of the fragments passing through the detector. Particle charge discrimination can be achieved by correlating the energy loss in the SCN with the measured TOF value. This chapter refers to the analysis of data acquired during two data taking runs performed at CNAO in March 2019 with protons and  $^{12}\text{C}$  beams and at GSI in April 2019 with  $^{16}\text{O}$  beams in the energy range relevant for particle therapy, from 60 to 400 MeV/u. Details about the experimental setup and data samples collected are presented in Sec. 5.1. The SCN calibration procedure reported in Sec. 5.2 is then applied in Sec. 5.3 for the charge discrimination.

### 5.1 Data samples

Data acquisition at CNAO (in the following referred to also as "CNAO data") aimed to perform a set of detector calibration runs with protons and  $^{12}\text{C}$  ions, while in the one at GSI (in the following referred to also as "GSI data") more data for the detector calibration with  $^{16}\text{O}$  ions were collected and the first FOOT data taking with a carbon target aimed to perform the charge separation of fragments. Details about beams and energies employed in the two tests are reported in Tab. 5.1.

	Particle	Beam energy	Purpose	Target
CNAO	p	60 MeV/u	Calibration	–
	$^{12}\text{C}$	115 MeV/u		–
	$^{12}\text{C}$	240 MeV/u		–
	$^{12}\text{C}$	406 MeV/u		–
GSI	$^{16}\text{O}$	400 MeV/u	Calibration	–
	$^{16}\text{O}$	400 MeV/u	Fragmentation	C

**Table 5.1:** Summary of the data samples collected at CNAO and GSI test beams and analyzed in this chapter.

At the CNAO test beam, the distance between STC and SCN was 42.5 cm. By moving the SCN in the X-Y plane while keeping the beam line fixed on the Z axis, as shown in Figure 5.1 (a), the distance between the two detectors was always constant along the beam axis. Events were recorded when at least one bar in each of the two SCN layers was triggered. For an ideal calibration, the detector should have been irradiated in each of the 400 positions with each different beam. However, due to time constraints, the SCN was only partly irradiated in a cross pattern, ensuring at least an irradiation at the center of each bar, as represented in Figure 5.1 (b). A total of 5000 events was acquired for each SCN *hit position*, which is defined as the region where two bars of different layers overlap.

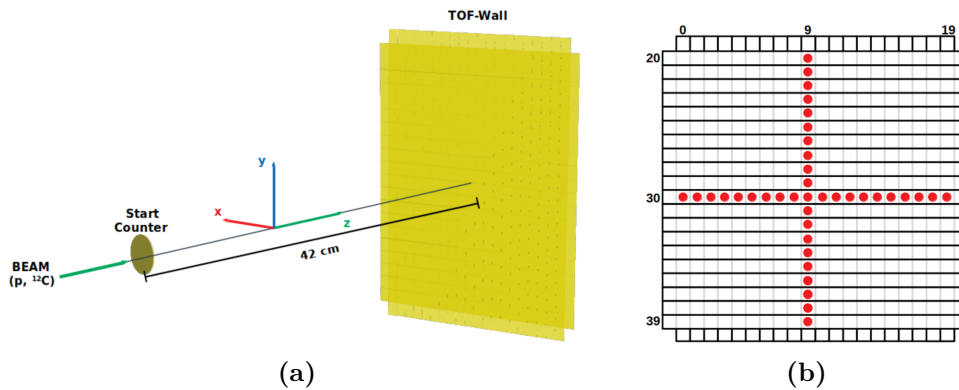


**Figure 5.1:** (a) Schematic view of CNAO experimental setup schematic view; (b) Schematic view of the SCN showing the bar labels and the cross pattern irradiated (red dots) during the calibration runs at CNAO [88].

The experimental setup used for the GSI test beam includes also part of the FOOT electronic setup: the pre-target region (Sec. 2.2.3), the vertex detector (Sec. 2.2.3) and a single calorimeter (Sec. 2.2.3) module. STC and SCN were placed at a distance of 2.23 m, which was kept fix during the irradiation, while moving the SCN along the X-Y plane, as in the CNAO test beam. A total of  $\sim 6.8 \cdot 10^4$  events

were collected in the calibration runs, irradiating only a limited number of bars mostly placed in central positions due to time constraints.

In conclusion, a total of 28 and 23 slabs have been calibrated during CNAO and GSI test beams, respectively. The bar calibrated in both occasions are 13 (specifically, slab number 9, 17, 18, 28, 29, 30, 31, 32, 33, 34, 36, 37, 38 referring to notation reported in Figure 5.1(b) ).

Finally, a total of  $\sim 4.5 \cdot 10^4$  events were acquired with a 5 mm graphite target ( $\rho=1.83 \text{ g/cm}^3$ ), in order to perform preliminary fragmentation studies. A schematic lateral view, as well as a picture of the actual setup, are presented in Figure 5.2.

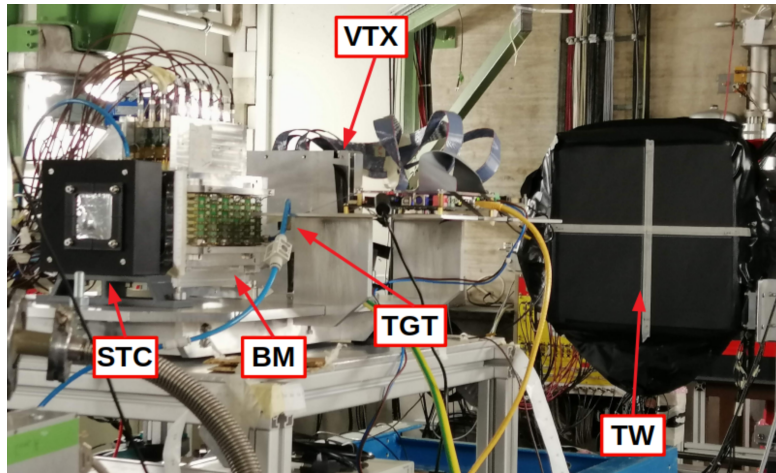
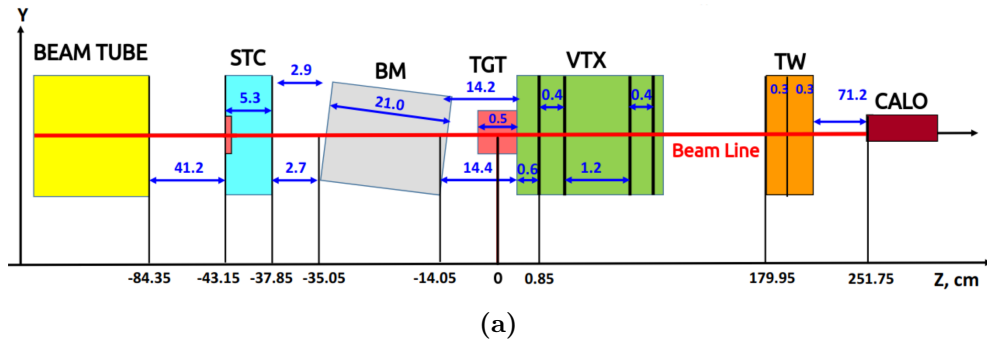


**Figure 5.2:** Schematic view (a) and picture (b) of the GSI setup. The pictures also show the target (TGT), as well as other part of the FOOT electronic setup present in the beam test (the STC, BM, VTX and CALO (i.e., a calorimeter module). The BM was tilted to avoid the possibility of having some lines of flight covered by its wires.

## 5.2 Energy calibration

A energy calibration of the SCN detector is required to determine the energy loss. The rationale driving such calibration is to find a correlation between the charge quantity collected from the SCN and the expected energy loss value predicted by MC. Details about the MC simulation performed to provide the set of reference  $\Delta E$  values can be found in [88]. For each bar involved in the event, two channels processed separately provide the charge collected in the left and right channel of the bar, in the following referred to as  $Q_L$  and  $Q_R$  respectively. Ideally,  $Q$  is expected to be independent of the hit position of the incident particle, which translates into an expected exponential attenuation of  $Q_L$  and  $Q_R$  along the bar moving from the hit position towards the respective bar side [55]. However, differences up to 15% were observed for the same incident beam, due to the obvious different behaviour of left and right channels of each bar [88]. Thus, the two charge signals can be combined to retrieve the total charge  $Q$  as:

$$Q = \sqrt{Q_R \cdot Q_L} \quad (5.1)$$

Only if both channels of a bar detect a signal during an event, the event is marked as *hit* and thus the total charge  $Q$  is collected, while it is automatically set to 0 if at least one of the channel is marked as empty. The precision obtained on the charge  $Q$  estimated with equation 5.1 is evaluated by applying a Gaussian fit to the charge distribution, as reported in Figure 5.4 for slab number 9, and it results to be  $\sim 5\%$ . In order to convert the charge evaluated with Eq. 5.1 into a energy loss  $\Delta E$  of the particle in the corresponding SCN bar, the mean value  $Q_{i,l}$  of the collected charge  $Q$  over all events in position  $i$  of layer  $l$  (where  $l = F$  for the front and  $l = R$  for the rear layer) is plotted as a function of the relative mean energy loss provided by MC simulation, in the following referred to as  $\Delta E_{i,l}$ , and then fitted with Birks' model [89] as follows:

$$Q_{i,l} = \frac{p_a \cdot \Delta E_{i,l}}{1 + p_b \cdot \Delta E_{i,l}} \quad (5.2)$$

$p_a$  and  $p_b$  represent the charge conversion factor and the saturation parameter of the model, respectively.

It should be noted that the SCN was disassembled for transport and subsequently rebuilt partly with different cables between CNAO and GSI data taking. Thus, the detector calibration has been performed both with data collected at CNAO taken alone and by combining CNAO and GSI calibration samples. The energy calibration curve obtained for a position at the center of bar 30 (i.e. when also bar 9 had been hit, as displayed in red dots in Figure 5.1(b)) is showed in Figure 5.3, proving that the Birks' model expressed in Eq. 5.2 accurately reproduce the light output of the bar. In particular, the energy calibration performed with only

CNAO data suits very well the calibration point obtained with GSI ones. The calibration parameters  $p_a$  and  $p_b$  retrieved through this method for each irradiated bar are presented in Tab. 5.2. The first three columns concern the Birk's law fit applied only to the four beam energy points collected at CNAO, while the last three refer to the fit performed on all the available energy points (i.e. five points, four collected at CNAO and one at GSI, see Tab.5.1 ). The comparison of the results on the 13 bars calibrated in both CNAO and GSI test beams prove that the calibration performed with proton and carbon ions can be confidently extended to oxygen ions too.

Bar label	CNAO sample			CNAO + GSI sample		
	$p_a$	$p_b \cdot 10^2$	$\chi^2$	$p_a$	$p_b \cdot 10^2$	$\chi^2$
1	$1.99 \pm 0.15$	$1.15 \pm 0.21$	2.6			
2	$2.12 \pm 0.15$	$1.15 \pm 0.20$	0.6			
3	$1.89 \pm 0.16$	$1.08 \pm 0.26$	0.3			
4	$2.28 \pm 0.15$	$1.18 \pm 0.19$	0.5			
5	$2.26 \pm 0.15$	$1.19 \pm 0.19$	0.5			
6	$2.13 \pm 0.15$	$1.18 \pm 0.19$	0.5			
7	$2.02 \pm 0.14$	$1.20 \pm 0.20$	0.4			
9	$2.07 \pm 0.16$	$1.19 \pm 0.24$	0.3	$2.07 \pm 0.16$	$1.19 \pm 0.24$	0.3
17	$1.94 \pm 0.13$	$1.22 \pm 0.21$	0.6	$1.92 \pm 0.14$	$1.26 \pm 0.21$	4.1
18	$1.88 \pm 0.13$	$1.22 \pm 0.20$	0.8	$1.86 \pm 0.13$	$1.23 \pm 0.20$	4.4
20	$2.28 \pm 0.15$	$1.40 \pm 0.19$	0.9			
21	$2.20 \pm 0.15$	$1.29 \pm 0.22$	1.2			
22	$2.39 \pm 0.16$	$1.27 \pm 0.22$	0.7			
23	$2.15 \pm 0.15$	$1.23 \pm 0.21$	0.6			
24	$2.32 \pm 0.27$	$1.44 \pm 0.37$	0.6			
25	$1.69 \pm 0.12$	$1.16 \pm 0.22$	0.2			
26	$2.20 \pm 0.16$	$1.21 \pm 0.22$	0.2			
27	$2.27 \pm 0.16$	$1.20 \pm 0.21$	0.2			
28	$2.21 \pm 0.16$	$1.21 \pm 0.21$	0.2	$2.21 \pm 0.16$	$1.21 \pm 0.21$	0.2
29	$2.06 \pm 0.17$	$1.14 \pm 0.25$	0.1	$2.06 \pm 0.17$	$1.30 \pm 0.24$	0.8
30	$2.18 \pm 0.17$	$1.29 \pm 0.23$	0.3	$2.18 \pm 0.17$	$1.30 \pm 0.24$	0.8
31	$2.12 \pm 0.17$	$1.25 \pm 0.24$	0.1	$2.12 \pm 0.17$	$1.27 \pm 0.24$	0.4
32	$2.30 \pm 0.17$	$1.19 \pm 0.21$	0.3	$2.30 \pm 0.17$	$1.20 \pm 0.22$	0.4
33	$1.91 \pm 0.14$	$1.16 \pm 0.21$	0.3	$1.91 \pm 0.15$	$1.17 \pm 0.21$	0.4
34	$2.30 \pm 0.20$	$1.43 \pm 0.32$	1.1	$2.34 \pm 0.20$	$1.59 \pm 0.32$	2.9
36	$1.92 \pm 0.14$	$1.08 \pm 0.21$	0.6	$1.90 \pm 0.15$	$1.13 \pm 0.22$	5.9
37	$1.99 \pm 0.15$	$1.19 \pm 0.23$	0.5	$1.98 \pm 0.16$	$1.28 \pm 0.24$	8.2
38	$2.21 \pm 0.17$	$1.27 \pm 0.24$	0.8	$2.20 \pm 0.17$	$1.34 \pm 0.25$	6.8

**Table 5.2:** Birks' parameters  $p_a$  and  $p_b$  for each SCN bar retrieved by fitting the experimental points collected only during calibration runs at CNAO and both at CNAO and GSI calibration runs. Parameter values and related uncertainties are reported with the same number of digits implemented in the analysis.

By inverting Eq.5.2, the actual energy loss value of each event in a given position  $i$  and layer  $l$  can be evaluated as follow:

$$\Delta E_{i,l} = \frac{Q_{i,l}}{p_{0,i,l} - p_{1,i,l} \cdot Q_{i,l}} \quad (5.3)$$

Finally, the corresponding calibrated energy loss of the particle is defined as the sum of the energy loss in the two layers of SCN, as:

$$\Delta E_i = \Delta E_{i,F} + \Delta E_{i,R} \quad (5.4)$$

In order to assure a reliable fit, the presented calibration procedure was applied only to the SCN bars which collected more than 100 events.

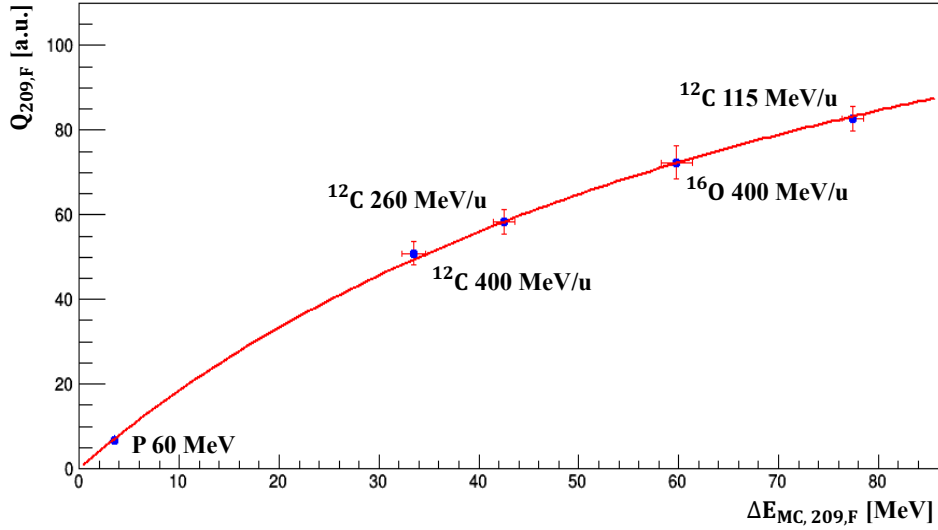


**Figure 5.3:** Energy calibration curve obtained with the Birks' model (red line) for the central position ( $i=209$ ) of bar 30 of the front layer ( $l=F$ ) of the SCN detector. The points are labeled using the corresponding particle and beam energy. Error bars represent the standard error on the mean obtained from the Gaussian fit.

Tab.5.3 reports the numerical comparison of the mean energy release in the SCN predicted through MC simulations and the one obtained as mean value of the Gaussian fit applied to distributions calibrated with the method presented above.

Results prove that the chosen calibration procedure is quite accurate in modeling carbon and oxygen ions. In fact, referring to the front layer, the calibration method explained reconstructs the energy release with an accuracy below 4%, with a slightly larger discrepancy for protons. Nevertheless, it should not be neglected that the electronic setup of FOOT is not designed to perform precise measurements for light particles ( $Z < 3$ ). Instead, the reconstruction accuracy on the energy release in the rear layer is always below 6%.

<b>Front layer</b>				
Beam	Energy [MeV/u]	$\Delta E_{MC}$ [MeV]	$\Delta E_{Calib}$ [MeV]	Diff [%]
p	60	$3.4 \pm 0.2$	$3.1 \pm 0.2$	7.7
$^{12}C$	115	$74.1 \pm 1.1$	$71.0 \pm 1.2$	4.0
$^{12}C$	260	$42.2 \pm 1.1$	$42.2 \pm 1.3$	0.02
$^{12}C$	400	$33.4 \pm 1.2$	$34.8 \pm 1.0$	4.2
$^{16}O$	400	$59.5 \pm 1.6$	$57.7 \pm 6.2$	3.0
<b>Rear layer</b>				
Beam	Energy [MeV/u]	$\Delta E_{MC}$ [MeV]	$\Delta E_{Calib}$ [MeV]	Diff [%]
p	60	$3.5 \pm 0.2$	$3.4 \pm 0.2$	4.2
$^{12}C$	115	$77.4 \pm 1.1$	$76.5 \pm 1.2$	1.2
$^{12}C$	260	$42.5 \pm 1.1$	$42.4 \pm 1.3$	0.2
$^{12}C$	400	$33.5 \pm 1.2$	$35.4 \pm 1.4$	5.7
$^{16}O$	400	$59.8 \pm 1.6$	$56.8 \pm 5.8$	5.0

**Table 5.3:** Energy release in the SCN detector predicted with MC simulation ( $\Delta E_{MC}$ ) and mean value obtained from Gaussian fits of the calibrated energy distributions ( $\Delta E_{calib}$ ). The results are given separately for each SCN layer.

### 5.3 Charge reconstruction of fragments

Once the calibrated  $\Delta E$  (Eq. 5.4) is available, the charge  $Z_i$  of a particle impinging on the SCN in position  $i$  is evaluated by inverting the Bethe-Bloch formula (Eq. 1.1), as follows:

$$Z_i = \sqrt{\frac{\Delta E_i \beta^2 A_S}{\rho \delta x K Z_S} \left( \frac{1}{2} \log \frac{2m_e c^2 \beta^2 \gamma^2 W_{max}}{I^2} - \beta^2 \right)^{-1}} \quad (5.5)$$

where  $\beta = \frac{d}{c \cdot TOF_i}$ ,  $d$  is the distance traveled by the particle and  $\delta x$  is the thickness of the two SCN layers ( $\delta x = 6$  mm).

$TOF_i$  represents the TOF of a particle impinging the SCN detector in position  $i$ . In particular, the TOF value calculated for each bar combines the start time  $T_{STC}$

of each event extracted from the STC detector and the corresponding stop time obtained from the SCN signals. For this purpose, the right and left channels of each SCN bar involved in the event, referred to as  $T_L$  and  $T_R$  respectively, were processed separately and the raw stop time associated to each bar was extracted as follow:

$$T_{bar} = \frac{T_L + T_R}{2} \quad (5.6)$$

Then, the raw TOF value was calculated for each bar as:

$$TOF_{raw} = T_{bar} - T_{STC} \quad (5.7)$$

Relating the raw TOF value from Eq. 5.7 to the expected TOF value between the STC and SCN predicted from MC simulation, an offset parameter for each position  $i$  and layer  $l$ , referred to as  $a_{i,l}$ , is retrieved.  $a_{i,l}$  accounts all the possible time offsets, such as signal propagation through cables and global time shifts between the STC and SCN detectors. Once this parameter has been extracted, the TOF of each event in a given position  $i$  and layer  $l$  is evaluated as:

$$TOF_{i,l} = TOF_{raw,i,l} - a_{i,l} \quad (5.8)$$

However, when referring to a calibration run, the calibrated TOF value of fragments should be evaluated from the center of the target, where the fragments are most likely produced, to the SCN, rather than from STC and SCN. Thus, for the fragmentation run the TOF of produced fragments is calculated as follow:

$$TOF_{i,l} = TOF_{raw,i,l} - a_{i,l} - TOF'_{STC-Target} \quad (5.9)$$

where  $TOF'_{ST-Target}$  is an additional offset accounting for the time needed by the primary beam ions (i.e.,  $^{16}O$  ions in the fragmentation run collected at GSI test beam) to travel from the STC to the target center. The precision on the TOF evaluation can be estimated by applying a Gaussian fit to the TOF distributions of each bar and it is  $\sim 90ps$ . An example is reported in Figure 5.4 (b) TOF reconstructed in slab number 9 by applying Eq. 5.9 to slab number 9 when it is crossed by a 400 MeV/u oxygen beam during the calibration run performed at GSI. Finally, for all the positions  $i$  that were well-calibrated in terms of energy as explained in Sec. 5.2, the TOF of a particle impinging the SCN detector in position  $i$  was defined as the mean value between its value in the front and rear layers:

$$TOF_i = \frac{TOF_{i,F} + TOF_{i,R}}{2} \quad (5.10)$$

Eq.5.5 was applied to discriminate the charge of fragments produced in nuclear interactions of a 400 MeV/u  $^{16}O$  beam impinging on a 5 mm graphite target during

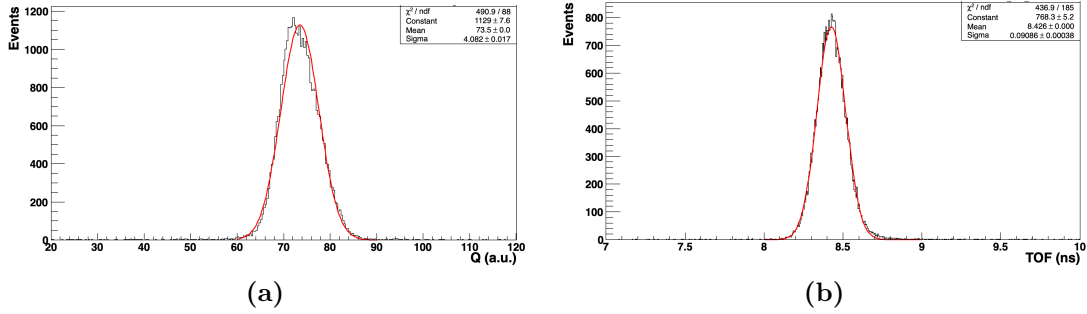


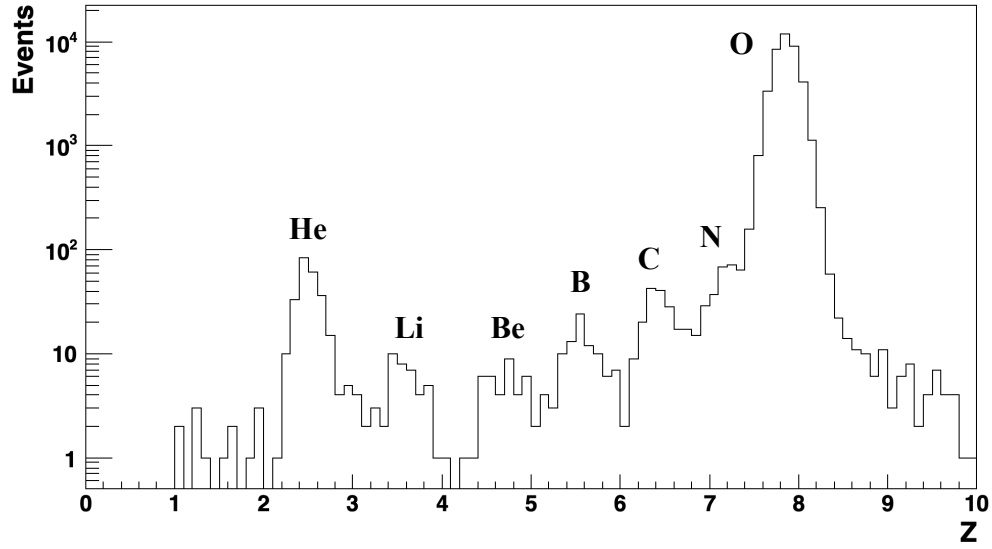
**Figure 5.4:** (a) Distribution of charge  $Q$  evaluated with Eq. 5.1 (black line) and (b) TOF reconstruction with Eq.5.9 (red line). The precision on both quantities is estimated by applying a Gaussian fit (red lines).  $Q$  and TOF precision are about 5% and 90 ps, respectively. Both figures refer to the signals collected by slab number 9 (see Figure 5.1(b)) to the calibration run performed at GSI with a 400 MeV/u  $^{16}\text{O}$  beam and no target.

the data taking performed at GSI. Specifically, the equation was applied to each event occurring in a SCN position that was well-calibrated as explained in the previous section (Sec. 5.2) and that was marked as a *real combination* event. In fact, a selection based on the charge and time signals measured by the SCN layers is applied in order to ensure that two events recorded in the front and back layers actually correspond to the same particle. In particular, the time to travel from the front to the rear layer must be below 10% the average time measured by the two layers and the difference of the charges measured by two layers must be below 20% the average charge evaluated by the layers. Figures 5.5 (a) and (b) refer to the charge identification based on the calibration curve retrieved with data collected only in the calibration run performed at CNAO and by combining CNAO and GSI calibration sample, respectively. Different charged fragments can be well discriminated in the plots and a Gaussian fit can be applied to the peaks to get an approximate estimation of the charge values and the corresponding uncertainties. The huge peak on the oxygen position refers to the events where the beam did not interact with the target. Results are reported in Tab.5.4, together with the differences with respect to the expected charge value. Both spectra do not contain any hydrogen particles because of the experimental threshold chosen in SCN signals to discriminate the electronic noise, which also cuts the events below a certain charge. A general improvement when considering the calibration provided by both CNAO and GSI calibration runs is observed. The results are satisfactory and will be improved with a high statistics campaign of calibration with different beam at several energies, even if they should be considered as preliminary, due to the very low statistics of events correctly reconstructed during GSI fragmentation run

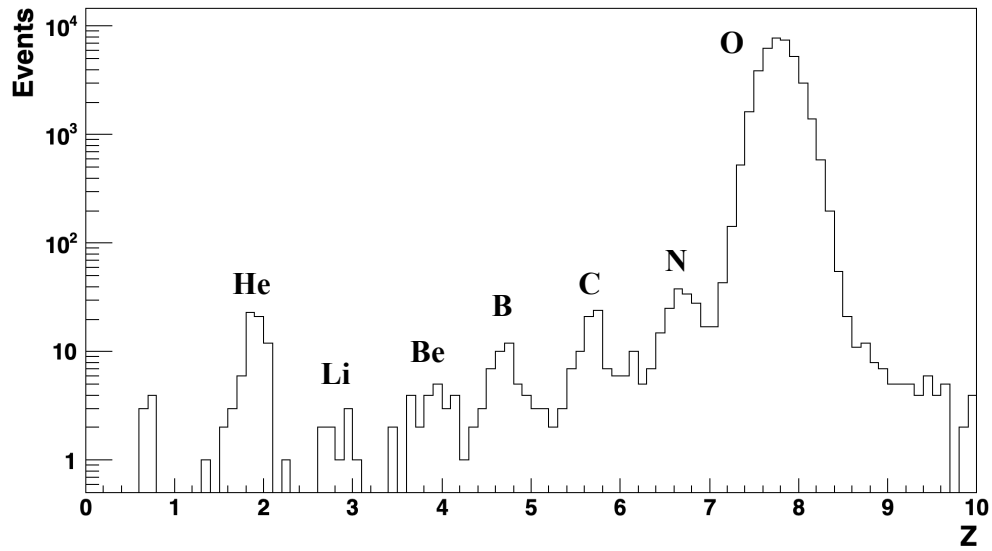
( $\sim 4.3 \cdot 10^3$  events). Surely, they will be improved with a high statistics campaign of calibration with different beam at several energies. Nevertheless, it should not be neglected that this is the first fragments' charge separation obtained with all the currently available elements of the FOOT electronic apparatus. Thus, the results are very encouraging for the future experimental studies of fragmentation that will be performed with more beam species and over a wider energy range in 2021. The tests will also be of great help to improve the calibration curve, up to now based on a simple Birks' model to fit charge collected only for three different particles type (protons, carbon and oxygen) in 13 slabs. Moreover, new beam tests will improve the statistics and help to study better the source of the underestimation in the reconstructed charge.

Particle	GSI calibration		GSI+CNAO calibration	
	Z	Diff [%]	Z	Diff [%]
H	–	–	–	–
He	$2.5 \pm 0.1$	25.5	$1.9 \pm 0.1$	-0.5
Li	$3.1 \pm 0.2$	1.9	$2.95 \pm 0.07$	-1.7
Be	$4.7 \pm 0.2$	15.3	$3.9 \pm 0.2$	-2.3
B	$5.6 \pm 0.2$	10.1	$4.7 \pm 0.2$	-5.7
C	$6.4 \pm 0.2$	6.7	$5.7 \pm 0.2$	-5.4
N	$7.3 \pm 0.2$	3.7	$6.7 \pm 0.2$	-4.0
O	$7.9 \pm 0.2$	-1.8	$7.8 \pm 0.2$	-2.7

**Table 5.4:** Preliminary charge evaluation obtained by applying Gaussian fits to the charge spectra of fragments produced in the interaction of a 400 MeV/u  $^{16}\text{O}$  beam with a graphite target. The second column refers the plot displayed in Figure 5.5(a), while the fourth one to Figure 5.5(b). Third and fifth columns represent the difference between the reconstructed charge value and the expected one.



(a) GSI calibration data samples



(b) CNAO + GSI calibration data sample

**Figure 5.5:** Charge spectra obtained from the fragmentation of 400 MeV/u  $^{16}\text{O}$  ions on a graphite target. The spectra was reconstructed through the energy calibration method presented in Sec.5.2 by considering only data collected in the calibration run performed at GSI (a) and by combining the ones recorded both in GSI and CNAO calibration runs (b).



## Chapter 6

# Future work: neutrons detection with FOOT

The discussion and analysis presented in Sec. 3.3.2 already highlights the important production of neutrons in thick materials relevant for space applications. The produced neutrons have a mean free path much longer than ions at the same kinetic energy and are generally associated to high RBE, thus representing a major factor to be taken into account in shielding design. Despite of that, the quality of a shielding material is generally evaluated in terms of dose attenuation, not including neutron production because of the very poor experimental database. Thus, the lack of measurements on the production of fast neutrons is generally acknowledged as a major gap for the estimation of the shielding configuration in spacecraft and planetary bases. The FOOT experimental setups extensively presented in Sec. 2.2 could be used for the identification and measurement of energetic neutrons, typically with energy exceeding 50 MeV, produced by the interactions of ions of energy close to 1 GeV/u. Considering the abundance of the different ion species in the GCR spectrum displayed in Figure 6.1, the most important cases of study would be  ${}^4\text{He}$  and higher  $Z$  ions like  ${}^{16}\text{O}$  at an energy of  $\sim 700$  MeV/n. Because the production of neutrons needs to be studied on target materials relevant for radioprotection in space, the first priorities should be aluminum, present in all spacecraft structure, and plastic material like polyethylene, generally considered an optimal shield for GCR. Layers of Moon Regolith and others made in-situ compound should be tested as well.

Neutrons production is a delicate element also in the hadrontherapy treatment. In the nuclear interaction between beam and human body, neutrons are produced in copious quantities: they span 10 orders of magnitude in neutron energy, their energy distributions depend strongly on the proton beam energy and direction, they are extremely penetrating, and their relative biologic effectiveness is as much

as about 20 times higher than that of proton radiation. Thus, they potentially increase the risk of radiogenic late effects and can create significant potential safety hazards [90].

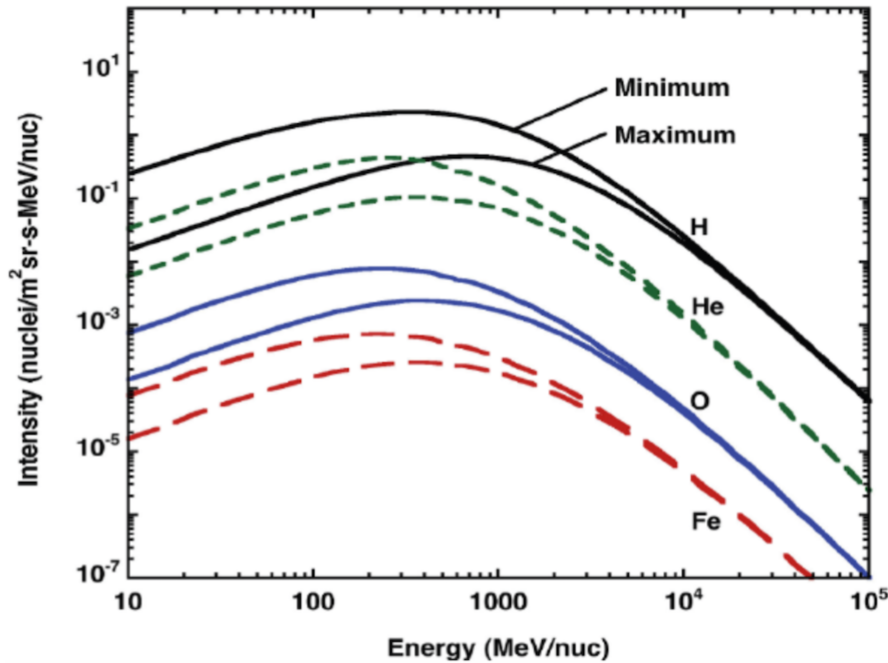


**Figure 6.1:** Spectrum of different components of the Galactic Cosmic Rays. *Maximum* and *minimum* refer to the sun’s activity, which runs on a roughly 11-year cycle, moving regularly from its most quiet period – solar minimum – to its most active – solar maximum – and back to quiet.

The updated apparatus containing dedicated part for neutron detection is argument of the next studies; it is currently under investigation the possibility to reveal neutrons with the present detector generating samples by Fluka MC code [91] of oxygen beam at different energies on a 2 mm polyethylene target to determine the neutron angular distribution produced in the interaction. Thus, both the electronic setup (described in Sec. 2.2.3) and the emulsion spectrometer (presented in Sec. 2.2.4) will be employed, in order to cover the full angular acceptance on the entire neutron energy range (50-2000MeV), as displayed in Figure 6.2. The angular semi-aperture of  $\sim 10$  deg of the magnetic spectrometer will provide information about the forward and most energetic neutron production, while the emulsion spectrometer will detect and measure neutrons emitted at large angles. The vertex detector in the magnetic spectrometer (see Sec. 2.2.3) will identify which energy depositions in the calorimeter match with charged tracks emerging from the target, to define the remaining depositions as possible candidates

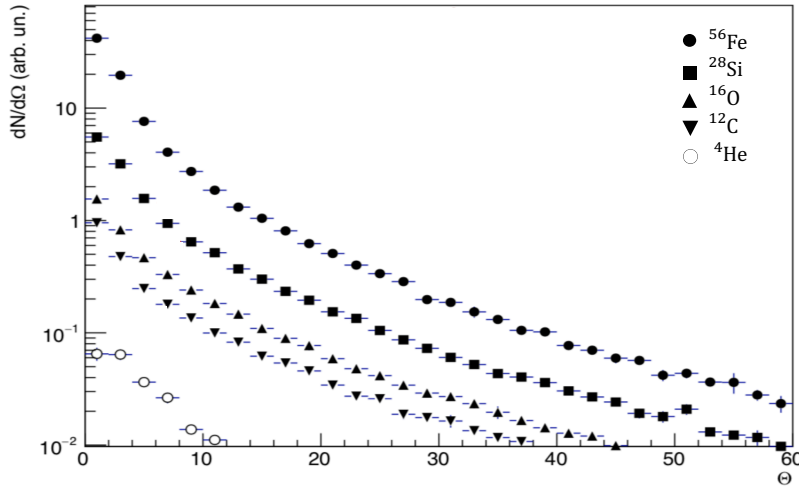
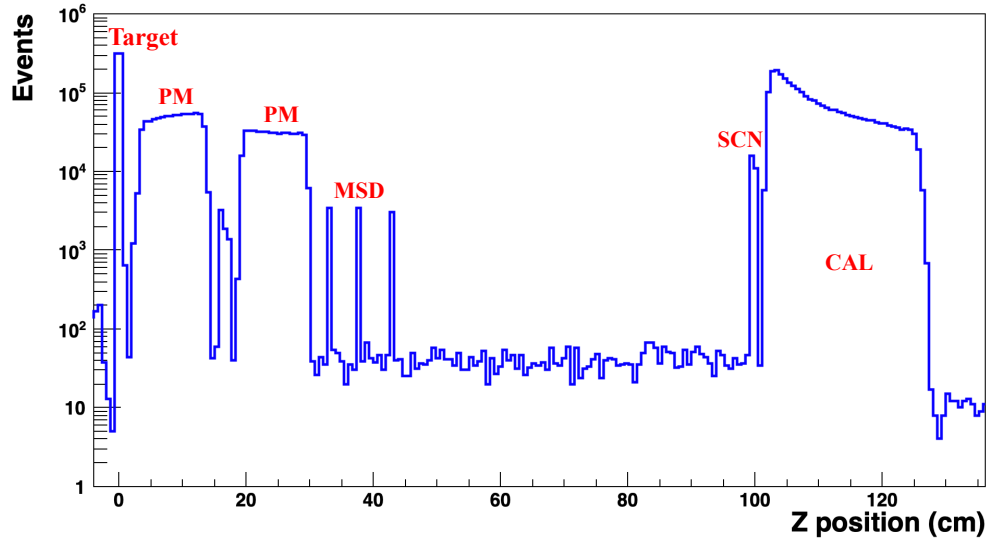


**Figure 6.2:** Expected polar angle distribution of neutrons with energy above 50 MeV produced by  $^{56}\text{Fe}$ ,  $^{28}\text{Si}$ ,  $^{16}\text{O}$ ,  $^{12}\text{C}$  and  $^4\text{He}$  at 800 MeV/u impinging on a 2 mm thick polyethylene target simulated by FLUKA MC code. Courtesy of G. Battistoni.

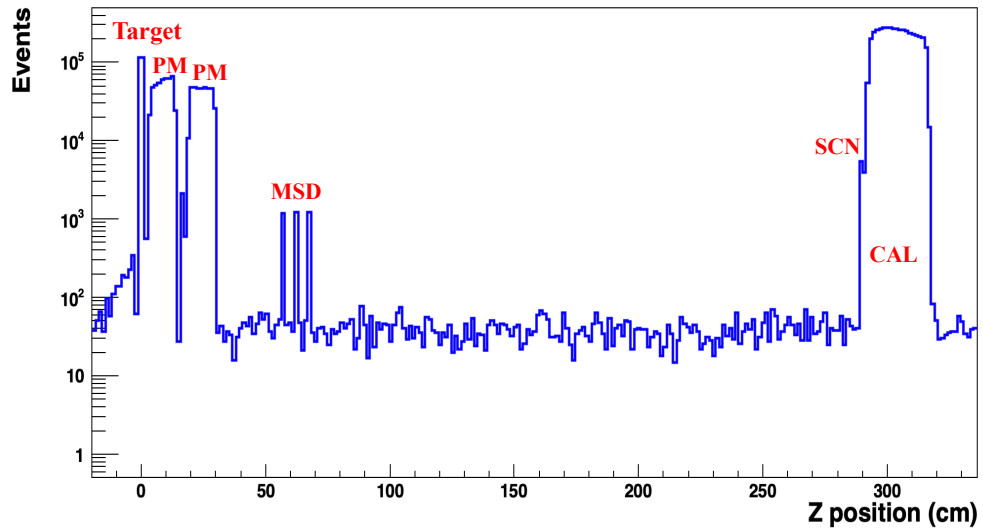
being produced by neutrons. Then, the scintillator and calorimeter detectors in the downstream region play the role of a telescope system  $\Delta E$ -E exploited for the characterization of secondary neutrons reported in Sec. 3.3.2, respectively. Charged particles will be characterized by an energy loss, i.e. a signal, both in the scintillator and calorimeter, while neutrons will interact only with the latter. To collect some preliminary considerations, the neutrons production for a 200 MeV/u ( $10^7$  primary particles) and 700 MeV/u ( $5 \cdot 10^6$  primary particles) oxygen beam impinging on a 5 mm polyethylene target has been investigated. The generation position along the beam axis of neutrons that reach the calorimeter is reported in Figure 6.3. For both cases at 200 MeV/u and 700 MeV/u, neutrons reaching the calorimeter are about 60% of the total neutrons produced. Nevertheless, the large production of neutrons in the FOOT setup instead that in the target (as highlight in red on the figures) could represent a source of misidentification. In particular, neutrons generated in the target are about  $\sim 12\%$  of the total amount that reach the calorimeter. In principle, background neutrons that comes from other sources than the target could be identified on their larger time of flight, due to both their lower energy and longer path before reaching the calorimeter. However, only neutrons from the target with an energy higher than the ones from background will have some sort of experimental signature to be identified. A dedicated study will be performed, in order to estimate the time resolution required in order to discriminate between the two components. Thus, a careful study of background neutrons has to be

performed, together with the evaluation of secondary fragmentation and consequent additional neutron production both in the elements of the apparatus and in air. Moreover, it will be of paramount importance to evaluate neutron efficiency of the calorimeter. Preliminary measurements will be carried out to perform a calibration campaign in order to assess both resolution and efficiency performances.

Preliminary measurements both using the current detector and with a prototype for the new one will be performed in parasitic mode to the next FOOT experimental tests foreseen in March and September 2021 at CNAO (Italy). The first campaign will be mainly focused on detectors calibration and trigger test, while the second one on physics measurements with the presence also of the magnet (see Sec. 2.2.3). During these tests beam it could be possible to repeat some measurements present in literature about neutron production in  $p+^{12}C$  and  $^{12}C+^{12}C$  reactions in order to provide the information about the feasibility of detecting neutrons with the present setup and with other detectors. In fact, several inorganic crystals and a liquid scintillating detector optimized for neutrons/ $\gamma$  discrimination will be placed at several angles (spanning between 30 deg and 80 deg) to get a raw estimation of the expected count rate, neutron energy spectrum and background via TOF measurement (see Sec. 3.2). Moreover, the additional shifts with oxygen beam assigned to FOOT at GSI in July 2021 will be another occasion to investigate the detector capability to identify neutrons. On this purpose, the study presented in Sec. 3.3.2 will provide important comparison results.



(a) 200 MeV/u



(b) 700 MeV/u

**Figure 6.3:** Neutrons production that reach the calorimeter as a function of the generation position along the beam axis for a 200 MeV/u (a) and 700 MeV/u (b)  $^{16}\text{O}$  beam impinging on a 5 mm thick  $\text{C}_2\text{H}_4$  target. The visible peaks and regions correspond to neutrons produced inside the target, the magnets (referred to as PM), the three MSD layers (referred to as MSD), the scintillator (referred to as SCN) and the calorimeter (referred to as CAL).



# Conclusions

The aim of the work discussed in this thesis is to improve the set of experimental data characterizing the complex radiation field generated by the interaction of medium-high energy beams (200 - 1000 MeV/u) with targets for applications in particle therapy and space radiation protection. Nuclear fragmentation processes can occur inside both the patient body or in a spaceship hull, generating secondary charged and neutral particles characterized by a broad energy spectrum.

The first part of this study focused on data collected in different experimental campaigns with a relatively simple setup common to a wide number of nuclear fragmentation experiments and described in Chapter 2. The combination of signals acquired by three scintillators placed in sequence allows the characterization of both secondary charged particles and neutrons. Specifically, two separate studies both presented in Chapter 3 have been conducted: the first one deals with the characterization of all secondary charged particles produced by a therapeutic carbon beam in a specific biological target; the second one is related to data collected in the frame of the ROSSINI project to study the secondary neutrons produced by a high energy nickel beam interacting with materials either of interest for the spaceship hull design or in-situ resources for building permanent habitats on the Moon or Mars.

Secondary particles produced from the nuclear interaction of a 400 MeV/u  $^{12}\text{C}$  beam with a  $9.095 \text{ g} \cdot \text{cm}^{-2}$  (i.e., 5 cm) compact-bone target was experimentally investigated and results show that the produced fragments are characterized by a wide spectrum of both kinetic energies and production angles. Specifically, the angular distributions indicate that while primary ions and fragments down to  $Z=3$  (i.e., boron, beryllium, lithium) are emitted in a rather narrow cone in the forward direction, helium and hydrogen fragments exhibit a wider angular spectrum. On the other hand, the most abundant species produced between 5 deg and 30 deg are hydrogen particles. The energy spectra show that, at small angles, the distributions peak at the residual primary beam energy ( $\sim 250 \text{ MeV/u} \pm 10\%$ ) and they become broader at increasing angle. Instead, light fragments can be produced with energies up to about twice the initial energy of carbon projectiles. Moreover, the peak energy decreases as the measurement angle increases.

Experimental data of 1000 MeV/u  $^{58}\text{Ni}$  beam interacting with several (i.e., 1 - 30 cm) shielding materials have been analyzed in order to characterize the secondary neutrons production. Polyethylene and aluminium target have been considered: the former is the reference shielding currently used in space, while the latter is the most common material used in the spacecraft structures. In addition, Moon and Mars regolith as well as Moon concrete have been used as in-situ simulants of interest in the space colonization phase foreseen in the next decades. The results show that most of the produced secondary neutrons produced at  $\sim 24$  deg are characterized by an energy distribution peaked at values ranging between 300 and 500 MeV. For a given material, the peak position shift towards lower energies as the target thickness increases. The data analysis identified aluminum as the material which produces the lowest neutron yield independently of the irradiated thicknesses. Concerning the exploration and new habitats design, the secondary neutrons production is almost the same in both Mars and Moon regolith targets. Instead, at the same thickness, Moon regolith generate a lower neutron yield compared to concrete.

With the same goal to measure nuclear fragmentation cross sections relevant in particle therapy and space radioprotection with a great accuracy, data simulated and acquired for the FOOT (FragmentatiON Of Target) experiment has been analyzed. FOOT relies on a more complex experimental setup described in details in Chapter 2. The work of this thesis focused on the the electronics apparatus, which aims to measure fragments heavier than helium emitted in a narrow cone ( $\sim 10$  deg) with respect to the primary beam direction. By measuring and combining momentum, time of flight, kinetic energy and energy loss in a thin scintillator detector, the FOOT setup is able to determine fragments charge and mass, as well as their energy and production angle. A dedicated software has been developed in order to automatize the full reconstruction of the events obtained from both the experiments and FLUKA Monte Carlo (MC) simulations. The resolution of the detectors tested in ad-hoc experimental campaign have been applied to simulated samples in order to recreate experimental-like data. The produced software is then applied to the sample to perform several studies presented in Chapter 4.

A huge campaign of simulated data has been generated in order to perform all the analysis chain to test the apparatus for the exclusive differential cross section measurements that will be performed by FOOT. The expected fragments charge resolution ranges between  $\sim 6\%$  for hydrogen and  $\sim 2\%$  for oxygen. The redundancy of sub-detectors in the FOOT apparatus allows to reconstruct the fragments mass by coupling time of flight, momentum and kinetic energy in three different ways. This aspect is the key to perform a mass discrimination also at higher energies, when the measurement might have been compromised by a kinetic energy underestimation due to the large neutrons production in the calorimeter. The achieved mass number resolution ranges between  $\sim 3.5\%$  and  $\sim 4.5\%$ . In the same software, the procedure to reconstruct the differential cross section of each

isotope generated in the beam-target interaction is included too. The results have been compared with the cross section generated by MC and found to be within  $\sim 25\%$  of agreement for most of the fragment types. The differential cross section values obtained in the case of  $C_2H_4$  and  $C$  targets have been combined to obtain the cross section on hydrogen by subtraction. The result differs by  $\sim 8\%$  from MC predictions. The software has been employed to perform a systematic study varying the resolution on time of flight, momentum and kinetic energy in order to estimate the impact of each detector on the accuracy of the cross section determination. The results show that it is very influenced by the time of flight resolution, while the dependence on the momentum and kinetic energy precision is weaker. Currently, the detectors resolution ( $\sigma(TOF) \simeq 70$  ps,  $\sigma(p)/p \simeq 3.7\%$  and  $\sigma(E_{kin})/E_{kin} \simeq 1.5\%$ ) allow a fragments mass identification with an accuracy of  $\sim 3\%$ , while the reconstructed number of events overestimates the MC prediction by  $\sim 7\%$ . The cross section estimation for the most abundant isotope (i.e.,  $^{12}C$ ) is within  $\sim 9\%$ .

The analysis of the first experimental data acquired with the FOOT apparatus in 2019 is presented in Chapter 5. Even if the statistic collected was very poor, the setup discriminated well the fragments charge providing very encouraging results for future experimental campaigns. The reconstruction of the charge of the produced nuclear fragments reflect the precision predicted by the MC simulations.

Several measurements at CNAO and GSI with carbon and oxygen ions are foreseen in 2021. The data taking will be also of paramount importance to investigate the possibility to exploit the FOOT electronic apparatus to identify secondary neutrons produced by beams and targets relevant for space radiation protection, as discussed in Chapter 6.

# Appendix

## Analysis of performances

In the following, all the results of the systematic study referring to carbon isotopes fragments (i.e.,  $^9C$ ,  $^{10}C$ ,  $^{11}C$ ,  $^{13}C$ ,  $^{14}C$ ) for the case of a 200 MeV/u  $^{16}O$  beam impinging on a  $C_2H_4$  target are reported.

$\sigma(\text{TOF})[\text{ps}]$	$\frac{\sigma(p)}{p}[\%]$	$\frac{\sigma(E_{kin})}{E_{kin}}[\%]$	$\sigma(A)[\%]$	$\frac{N_{reco}}{N_{MC}}$	$\frac{\sigma_{f,reco}}{\sigma_{f,MC}}$
40			$2.2 \pm 1.2$	$1.0 \pm 0.03$	$0.7 \pm 0.1$
50			$2.6 \pm 1.4$	$1.0 \pm 0.04$	$0.7 \pm 0.1$
60			$3.1 \pm 1.8$	$1.2 \pm 0.05$	$0.7 \pm 0.1$
70	3.7	1.5	$3.6 \pm 2.6$	$1.3 \pm 0.08$	$0.7 \pm 0.1$
80			$3.7 \pm 3.2$	$0.8 \pm 0.1$	$0.4 \pm 0.1$
90			$4.6 \pm 7.5$	$0.8 \pm 0.3$	$0.3 \pm 0.1$
	2.5		$3.1 \pm 2.0$	$0.9 \pm 0.1$	$0.7 \pm 0.1$
	3.0		$3.2 \pm 2.2$	$1.1 \pm 0.1$	$0.7 \pm 0.1$
	3.5		$3.7 \pm 3.0$	$1.4 \pm 0.1$	$0.8 \pm 0.1$
70	4.0	1.5	$3.5 \pm 3.5$	$1.5 \pm 0.1$	$1.0 \pm 0.1$
	4.5		$3.7 \pm 3.5$	$1.1 \pm 0.1$	$0.8 \pm 0.1$
	5.0		$3.0 \pm 3.6$	$1.1 \pm 0.1$	$0.6 \pm 0.1$
		1.0	$3.3 \pm 1.9$	$1.0 \pm 0.1$	$0.7 \pm 0.1$
		1.3	$3.4 \pm 2.9$	$1.3 \pm 0.1$	$0.9 \pm 0.1$
		1.6	$3.6 \pm 3.6$	$1.3 \pm 0.1$	$0.7 \pm 0.1$
70	3.7	1.9	$3.6 \pm 3.6$	$1.3 \pm 0.1$	$0.8 \pm 0.1$
		2.2	$3.6 \pm 4.1$	$0.9 \pm 0.1$	$0.9 \pm 0.1$
		2.5	$3.8 \pm 4.6$	$0.8 \pm 0.1$	$0.5 \pm 0.1$

**Table 1:** Variation of  $\sigma(A)$ ,  $\frac{N_{reco}}{N_{MC}}$  and  $\frac{\sigma_{f,reco}}{\sigma_{f,MC}}$  as a function of the resolutions on TOF,  $p$  or  $E_{kin}$ , keeping the other two variables fixed at the standard precision (respectively  $\sigma(\text{TOF})=70$  ps,  $\sigma(p)/p=3.7\%$ ,  $\sigma(E_{kin})/E_{kin}=1.5\%$ ), for  ${}^9\text{C}$  fragment generated by a 200 MeV/u  ${}^{16}\text{O}$  beam impinging on a  $\text{C}_2\text{H}_4$  target, as obtained with the  $\chi^2$  method approach after the application of a  $\chi^2 < 5$  cut.

$\sigma(\text{TOF})[\text{ps}]$	$\frac{\sigma(p)}{p}[\%]$	$\frac{\sigma(E_{kin})}{E_{kin}}[\%]$	$\sigma(A)[\%]$	$\frac{N_{reco}}{N_{MC}}$	$\frac{\sigma_{f,reco}}{\sigma_{f,MC}}$
40			$2.1 \pm 0.3$	$1.0 \pm 0.01$	$0.9 \pm 0.03$
50			$2.5 \pm 1.1$	$1.0 \pm 0.02$	$0.9 \pm 0.03$
60			$2.8 \pm 1.3$	$1.0 \pm 0.03$	$0.9 \pm 0.03$
70	3.7	1.5	$3.1 \pm 2.6$	$1.1 \pm 0.1$	$0.9 \pm 0.03$
80			$3.2 \pm 4.7$	$1.02 \pm 0.1$	$1.1 \pm 0.03$
90			$3.4 \pm 12.0$	$0.7 \pm 0.3$	$0.9 \pm 0.04$
	2.5		$3.0 \pm 1.4$	$1.1 \pm 0.03$	$0.9 \pm 0.03$
	3.0		$3.1 \pm 1.6$	$1.1 \pm 0.04$	$0.9 \pm 0.03$
	3.5		$3.0 \pm 2.0$	$1.1 \pm 0.1$	$0.9 \pm 0.03$
70	4.0	1.5	$3.2 \pm 2.6$	$1.0 \pm 0.1$	$0.8 \pm 0.03$
	4.5		$3.1 \pm 2.8$	$1.1 \pm 0.1$	$0.8 \pm 0.03$
	5.0		$3.3 \pm 3.7$	$1.0 \pm 0.1$	$0.8 \pm 0.03$
		1.0	$3.0 \pm 0.3$	$1.1 \pm 0.03$	$0.9 \pm 0.03$
		1.3	$3.0 \pm 2.5$	$1.1 \pm 0.1$	$0.8 \pm 0.03$
		1.6	$3.1 \pm 2.6$	$1.1 \pm 0.1$	$0.9 \pm 0.01$
70	3.7	1.9	$3.1 \pm 2.7$	$1.1 \pm 0.1$	$0.9 \pm 0.03$
		2.2	$3.2 \pm 3.6$	$0.8 \pm 0.1$	$0.8 \pm 0.03$
		2.5	$3.1 \pm 3.8$	$0.8 \pm 0.1$	$0.8 \pm 0.04$

**Table 2:** Variation of  $\sigma(A)$ ,  $\frac{N_{reco}}{N_{MC}}$  and  $\frac{\sigma_{f,reco}}{\sigma_{f,MC}}$  as a function of the resolutions on TOF,  $p$  or  $E_{kin}$ , keeping the other two variables fixed at the standard precision (respectively  $\sigma(\text{TOF})=70$  ps,  $\sigma(p)/p=3.7\%$ ,  $\sigma(E_{kin})/E_{kin}=1.5\%$ ), for  ${}^{10}\text{C}$  fragment generated by a 200 MeV/u  ${}^{16}\text{O}$  beam impinging on a  $\text{C}_2\text{H}_4$  target, as obtained with the  $\chi^2$  method approach after the application of a  $\chi^2 < 5$  cut.

$\sigma(\text{TOF})[\text{ps}]$	$\frac{\sigma(p)}{p}[\%]$	$\frac{\sigma(E_{kin})}{E_{kin}}[\%]$	$\sigma(A)[\%]$	$\frac{N_{reco}}{N_{MC}}$	$\frac{\sigma_{f,reco}}{\sigma_{f,MC}}$
40			$2.1 \pm 0.1$	$1.0 \pm 0.01$	$0.9 \pm 0.01$
50			$2.4 \pm 0.2$	$1.0 \pm 0.01$	$0.9 \pm 0.01$

60			$2.7 \pm 0.4$	$1.0 \pm 0.01$	$0.9 \pm 0.01$
70			$2.9 \pm 1.2$	$0.9 \pm 0.03$	$0.9 \pm 0.01$
80			$3.1 \pm 2.9$	$0.9 \pm 0.1$	$0.9 \pm 0.01$
90			$3.4 \pm 3.0$	$0.8 \pm 0.2$	$0.8 \pm 0.01$
70	2.5	1.5	$2.7 \pm 0.5$	$1.0 \pm 0.02$	$0.9 \pm 0.01$
	3.0		$2.8 \pm 0.6$	$1.0 \pm 0.02$	$0.9 \pm 0.01$
	3.5		$2.9 \pm 0.7$	$0.9 \pm 0.03$	$0.9 \pm 0.01$
	4.0		$2.7 \pm 1.3$	$0.9 \pm 0.03$	$0.9 \pm 0.01$
	4.5		$3.0 \pm 1.4$	$0.9 \pm 0.04$	$0.9 \pm 0.01$
70	5.0		$3.0 \pm 1.4$	$0.9 \pm 0.04$	$0.9 \pm 0.01$
	3.7	1.0	$2.9 \pm 0.02$	$1.0 \pm 0.02$	$0.9 \pm 0.01$
		1.3	$2.9 \pm 0.7$	$0.9 \pm 0.03$	$0.9 \pm 0.01$
		1.6	$2.9 \pm 1.2$	$0.9 \pm 0.03$	$0.9 \pm 0.01$
		1.9	$2.9 \pm 1.3$	$0.9 \pm 0.04$	$0.9 \pm 0.01$
2.2		$3.0 \pm 1.4$	$1.0 \pm 0.04$	$0.9 \pm 0.01$	
	2.5		$3.1 \pm 1.5$	$1.0 \pm 0.1$	$0.9 \pm 0.01$

**Table 3:** Variation of  $\sigma(A)$ ,  $\frac{N_{reco}}{N_{MC}}$  and  $\frac{\sigma_{f,reco}}{\sigma_{f,MC}}$  as a function of the resolutions on TOF, p or  $E_{kin}$ , keeping the other two variables fixed at the standard precision (respectively  $\sigma(\text{TOF})=70$  ps,  $\sigma(p)/p=3.7\%$ ,  $\sigma(E_{kin})/E_{kin}=1.5\%$ ), for  $^{11}\text{C}$  fragment generated by a 200 MeV/u  $^{16}\text{O}$  beam impinging on a  $\text{C}_2\text{H}_4$  target, as obtained with the  $\chi^2$  method approach after the application of a  $\chi^2 < 5$  cut.

$\sigma(\text{TOF})[\text{ps}]$	$\frac{\sigma(p)}{p}[\%]$	$\frac{\sigma(E_{kin})}{E_{kin}}[\%]$	$\sigma(A)[\%]$	$\frac{N_{reco}}{N_{MC}}$	$\frac{\sigma_{f,reco}}{\sigma_{f,MC}}$
40	3.7	1.5	$2.1 \pm 0.3$	$1.0 \pm 0.1$	$0.9 \pm 0.01$
50			$2.3 \pm 0.5$	$1.0 \pm 0.01$	$0.9 \pm 0.01$
60			$2.5 \pm 1.3$	$0.9 \pm 0.03$	$0.9 \pm 0.02$
70			$2.6 \pm 1.8$	$0.8 \pm 0.1$	$0.9 \pm 0.01$
80			$2.6 \pm 3.6$	$0.6 \pm 0.2$	$0.8 \pm 0.01$
90			$2.7 \pm 5.7$	$0.4 \pm 0.2$	$0.9 \pm 0.01$
70	2.5	1.5	$2.6 \pm 1.4$	$0.9 \pm 0.04$	$0.9 \pm 0.01$
	3.0		$2.6 \pm 1.6$	$0.8 \pm 0.1$	$0.9 \pm 0.01$
	3.5		$2.7 \pm 1.7$	$0.8 \pm 0.1$	$0.9 \pm 0.01$
	4.0		$2.6 \pm 2.5$	$0.8 \pm 0.1$	$0.9 \pm 0.02$
	4.5		$2.7 \pm 2.6$	$0.7 \pm 0.1$	$0.8 \pm 0.01$
	5.0		$2.5 \pm 2.6$	$0.7 \pm 0.1$	$0.8 \pm 0.01$
70	3.7	1.0	$2.6 \pm 1.2$	$0.8 \pm 0.1$	$0.9 \pm 0.01$
		1.3	$2.6 \pm 1.7$	$0.8 \pm 0.1$	$0.9 \pm 0.01$
		1.6	$2.6 \pm 1.8$	$0.8 \pm 0.1$	$0.8 \pm 0.01$

	1.9	$2.7 \pm 2.6$	$0.7 \pm 0.1$	$0.8 \pm 0.01$
	2.2	$2.7 \pm 2.1$	$0.7 \pm 0.1$	$0.8 \pm 0.01$
	2.5	$2.7 \pm 2.8$	$0.7 \pm 0.1$	$0.8 \pm 0.01$

**Table 4:** Variation of  $\sigma(A)$ ,  $\frac{N_{reco}}{N_{MC}}$  and  $\frac{\sigma_{f,reco}}{\sigma_{f,MC}}$  as a function of the resolutions on TOF,  $p$  or  $E_{kin}$ , keeping the other two variables fixed at the standard precision (respectively  $\sigma(\text{TOF})=70$  ps,  $\sigma(p)/p=3.7\%$ ,  $\sigma(E_{kin})/E_{kin}=1.5\%$ ), for  $^{13}\text{C}$  fragment generated by a 200 MeV/u  $^{16}\text{O}$  beam impinging on a  $\text{C}_2\text{H}_4$  target, as obtained with the  $\chi^2$  method approach after the application of a  $\chi^2 < 5$  cut.

$\sigma(\text{TOF})[\text{ps}]$	$\frac{\sigma(p)}{p}[\%]$	$\frac{\sigma(E_{kin})}{E_{kin}}[\%]$	$\sigma(A)[\%]$	$\frac{N_{reco}}{N_{MC}}$	$\frac{\sigma_{f,reco}}{\sigma_{f,MC}}$
40			$2.3 \pm 1.1$	$1.0 \pm 0.02$	$0.9 \pm 0.03$
50			$2.8 \pm 1.3$	$1.1 \pm 0.03$	$1.0 \pm 0.03$
60			$3.3 \pm 3.3$	$1.2 \pm 0.1$	$1.0 \pm 0.03$
70	3.7	1.5	$4.0 \pm 5.4$	$1.4 \pm 0.1$	$1.0 \pm 0.03$
80			$4.7 \pm 5.8$	$1.8 \pm 0.1$	$1.0 \pm 0.03$
90			$5.9 \pm 6.0$	$2.3 \pm 0.02$	$0.9 \pm 0.03$
	2.5		$3.6 \pm 1.6$	$1.3 \pm 0.1$	$1.0 \pm 0.03$
	3.0		$3.7 \pm 4.4$	$1.4 \pm 0.1$	$1.0 \pm 0.03$
	3.5		$4.0 \pm 5.4$	$1.4 \pm 0.01$	$1.0 \pm 0.03$
70	4.0	1.5	$4.1 \pm 6.4$	$1.5 \pm 0.1$	$1.0 \pm 0.03$
	4.5		$4.2 \pm 10.3$	$1.6 \pm 0.11$	$1.1 \pm 0.03$
	5.0		$4.3 \pm 6.5$	$1.6 \pm 0.1$	$1.1 \pm 0.03$
		1.0	$3.81 \pm 4.36$	$1.42 \pm 0.03$	$1.02 \pm 0.03$
		1.3	$3.86 \pm 5.40$	$1.41 \pm 0.09$	$0.99 \pm 0.02$
		1.6	$4.04 \pm 6.38$	$1.49 \pm 0.10$	$1.01 \pm 0.03$
70	3.7	1.9	$4.11 \pm 7.28$	$1.55 \pm 0.11$	$1.06 \pm 0.03$
		2.2	$4.20 \pm 7.44$	$1.58 \pm 0.12$	$1.04 \pm 0.03$
		2.5	$4.35 \pm 8.45$	$1.62 \pm 0.13$	$1.04 \pm 0.03$

**Table 5:** Variation of  $\sigma(A)$ ,  $\frac{N_{reco}}{N_{MC}}$  and  $\frac{\sigma_{f,reco}}{\sigma_{f,MC}}$  as a function of the resolutions on TOF,  $p$  or  $E_{kin}$ , keeping the other two variables fixed at the standard precision (respectively  $\sigma(\text{TOF})=70$  ps,  $\sigma(p)/p=3.7\%$ ,  $\sigma(E_{kin})/E_{kin}=1.5\%$ ), for  $^{14}\text{C}$  fragment generated by a 200 MeV/u  $^{16}\text{O}$  beam impinging on a  $\text{C}_2\text{H}_4$  target, as obtained with the  $\chi^2$  method approach after the application of a  $\chi^2 < 5$  cut.

# Bibliography

- [1] In: *Annals of ICRPNew* , Ref: 4819-7515-188 (2012).
- [2] F. Tommasino and M. Durante. “Proton radiobiology”. In: *Cancers (Basel)* 7.1 (2015), pp. 353–381.
- [3] H. Bethe. “Zur theorie des durchgangs schneller korpuskularstrahlen durch materi”. In: *Ann. Phys.* 397 (1930), pp. 325–400.
- [4] F. Bloch. “Bremsvermögen von atomen mit mehreren elektronen”. In: *Z. Phys. A: Hadrons Nucl.* 81 (1933), pp. 367–76.
- [5] F. Bloch. “Zur bremsung rasch bewegter teilchen beim durchgang durch materie”. In: *Ann. Phys.* 408 (1933), pp. 285–320.
- [6] K. Parodi. PhD thesis. 2004.
- [7] A.C. Kraan. “Range verification methods in particle therapy: underlying physics and Monte Carlo modeling”. In: *Fron. Oncol.* 5 (2015), p. 150.
- [8] D. Schardt et al. “Heavy-ion tumor therapy: physical and radiobiological benefits”. In: *Rev. Mod. Phys.* 82.1 (2010), pp. 383–425.
- [9] A. Mairani. PhD thesis. 2007.
- [10] T. Böhlen et al. “The FLUKA code: developments and challenges for high energy and medical applications”. In: *Nucl. Data Sheets* 120 (2014), pp. 211–214.
- [11] P.V. Vavilov. “Ionization losses of high-energy heavy particles”. In: *Sov. Phys. JETP* 5 (1957), pp. 749–751.
- [12] G. Molière. “Theorie der streuung schneller geladener teilchen ii mehrfach-und vielfachstreuung”. In: *Z. Naturforsch. A* 3.2 (1948), pp. 78–97.
- [13] V.L. Highland. “Some practical remarks on multiple scattering”. In: *Nucl. Instrum. Meth.* 129.2 (1975), pp. 497–499.
- [14] R. Serber. “Nuclear reactions at high energies”. In: *Phys. Rev.* 72.11 (1947), p. 1114.

- [15] Gyo T. and K.M. Watson. “Scattering of fast neutrons and protons by atomic nuclei”. In: *Phys. Rev.* 97 (1955), pp. 1337–43.
- [16] R. R. Wilson. “Radiological use of fast protons”. In: *Radiology* 47 (1946), pp. 487–91.
- [17] C. A. Tobias and P. W. Todd. “Heavy charged particles in cancer therapy”. In: *Natl. Cancer Inst.* 24 (1967), pp. 1–21.
- [18] M. Durante and J. Debus. “Heavy charged particles: does improved precision and higher biological effectiveness translate to better outcome in patients?”. In: *Semin Radiat Oncol.* 28 (2018), pp. 160–7.
- [19] Nobuyuki Kanematsu, Taku Inaniwa, and Yusuke Koba. “Relationship between electron density and effective densities of body tissues for stopping, scattering, and nuclear interactions of proton and ion beams”. In: *Med. Phys.* 39 (2012), pp. 1016–1020.
- [20] Taku Inaniwa, Nobuyuki Kanematsu, H. Tsuji, and T. Kamada. “Influence of nuclear interactions in body tissues on tumor dose in carbon-ion radiotherapy”. In: *Med. Phys.* 42 (2015), pp. 7132–7137.
- [21] Taku Inaniwa, Sung Hyun Lee, Kota Mizushima, Dousatsu Sakata, Yoshiyuki Iwata, Nobuyuki Kanematsu, and Toshiyuki Shirai. “Nuclear-interaction correction for patient dose calculations in treatment planning of helium-, carbon-, oxygen-, and neon-ion beams”. In: *Phys. Med. Biol.* 65 (2020), pp. 025004–025016.
- [22] M. Durante and F. Cucinotta. “Physical basis of radiation protection in space travel”. In: *Rev. Mod. Phys.* 83 (2011), p. 1245.
- [23] J. Norbury et al. “Review of nuclear physics experiments for space radiation”. In: *Health Phys.* 103 (2012), pp. 640–642.
- [24] B. Braunn et al. “Assessment of nuclear-reaction codes for proton-induced reactions on light nuclei below 250 MeV”. In: *Eur. Phys. J. Plus* 130 (2015), p. 153.
- [25] N. Matsufuji, A. Fukumura, M. Komori, T. Kanai, and T. Kohno. “Influence of fragment reaction of relativistic heavy charged particles on heavy-ion radiotherapy”. In: *Phys. Med. Biol.* 48 (2003), p. 1605.
- [26] *Experimental nuclear reaction data (EXFOR)*. <http://www-nds.iaea.org/exfor/exfor.html/>.
- [27] A.S. Iljinov, V.G. Semenov, M.P. Semenova, N.M. Sobolevsky, and L.V. Udovenko. “Production of radionuclides at intermediate energies”. In: *Landolt-Börnstein, New Series (Springer-Verlag, Berlin-Heidelberg) I/13* (1991).

- 
- [28] A. Koning, S. Hilaire, and M. Duijvestijn. “TALYS-1.0”. In: *Proceedings of the International Conference on Nuclear Data for Science and Technology 1* (2008), pp. 211–214.
- [29] A. Boudard, J. Cugnon, J.C. David, S. Leray, and D. Mancusi. “New potentialities of the Liège intranuclear cascade model for reactions induced by nucleons and light charged particles”. In: *Phys. Rev. C* 87 (2013), p. 014606.
- [30] H. H. Barschall, M. B. Chadwick, D. T. L. Jones, J. P. Meulders, H. Schuhmacher, and P. G. Young. “Nuclear data for neutron and proton radiotherapy and for radiation protection (Report 63)”. In: *Journal of the International Commission on Radiation Units and Measurements, Issue 2* (2000), p. 014606.
- [31] K. Gunzert-Marx et al. “Secondary beam fragments produced by 200 MeV/u  $^{12}\text{C}$  ions in water and their dose contributions in carbon ion radiotherapy”. In: *New J. Phys.* 10.7 (2008), p. 075003.
- [32] J. Doudet et al. “Double-differential fragmentation cross-sections measurements of 95 MeV/u  $^{12}\text{C}$  beams on thin targets for hadrontherapy”. In: *Phys. Rev. C* 88.2 (2013), p. 024606.
- [33] M. Toppi et al. “Measurement of fragmentation cross sections of  $^{12}\text{C}$  ions on a thin gold target with the FIRST apparatus”. In: *Phys. Rev. C* 93.6 (2016), p. 064601.
- [34] M. Marafini et al. “Secondary radiation measurements for particle therapy applications: nuclear fragmentation produced by  $^4\text{He}$  ion beams in a PMMA target”. In: *Phys. Med. Biol.* 62.4 (2017), p. 1291.
- [35] M. Rovituso et al. “Fragmentation of 120 and 200 MeV/u  $^4\text{He}$  ions in water and PMMA targets”. In: *Phys. Med. Biol.* 62.4 (2017), p. 1310.
- [36] J. W. Wilson et al. “Transport methods and interactions for space radiations”. In: *NASA Reference Publication* 1257 (1991).
- [37] J. A. Simpson et al. “Elemental and isotopic composition of the Galactic Cosmic Rays”. In: *Annual Review of Nuclear and Particle Science* 33 (1983), pp. 323–382.
- [38] F. Tommasino et al. “New ions for therapy”. In: *Int. J. Part. Ther.* 2.3 (2015), pp. 428–438.
- [39] B. Knäusl et al. “Can particle beam therapy be improved using helium ions? - a planning study focusing on pediatric patients”. In: *Acta Oncol.* 55.6 (2016), pp. 751–759.
- [40] S. Carboni et al. “Particle identification using the  $\Delta\text{E-E}$  technique and pulse shape discrimination with the silicon detectors of the FAZIA project”. In: *Nucl. Instrum. Methods Phys. Res.* (2012), p. 664.

- [41] S. Majewski and C. Zorn. “Fast scintillators for high radiation levels”. In: *World Scientific* (1992).
- [42] R. Novotny. “The BaF2 Photon Spectrometer TAPS”. In: *IEEE Trans. Nucl. Sci.* 38 (1991), pp. 379–85.
- [43] Scherzinger J., Al Jebali R., Annand J.R.M., Fissum K.G, Hall-Wilton R., Kanaki K., Lundin M., Nilsson B., Perrey H., Rosborg A., and Svensson H. “The light-yield response of a NE-213 liquid-scintillator detector measured using 2–6 MeV tagged neutrons”. In: *Nuclear Instrument and Methods in Physics Research A* 840 (2016), pp. 121–127.
- [44] A. Ferrari et al. “FLUKA: a multi-particle transport code”. In: *CERN-2005-10, INFN TC 05/11, SLAC-R-773* (2005).
- [45] M. Francesconi, A. M. Baldini, and L. Galli et al. *The WaveDAQ integrated Trigger and Data Acquisition System for the MEG II experiment*. arXiv: 1806.09218 [physics.ins-det]. 2018.
- [46] Y. Dong, G. Silvestre, and S. Colombi et al. “The Drift Chamber detector of the FOOT experiment: performance analysis and external calibration”. In: *Nuclear Instrument and Methods in Physics Research A* 986 (2021), p. 164756.
- [47] N. Simos et al. “Demagnetization of  $Nd_2 Fe_{14} B$ ,  $Pr_2 Fe_{14} B$ , and  $Sm_2 Co_{17}$  permanent magnets in spallation irradiation fields”. In: *IEEE T. Magn.* 54 (2018), BNL-205752-2018–JAAM.
- [48] “PLUME”. In: *www.iphc.cnrs.fr/PLUME.html* ().
- [49] W. de Boer et al. “Measurements with a CMOS pixel sensor in magnetic fields”. In: *Nucl. Instr. Meth. A* 487 (2002), pp. 163–169.
- [50] O. Adriani et al. “Comprehensive study of the effects of irradiation on charge collection efficiency in silicon detectors”. In: *Nucl. Instr. Meth. A* 396 (1997), p. 76.
- [51] B. Alpat et al. “The internal alignment and position resolution of the AMS-02 silicon tracker determined with cosmic-ray muons”. In: *Nucl. Instr. Meth. A* 613 (2010), p. 207.
- [52] P. Fernandez et al. “Simulation of new p-type strip detectors with trench to enhance the charge multiplication effect in the n-type electrodes”. In: *Nucl. Instr. Meth. A* 658 (2011), p. 98.
- [53] H.F.-W. Sadrozinski et al. “Sensors for ultra-fast silicon detectors”. In: *Nucl. Instr. Meth. A* 7675 (2014), p. 7.
- [54] G. Pellegrini et al. “Technology developments and first measurements of Low Gain Avalanche Detectors (LGAD) for high energy physics applications”. In: *Nucl. Instr. Meth. A* 765 (2014), p. 12.

- [55] M. Morrocchi et al. “Development and characterization of a E-TOF detector prototype for the FOOT experiment”. In: *Nucl. Instr. Meth. A* 916 (2019), p. 116.
- [56] N. Armenise et al. “High-speed particle tracking in nuclear emulsion by last-generation automatic microscopes”. In: *Nucl. Instr. Meth. A* 551 (2005), p. 261.
- [57] L. Arrabito et al. “Hardware performance of a scanning system for high speed analysis of nuclear emulsions”. In: *Nucl. Instr. Meth. A* 568 (2006), p. 578.
- [58] A. Alexandrov et al. “Further progress for a fast scanning of nuclear emulsions with Large Angle Scanning System”. In: *JINST* 9 (2014), p. C02034.
- [59] A. Alexandrov et al. “A new fast scanning system for the measurement of large angle tracks in nuclear emulsions”. In: *JINST* 11.10 (2015), P11006.
- [60] A. Alexandrov et al. “A new generation scanning system for the high-speed analysis of nuclear emulsions”. In: *JINST* 11 (2016), p. 6002.
- [61] A. Alexandrov et al. “The continuous motion technique for the new generation scanning system”. In: *Scientific reports* 7 7 (2017), p. 7310.
- [62] De Lellis G. et al. “Emulsion Cloud Chamber technique to measure the fragmentation of a high-energy carbon beam”. In: *J. Instrum.* 2 2.06 (2007), P06004.
- [63] De Lellis G. et al. “Measurements of the fragmentation of Carbon nuclei used in hadron therapy”. In: *Nuclear Physics A* 853 (2011), p. 124.
- [64] M.C. Montesi and A. Lauria et al. “Ion charge separation with new generation of nuclear emulsion films”. In: *De Gruyter, Open Phys.* 17 (2019), pp. 233–240.
- [65] N. Agafonova et al. “Momentum measurements by the multiple coulomb scattering method in the OPERA lead-emulsion target”. In: *New Journal of Physics* 14 (2013), p. 13.
- [66] G.De Lellis et al. “Momentum measurement by the angular method in the Emulsion Cloud Chamber”. In: *Nucl. Instr. and Meth. A* 512 (2003), p. 539.
- [67] Haettner E., Iwase H., Krämer M., Kraft G., and Schardt D. “Experimental study of nuclear fragmentation of 200 and 400 MeV/u  $^{12}\text{C}$  ions in water for applications in particle therapy”. In: *Phys. Med. Biol.* 58.23 (2013), pp. 8265–79.
- [68] Weimar R., Romberg R., Frigo S., Kasshke B., and Feulner P. “Time-of-flight techniques for the investigation of kinetic energy distributions of ions and neutrals desorbed by core excitations”. In: *Surf. Sci.* 451 (2000), pp. 124–9.
- [69] Tarasov O.B. “LISE++: Radioactive beam production with inflight separators”. In: *NIMB* 266 (2008), pp. 4657–4664.

- 
- [70] Golovkov M.S., Aleksandrov D.V., Chulkov L.V., Kraus G., and Schardt D. “Fragmentation of 270 AMeV carbon ions in water”. In: *Adv.Hadron Therapy Int.Congr.Ser.* (1997), p. 1144.
- [71] Bertini H.W., R.T Santoro, and Hermann O.W. “Calculated nucleon spectra at several angles from 192-, 500-, 700-, and 900-MeV  $^{12}\text{C}$  on  $^{56}\text{Fe}$ ”. In: *Phys. Rev. C* 14 (1976).
- [72] Slaba T.C. et al. “Optimal shielding thickness for galactic cosmic ray environments”. In: *Life Sci. Space Res.*12 (2017), pp. 1–15.
- [73] Zeitlin C. et al. “Measurements of energetic particle radiation in transit to Mars on the Mars Science Laboratory”. In: *Science*.340 (2013), pp. 1080–1084.
- [74] Köhler J. et al. “Measurements of the neutron spectrum in transit to Mars on the Mars Science Laboratory”. In: *Life Sci. Space Res.*5 (2015), pp. 6–12.
- [75] Köhler J. et al. “Measurements of the neutron spectrum on the Martian surface with MSL/RAD”. In: *J. Geophys. Res.*119 (2014), pp. 594–603.
- [76] Durante M. “Space radiation protection: destination Mars”. In: *Life Sci. Space Res.*1 (2014), pp. 2–9.
- [77] Kurosawa T., Nakao N., Nakamura T., Iwase H., Sato H., Uwamino Y., and Fukumura A. “Neutron yields from thick C, Al, Cu, and Pb targets bombarded by 400 MeV/nucleon Ar, Fe, Xe and 800 MeV/nucleon Si ions”. In: *Physical Review C*.62 (2000), p. 044615.
- [78] Giraudo M., Schuy C., Weber U., Rovituso M., Santin G., Norbury J.W., Tracino E., Menicucci A., Bocchini L., Lobascio C., Durante M., and La Tessa C. “Accelerator-Based Tests of Shielding Effectiveness of Different Materials and Multilayers using High-Energy Light and Heavy Ions”. In: *Radiation Research Society* 190.5 (2018), pp. 526–537.
- [79] La Tessa C., Sivertz M., Hung Chiang I., Lowenstein D., and Rusek A. “Overview of the NASA space radiation laboratory”. In: *Life Sci. Space Res.* 11 (2016), pp. 18–23.
- [80] S. Agostinelli et al. “Geant4 — a simulation toolkit”. In: *Nucl. Instr. and Meth. A* 506 (2003), pp. 250–303.
- [81] J. Rauch and T .Schlüter. “GENFIT – a generic track-fitting toolkit”. In: *J. Phys. Conf. Ser.* 608 (2015), p. 012042.
- [82] G. Battistoni et al. “The FLUKA code: an accurate simulation tool for Particle Therapy”. In: *Fron. Oncol.* 6 (2016), p. 116.
- [83] S. M. Valle. “Design, simulation and performances study of the FOOT experiment”. PhD thesis. 2019, pp. 63–88.

- [84] V.Vlachoudis. “FLAIR: A Powerful But User Friendly Graphical Interface For FLUKA”. In: *Proc. Int. Conf. on Mathematics, Computational Methods Reactor Physics* (2009).
- [85] G. Traini et al. “Performance of the ToF detectors in the FOOT experiment”. In: *Il Nuovo Cimento* 43 (2020), p. 16.
- [86] D’Agostini G. “A multidimensional unfolding method based on Bayes’ theorem”. In: *Nucl. Instrum. Meth. A* 362.2-3 (1995), pp. 487–498.
- [87] T. Adye. “RooUnfold: ROOT Unfolding Framework”. URL: <http://hepunix.rl.ac.uk/~adye/software/unfold/RooUnfold.html>.
- [88] Zarrella R. “Charge identification of nuclear fragments with the Time-Of-Flight detectors of the FOOT experiment”. Master Thesis. 2020, p. 35. URL: [https://etd.adm.unipi.it/theses/available/etd-03162020-114207/unrestricted/Thesis\\_Roberto\\_Zarrella.pdf](https://etd.adm.unipi.it/theses/available/etd-03162020-114207/unrestricted/Thesis_Roberto_Zarrella.pdf).
- [89] Birks J.B. “The theory and practice of scintillation counting”. In: *International Series of Monographs in Electronics and Instrumentation* Pergamon (1964), pp. xvii–xviii.
- [90] Newhauser W.D and Zhang R. “The physics of proton therapy”. In: *Phys Med Biol.* 60.8 (2015), pp. 115–209.
- [91] Battistoni G. et al. “Overview of the FLUKA code”. In: *Ann. Nucl. Energy.* 82 (2015), pp. 10–18.